DESIGN OF ACTUATION SYSTEM AND MINIMIZATION OF SENSOR CONFIGURATION FOR GAIT EVENT DETECTION FOR GEN 3.0 PORTABLE POWERED ANKLE-FOOT ORTHOSIS (PPAFO)

BY

ZIMING WANG

THESIS

Submitted in partial fulfillment of the requirements
for the degree of Master of Science in Mechanical Engineering
in the Graduate College of the
University of Illinois at Urbana-Champaign, 2016

Urbana, Illinois

Advisor:

Professor Elizabeth T. Hsiao-Wecksler

Abstract

Powered ankle-foot orthoses (AFOs), which are capable of providing assistive torque at the ankle joint, have significant potential as both assistance and rehabilitation devices. Technology advancements have led to great progression in the development of powered AFOs. Our group had developed the Portable Powered Ankle-Foot Orthosis (PPAFO) that was capable of providing bidirectional assistive torque at the ankle joint. Two generations of the PPAFO were previously developed. Both designs used two different off-the-shelf rotary actuators. This thesis consists of two studies focusing on the development of a new compact higher torque actuation system and the identification of a minimum sensor configuration for gait event detection for a powered AFO.

Study 1 presents the design and evaluation of a new actuation system for the PPAFO (Generation 3.0). The actuation system utilized two dual-action linear actuators and a customized gear train. Compared with the previous designs, it generated higher torque and power while providing a thinner lateral profile. The new design had a total weight of (680g) and was capable of generating 32 Nm torque and 110 W power. While running under the same torque and power level as the previous designs, the new design offered better longevity (42.9% and 81.4% increases in normalized run time for test bench emulation and treadmill walking). Although the overall weight of the new actuation system had a 20% increase compared with previous design, it could generate 166.7% more torque and 120% more power, which will enable us to test the system at various torque and power settings.

Study 2 investigated the minimum sensor configuration for detecting gait events. Knowledge of the expected orientation and behavior of a limb as related to specific events during the gait cycle (or state timing as a function of the percentage of the gait cycle, % GC) is essential to allow appropriate control of a powered AFO. A total of five sensors were selected (two force sensitive sensors, one ankle angle sensor, and two inertial measurement units (IMU)). The performances of selected sensor configurations were quantified and compared through state-based and event-based approaches in terms of gait state estimation and gait event detection timing, respectively. Gait data were collected from five healthy subjects while walking on a treadmill wearing the Gen 3.0 PPAFO. Results indicated that, while single IMU configurations (located on the shank or foot) both outperformed all other configurations (mean state estimation error: < 2% GC; mean event detection timing error: < 23 ms), the shank IMU was able to detect more gait events than the foot IMU. Since more detectable events could improve the system's robustness (i.e., adjusting to variable speeds) by updating estimation more frequently, a single shank IMU configuration was recommended for powered AFO applications.

To Father and Mother

Acknowledgments

I would like to thank my advisor, Professor Elizabeth T. Hsiao-Wecksler, with my deepest sincerity for her continued support, patience and guidance throughout my master's journey here at the U of I. She has walked me through all the stages of the writing of this thesis. I would never be able to reach this present stage if without her consistent and illuminating instruction. I am honored to be one of her students as well as a member of the Human Dynamics and Controls Lab (HDCL).

I would like to thank my HDCL lab mates for their support as well. Their valuable insights, novel ideas and uplifting words have always inspired me. Thank you "M cube" (Matt Petrucci, Morgan Boes, and Mazharul Islam) for sharing your rich knowledge in biomechanics and controls. Thank you Alan Gaglio, Carrie Liang and Chenzhang Xiao for sharing your insights in electronics and machining. I would also like to thank all the undergraduate students who have help me with my projects (Yingjie He, Emily Seyforth, Toni Nepomuceno, Aaron Benjamin, Elizabeth Gacek, and David Lin).

I would also like to thank everyone who constantly supported me during my thesis writing process. I am especially thankful to Brian Blankenau, Matt Petrucci and Alan Gaglio, who continuously advised me throughout this time.

Finally, I would like to thank my parents Huijun Wang and Shufen Xu. Without their love and support I would never be able to complete this thesis.

This work is supported by the NSF Engineering Research Center for Compact and Efficient Fluid Power # 0540834.

Table of Contents

Chapter 1: INTRODUCTION

1.1 MOTIVATION

1.1.1 Walking Gait

Walking is a type of gait which has at least one foot in contact with the ground at all time. A normal walking gait can be divided into three functional tasks [1] and eight different events [2]. The first task is weight acceptance, which includes initial contact (IC), loading response (LR). The second task is single-limb support, which includes mid stance (MSt), terminal stance (TSt). The third task is limb advancement, which includes pre-swing (PSw), initial swing (ISw), mid-swing (MSw), and terminal swing (TSw) (Figure 1).

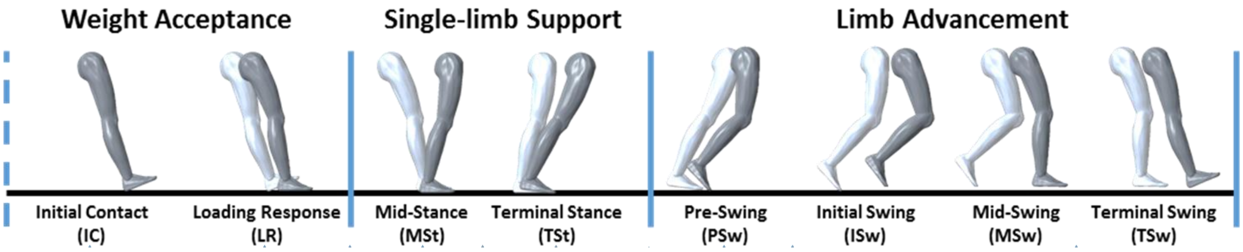

Figure 1 Different phases of a gait cycle (starting with the right heel striking the ground and continuing to the next heel strike) (figure created using human model downloaded from [3])

During the weight acceptance task, immediately after IC (i.e., heel strike, HS), body weight transfer onto the contacting ipsilateral limb is performed. This process provides shock absorption while preserving the momentum of progression. During the single-limb support task, the stance limb is undergoing a forward rocking motion while the contralateral foot is in a swing motion. Body weight is carried completely by the stance limb. During the final limb advancement task, the ipsilateral limb leaves the ground (i.e., toe off, TO) and begins to swing forward. While the contralateral foot is providing the weight support, the swinging limb reaches maximum swing speed to posture itself in preparation for next the IC [4].

1.1.2 Causes of Impaired Walking

Impaired walking is identified as one of the most common functional disability types [5]. An essential part of people's daily lives [6], walking is not only rhythmically complex, but also involves the intricate coordination of the brain, muscles and nerves as well as lower and upper limbs [4]. Therefore it can be affected by symptoms resulting from numerous neurological disorders, muscular pathologies and injuries. Diseases such as stroke, Parkinson's disease, multiple sclerosis or spinal cord injury may lead to a mobility disorder. Many of these diseases have significant correlations with aging. For example, an estimated 7 million Americans over 20 years of age have had a stroke. Nearly three-quarters of all strokes occurred in people over the age of 65, and 30 percent of survivors were unable to walk without some form of assistance. The risk of having a stroke more than doubles each decade after the age of 55 [7]. Projections indicate that by 2030, the prevalence of stroke will increase 24.9% from 2010 [8]. Despite the increasing stroke population, only 30.7% of stroke survivors received outpatient rehabilitation [9]. Thus, affordable and effective rehabilitation solutions were needed to help the patients restore their mobility.

1.1.3 Power-Assisted Solutions

It is necessary and impactful to develop affordable powered assistive devices that utilize state-of-the-art technologies to help people with disability regain the abilities to stand and walk [10]. To the author's knowledge, the earliest recorded publication that introduces the concept of "powered orthosis" was in the early 1960s [11]. Since then, especially in the last two decades, powered orthoses and exoskeletons have been developed extensively [12]. While powered orthoses were developed for various purposes, they can be classified as upper extremity devices, lower extremity devices, as well as full body devices [11, 13-15]. Many research groups have focused on lower-limb devices as they address the basic walking task [10]. The work presented in this thesis focused on the powered ankle-foot orthosis, because during walking gait, the ankle joint complex dissipates impact energy, helps to maintain stability and generates the highest output at push-off which is the primary source of power for forward propulsion [16].

1.1.4 From AFO to PPAFO

An ankle-foot orthoses (AFO) is an orthotic device used to correct gait deficiency at the ankle created by impairment to the lower limb. While current commercially available AFOs are still mostly passive [17], they are not capable of providing forward propulsion (plantarflexion) needed for normal and fast walking speeds. Powered AFOs, which are capable of providing assistive torque at the ankle joint, have significant potential as both assistance and rehabilitation devices [6]. Technology advancement has led to great progression in the development of powered AFOs. Unfortunately, while many different design approaches can easily be found, the challenges related to portability and power generation still remain.

Our group had developed the Portable Powered Ankle-Foot Orthosis (PPAFO) that was capable of providing bidirectional assistive torque at the ankle joint. Two generations of the PPAFO have been developed [6, 18] (Figure 2). The Gen 1.0 PPAFO used a dual-vane bidirectional rotatory pneumatic actuator (CRB2BW40-90D-DIM0065, SMC Corp of America; Noblesville, IN). The Gen 2.0 PPAFO utilized a different off-the-shelf actuator (PRN30D-90-45, Parker Hannifin, Cleveland, OH). The PPAFO was designed for untethered operation away from the confines of a lab or treadmill by use of a portable pneumatic power supply. In both generations, the peak plantarflexor torque was approximately 12 Nm for 100 psig input pressure, which is 17% of peak ankle torque that an 85 kg healthy walker can generate [19]. In addition, the bulkiness of the actuator made it difficult to be concealed underneath clothing and increased the risk of interfering with the surrounding environment during gait. Therefore, other solutions that could provide high torque and compact designs were investigated.

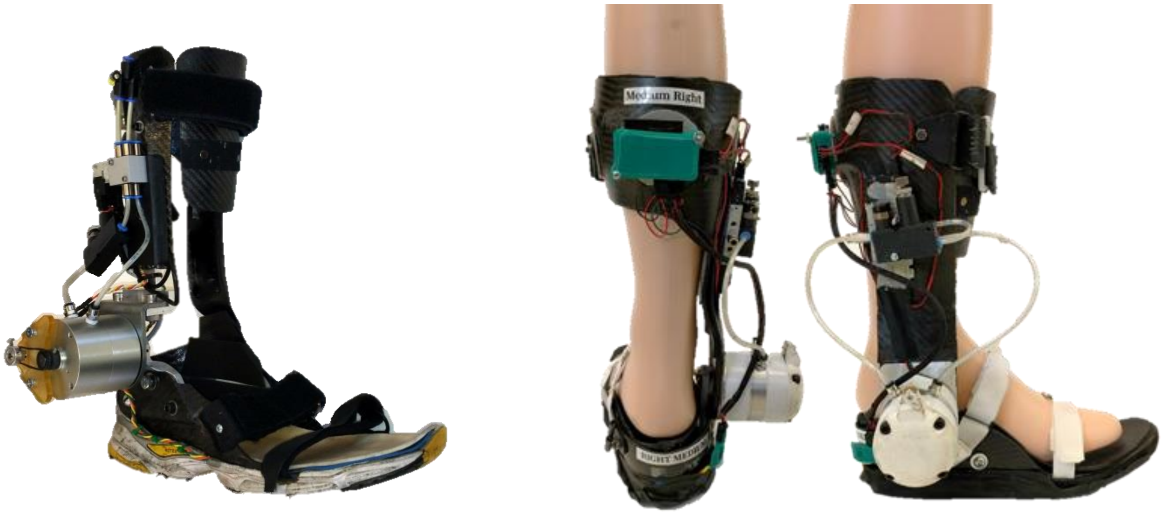

Figure 2 Gen 1.0 and 2.0 PPAFO Designs (rotatory actuator designs)

1.2 LITERATURE REVIEW

1.2.1 Existing Actuation Systems for Powered Orthoses and Exoskeletons

Robotic devices such as powered orthoses or exoskeletons for lower limb gait assistance have the potential to significantly improve mobility for people with lower-limb gait disorders. Because walking is not an energy neutral process, external power sources are needed for such devices to improve wearer’s mobility [17]. Developing joint power has been managed through electrical, hydraulic, pneumatic, as well as pure mechanical systems.

1.2.1.1 ELECTRICAL ACTUTION SYSTEMS

The most commonly used actuators for electric powered AFOs or exoskeletons are electric motors [20-22]. A motor is either aligned with a joint axis to apply power directly or utilize some forms of power transmission methods to translate the power from motor to joint [20, 21, 23]. With technology advancement, electrical motors remain competitive due to their capability of advanced motion control, high torque to weight ratio, as well as reduced running noise, though size, weight and power ratio of motor have been major concerns for wearable robotics.

Kazerooni's group at Berkeley designed an electric motor joint for the Berkeley lower extremity exoskeleton (BLEEX) [20] with the goal of reducing power consumption when compared with their hydraulic design. The main advantage of this electrical joint was its higher power efficiency. The major disadvantage was the size and the weight of the system (4.1 kg). One concern about this design was that the size and the weight of the system would greatly affect the overall inertia of the lower limbs. This added inertia could further affect the limb dynamics during locomotion. Another limitation was an overheating issue caused by the large amount of current going through the system. Overall, the joint was 15% efficient, as it required 93 W to produce 13.5 W of mechanical output. With a motor constant of 0.237 Nm/√W and transmission ratio of 80, the motor was estimated to output a 27Nm ankle torque. The torque capability of the system was also greatly dependent on the operating temperature. Therefore, a proper cooling system was also necessary for the motor joint design.

Walsh's group at Harvard developed a soft exosuit for gait assistance by utilizing an electrical motor and two Bowden cables per leg [21]. The system had a total weight of 6.5 kg and 65 W power consumption, while generating ~ 20 % of the nominal joint torque at the ankle joint. The Bowden cables were capable of providing flexible transmission from the actuator to the desired lower limb joint. With the help of a Bowden cable, the design shifts the motor unit to the side of an empty backpack. A soft webbing design not only reduced the amount of weight that was needed to attach to the lower limbs but also allowed the subject to wear normal clothes. However, because of the soft webbing, proper positioning was necessary. It was noted that actuation may present difficulties if the suit changed the position during locomotion.

Herr’s group at MIT presented a plantarflexion-only powered leg exoskeleton [22]. The design used fiberglass struts as an extension to the ankle joint moment arm which was connected to a brushless motor that was mounted on the anterior shank segments. The total mass of the system was 4.0 kg. It was capable of generating 70 Nm and11.5 W to each ankle joint.

1.2.1.2 HYDRAULIC SYSTEMS

Hydraulic systems have the highest power to mass ratio compared to electric motor or pneumatic systems [24]. Unlike electric motors and pneumatics, hydraulic actuator’s power to mass ratio increases with increasing weight [25], which means as the system’s weight increases, its power output increases at a higher ratio. Therefore, hydraulic systems tend to be more suitable for large scale applications. For low power applications, a hydraulic solution could be lighter than a electromechanical solution, if the hydraulics were running at a high pressure [26].

Durfee’s group at the University of Minnesota had designed a portable hydraulic ankle-foot orthosis [26, 27]. The system consisted of a custom hydraulic power supply and a custom hydraulic ankle-foot actuator secured to the shin and foot with carbon fiber supports. The two components were connected through two high pressure hydraulic tubes in which fluid power was transmitted. The total weight of the system was 4.2 kg and was capable of generating 90 Nm torque at 2000 psig, however actual power output during gait had yet to be presented. The hydraulic actuator was essentially a combination of two custom mini hydraulic cylinders with pistons attached to steel cables that wrapped around a pulley. The pulley was directly aligned to the ankle joint. Thus, as the cable was pulled by the cylinders, torque was generated at the ankle joint. One limitation about the design was that the bandwidth (actuation speed) of the system may not be high enough to meet normal gait speed requirements.

Another version of the BLEEX was powered by linear hydraulic actuators [13]. The design chose linear hydraulic actuators over rotary hydraulic actors because rotatory hydraulic actuators usually had either internal leakage or considerable friction [28]. The ankle-foot segment of the BLEEX consists of two separate parts, the foot and the shank. To create rotatory motion to the ankle joint one end of the linear hydraulic actuator was attached to the shank bar where it was close to the knee connection while the other end connected to the ankle joint moment arm. The system was capable of providing full torque that was needed for a 75 kg subject walking up to 1.3 m/s at 1000 psig. While the overall weight of the system was not recorded, BLEEX was designed in such way that it was capable of carrying its own weight through its mechanical structure.

1.2.1.3 PNEUMATIC SYSTEMS

Pneumatics has been widely used in the field of robotics. Historically, its low cost, high power density and high natural compliance feature made pneumatics a popular option for powered orthoses. In fact, the first power orthosis in the 1960s used a pneumatic muscle [11].

Research teams under Ferris et al. at the University of Michigan initiated a series of studies using pneumatic powered AFOs [29-31]. The second generation AFO used a carbon fiber and polypropylene shell with two artificial pneumatic muscles attached to the anterior and posterior side of the shank shell to provide plantarflexion and dorsiflexion [29]. Total weight of the system was around 1.3 kg and it was able to provide ~57 % peak ankle plantarflexor torque with an average moment arm of 10.1 cm. Its average positive mechanical power was 0.23±0.02W/kg during level ground walking.

Walsh’s group had also developed a pneumatic version of the soft exosuit. The exosuit was designed using custom McKibben style pneumatic actuators [32]. The actuators were attached to the exosuit through a network of soft inextensible webbing. Each joint required multiple McKibben style pneumatic actuators to achieve the desired power output. This device had a total weight of 7.1 kg with peripherals but only 3.5 kg for the actual suit which resulted in low mechanical impedance and inertia to the lower limbs. The design was aimed to provide ~50 % of plantarflexor torque. Its total power output at the ankle joint was not recorded, but there was a 43.9 W reduction in average metabolic power when comparing walking with the powered suit to walking with the unpowered suit.

The Gen 1.0 and 2.0 PPAFOs developed by our group at the University of Illinois [6, 18] used off-the-shelf pneumatic bidirectional rotary actuators to generate approximately 12 Nm torque output at an operating pressure of 100 psig. Both PPAFOs weighed around 3.0 kg in total. While the peak power output for Gen 1.0 was not recorded, Gen 2.0 had a peak power generation of 50 W during gait [18]. The PPAFOs utilized small, compressed CO_2 tanks on a belt around the user's waist. The rotary actuators created a dorsiflexor torque for toe lifting during swing and eccentric deceleration at initial contact, and modest assistive plantarflexor torque at terminal stance phase. Both PPAFOs' actuators were directly aligned to the ankle axis of rotation through the support of carbon fiber shells had therefore had large lateral profiles due the off the shelf designs.

1.2.1.4 MECHANICAL SYSTEMS

While all the systems reviewed above were considered powered devices, pure mechanical systems can be considered as a power harvesting device. These types of systems are designed to either correct gait impairment or improve overall gait efficiency.

Our group developed a self-controlled pneumatic power harvesting AFO [33]. Ankle motion during swing phase was restricted through a locking mechanism actuated via a pneumatic circuit connected to a pump embedded under the forefoot. The pump was compressed by the body weight during stance and the compressed air was then used to engage the lock during swing to prevent foot drop.

Collins' group at Carnegie Mellon presented an unpowered exoskeleton [34]. This exoskeleton had a custom clutch spring system that behaved like calf muscles. The clutch held the spring as it was stretched when the foot was on the ground and releasing the stored power during push off. The system weighed between 0.408 and 0.503 kg depending on participant size. The power output of the device was not recorded however it reduced the metabolic cost of walking by around 0.21w/kg.

1.2.2 Existing Gait State Recognition Sensory Systems

The use of a gait state recognition system can provide gait monitoring and gait biofeedback. In this section, we review the sensors and gait detection methods used for gait monitoring not only in the field of powered orthoses but also in clinical applications such as monitoring daily activities and gait behaviors.

1.2.2.1 Sensors

The commonly found wearable sensors used for gait monitoring are: force based sensors (e.g. pressure insoles, force sensitive sensors) [6, 23, 35-37], joint angle measurement sensors (e.g. potentiometer, goniometer and Hall Effect sensor) [38-41], electromyographic (EMG) sensors [29, 30], and other inertial sensors such as accelerometer [42-47], gyroscope [21, 23, 48-50], as well as their combination which is known as an inertial measurement unit (IMU) [51-59].

1.2.2.1.1 Force based sensors

Among different sensors, footswitches such as force resistive sensors (FSR) were commonly used for force-based gait detection [6, 13, 35-37]. With FSRs mounted in shoe insoles, gait event detection could be achieved based on the threshold values obtained from the FSR. This type of sensor is low cost and easy to process. Although footswitches were widely used, there were still a few disadvantages. The number of detectable events was limited and the placement of the sensors on patients with pathological gaits affects its accuracy and reliability [50]. FSR's performance is highly depending on its placement. Wire connections subjected to repetitive load decreased the system service life [47]. A study also showed that heel strike detection using a FSR had a mean delay of 0.3-

3 percent of a gait cycle when compared with heel strike detection using force plate measurements [36].

1.2.2.1.2 Inertial sensors

With the advancement of micro-electromechanical systems (MEMS) and digital signal processing technologies, inertial sensors such as gyroscopes and accelerometers have quickly gained popularity since the early 2000s. Inertial sensors are miniature, durable, inexpensive, and highly mobile sensors. In addition, due to their very low electrical power consumption, the inertial sensors can be battery powered and are promising tools for long-term monitoring [50]. Moreover, with respect to solutions based on footswitches or foot pressure insoles, the analysis of the inertial sensors allowed researchers to recognize a greater granularity of events during the gait cycle, such as the sub-phases of the swing phase [60].

a) Accelerometer

Accelerometers provide the measurement of acceleration on its axes. MEMS accelerometers consist of a mass-spring system in a vacuum environment. It essentially uses the fundamentals of Newton's Laws of Motion [42] by measuring the displacement of the mass, which is proportional to the force acting on the mass, to compute the acceleration. By attaching an accelerometer to various body segments, such as the thigh, shank or foot, one can capture the continuous kinematic information of the leg during gait. In addition, previous studies also used accelerometers embedded in mobile phones [43] or smartwatches and wristbands [61, 62]. However, due to the random movements caused by phones or the upper extremities during gait, these embedded options were not preferred for gait state estimation for powered orthotic devices due to their relatively low accuracy. In general, the accelerometer was used to detect two gait phases: the stance and swing phases. The use of accelerometry data required additional signal processing due to the effects of gravity and jerky motions which would result in data drifting in a short period of time [47].

b) Gyroscopes

A MEMS gyroscope is an angular velocity sensor consisting of a vibrating element and sensing element. It is essentially capturing the Coriolis force which is generated do to the vibrating element proportionally to the angular velocity. The use of the angular velocity as a variable to perform gait partitioning reached greater popularity in recent decades [47] due to angular velocity being not easily influenced by gravity or vibrations caused by an intense movement such as heel strike [48]. Typical placement of the gyroscope was similar to the accelerometer. In gait analysis, the major contribution of gyroscopes is in their combination with accelerometers to compensate for accelerometer orientation errors.

c) Inertial measurement unit

The combination of more than one inertial sensor, such as gyroscope and accelerometer, has been referred to as an inertial measurement unit (IMU). An IMU consists of multi-axis gyroscopes and accelerometers enabling the tracking of rotational and translational movements. While a biaxial accelerometer and a uniaxial gyroscope can be used for measuring 1D orientation [63], triaxial sensors were needed to achieve 2D orientation [55, 59]. When it came to segment orientation or joint angle tracking for gait analysis, gyroscopes suffered from unknown initial joint angles and error accumulation in the integral value, while the accelerometer signal was sensitive to heel strike vibrations and gravitational force. A common solution to this problem has been to combine more than one inertial sensor [52]. IMUs are currently one of the most widely used types of sensors in gait analysis. Various sensor fusion algorithms also provided higher position and angle tracking accuracy [55, 64-66]. Therefore, IMUs have a great potential in the field of powered orthoses and exoskeletons.

In addition to an accelerometer and a gyroscope, another sensor that is commonly embedded in an IMU is a magnetometer. A magnetometer can be used to detect the Earth’s magnetic field, providing another reference measure for body 3D orientation [55, 66]. Unlike the accelerometer, the magnetometer signal is not affected by dynamic motions [67]. However, it is sensitive to the presence of metals and ferromagnetic materials [68]. Therefore, the presence of magnetic disturbances such as metal objects and house hold electronics may limit the performance of magnetometers for gait monitoring.

1.2.2.1.3 Goniometers

Goniometers can be used to track the angles of body joints. They are essentially operated by measuring the change in sensors' signals (e.g., resistance, the direction of the magnetic field, and, electrical pulses) resulting from the angular change. Commonly used mechanisms for goniometers are strain gauges, encoders, potentiometers and Hall Effect sensors. Goniometers are capable of providing continuous measurement during gait.

1.2.2.1.4 Electromyography (EMG)

EMG signals can be used to measure the action of the muscles in the lower extremity. It is less popular due to higher complexity in data acquisition and post-processing [47]. In addition, while working with impaired populations, collecting EMG signals is not necessarily an easy task to accomplish, especially in populations with neuromuscular impairment [69]. Studies also indicate that, in the powered AFO application, EMG amplitude tends to reduce over time due to subject adaptation [70].

1.2.2.2 Gait detection methods

Identifying when a sensor reading crosses a set of thresholds (e.g. local maxima, minima and threshold-crossing) is the most common method for detecting gait events used due to their capabilities of real-time detection and ease of implementation [67]. Sensors such as insole FSR, gyroscope and accelerometer are capable of differentiating stance phase and swing phase by detecting HS and TO events [36, 44, 49]. Shorter et al. initially proposed a direct event (DE) controller that used FSRs in the PPAFO sole to divide the gait cycle into four gait states (1.loading response, 2.mid stance, 3.terminal stance through pre swing, and 4.swing). Li et al. proposed a Fractional Time (FT) state estimation approach that depended only on the rising edge of the heel FSR sensor data to define the heel strike event [71]. The percentage of the gait cycle was then estimated following the heel strike event. This approach was slow in adjusting to changing gait speed because it only detected the heel strike event. Similar to the DE method, Mooney et al. proposed a finite state machine technique which used threshold detection and zero-crossing detection to detect the swing phase and the heel strike event [23]. A series of power timers were also used to further divide the gait cycle into more sub-states for controlling their ankle exoskeleton (i.e., controlling the actuator until a predetermined timer expired). However the sub-states were still relying on the initial threshold detection. Ferris et al. used electromyography (EMG) signals of the tibialis anterior muscle and the soleus muscle for tracking gait states and controlling AFO [29]. Upon reaching a threshold, a proportional myoelectric control was applied to their powered AFOs.

Furthermore, pattern similarity matching and machine learning are two major advanced gait detection methods that provided more accurate gait detection. For similarity matching, methods such as curve-aligning and pattern fitting [41, 46, 71, 72] were commonly used. Pattern fitting was performed by methods such as k-nearest neighbor (kNN) and correlation [71, 72]. Li et al. proposed state estimation methods that used the cross correlation (CC) and kNN between sensor signals and a regression model learned from training data [71]. Both methods were able to divide the gait cycle into 100 states. Islam et al. [41] proposed the Modified Fractional Time (MFT) estimator utilizing both heel and toe FSRs and an additional ankle angle sensor (Hall Effect sensor). MFT was able to detect up to eight events within a single gait cycle by comparing the captured data with a trained vector. Several machine learning techniques have been used to detect gait events, such as Artificial Neural Networks (ANN) [41], and Gaussian Mixture Model (GMM) [73]. The GMM method was used to discriminate stance and swing phases, while the ANN method proposed by Islam et al. used a moving window of six continuous data points estimating states across the gait cycle. Advanced algorithms and multi-sensor configurations showed improvements in terms of accuracy and number of detectable events. However, some of these algorithms either cannot achieve satisfactory control for AFOs due to heavy computing and delays in classification process [38, 71], or a model of the events was necessary to identify gait event [38, 41, 73]. With the increasing number of sensors introduced to gait monitoring systems, the complexity of these systems increased [20] due to their complicated data collection protocols and computationally expensive algorithms.

1.3 MOTIVATION FOR PROPOSED STUDIES

1.3.1 Study 1: A COMPACT HIGH TORQUE ACTUATION SYSTEM FOR A PORTABLE POWERED ANKLE-FOOT ORTHOSIS

As mentioned previously, our group had developed multiple generations of the portable pneumatically powered ankle-foot orthosis utilizing off-the-shelf components [6, 18]. These devices were designed for untethered operation away from the confines of a lab or treadmill by use of a portable pneumatic power supply. However, since the off-the-shelf actuators were not designed for portable application, the systems had lower torque outputs and large lateral profiles. So our goal for the first study was to develop a compact higher torque PPAFO (Gen 3.0). The development of a lower profile and higher torque generating PPAFO has the potential to increase the mobility and enable further investigation on how powered plantarflexor torque magnitude impacts gait function.

1.3.2 Study 2: MINIMUM SENSOR CONFIGURATION FOR GAIT EVENT DETECTION FOR A PORTABLE POWERED ANKLE-FOOT ORTHOSIS

The use of gait detection devices can provide gait monitoring and gait biofeedback. One major benefit of gait monitoring for lower-limb powered orthoses is its ability to collect gait information and make control decisions on board in real time, such that the ankle torque actuation control policies can be designed to accommodate the short-term changes in gait speed and/or gait mode. There were many studies investigating low-cost, robust wearable sensors that could potentially be used for gait event detection. However, with the increasing number of sensors and gait detection methods introduced to gait monitoring systems, the complexity of these systems could also be increased [74] due to the intricate data collection protocols and computationally expensive algorithms. To the author's knowledge, there has been no systematic study on the simplest cost-effective and robust sensor configuration for robust gait monitoring in a powered AFO. So as our goal for the second study, we were interested in investigating the minimum sensor configuration that would be needed for robust gait event estimation.

1.4 THESIS OVERVIEW

The study presented in Chapter 2 covers the design and evaluation of the Gen 3.0 portable powered ankle-foot orthosis (PPAFO). The Gen 3.0 PPAFO utilized two dual-action linear pneumatic actuators and customized compact gear train to provide plantarflexion and dorsiflexion actuation to the ankle joint. The new system was capable of providing higher torque and power output while reducing the lateral profile compare with the earlier generations. Next, a study on the investigation of the minimum amount of sensors that were needed for better gait event detection is presented in Chapter 3. Multiple sensors were compared (FSRs, potentiometer, IMU). The study focused on single sensor and double sensor configurations to identify the minimal number of sensors required to perform robust gait event detection. Lastly, in the final chapter, we discuss the conclusion and the future directions of the studies described in this thesis.

Chapter 2:

A COMPACT HIGH TORQUE ACTUATION SYSTEM FOR A PORTABLE POWERED ANKLE-FOOT ORTHOSIS

Abstract

The portable powered ankle-foot orthosis (PPAFO) is capable of providing bidirectional assistive torque at the ankle joint. To create the ankle torque, the previous design utilized an off-the-shelf rotatory pneumatic actuator (560 g) capable of generating up to 12 Nm torque and 50 W power at an operating pressure of 100 psig. This torque value is 17% of the peak ankle torque that an 85 kg healthy walker can generate. An increased torque may help to improve gait function. In this chapter, we present the design and evaluation of a new actuation system for the PPAFO. The actuation system utilized two dual action linear actuators and a customized gear train. Compared with the previous design, it generated higher torque and power while providing a thinner lateral profile. The new design had a total weight of (680g) and was capable of generating 32 Nm torque and 110 W power. While running under the same torque and power level, the new design offered better longevity (42.9% and 81.4% increases in normalized run time for test bench emulation and treadmill walking). Although the overall weight of the new actuation system had a 20% increase compared with previous design, it could generate 166.7% more torque and 120% more power which will enable us to test the system at various torque and power settings.

2.1 Introduction

An ankle-foot orthoses (AFO) is an orthotic device used to correct mobility disorders that cause impairments to the lower legs. Conventional passive AFOs provide functional assistance during gait by restricting unwanted motion of the foot [75]. However, the restricted motion and passive properties of conventional AFOs can impede gait and cannot adapt to a changing environment[76]. Therefore, powered AFOs capable of providing assistive torque at the ankle joint have significant potential as both assistive and rehabilitative devices [6].

Novel powered AFOs have been developed to provide assistance to the ankle joint for motion control and torque assistance [6]. The development of joint power had been achieved through electrical [21, 22, 40], hydraulic, [13, 27] and pneumatic systems [6, 29, 32]. One research group at the Carnegie Mellon University recently developed two different electrically powered, tethered designs [40]. Both designs were powered with an off-board motor. The peak torque during pilot testing was 121 Nm. The peak power of the system was not recoded; however it was reported to be capable of providing high torque at high bandwidth with accurate torque tracking. Though the systems were able to provide full torque assistance, their tethered design constrained the testing environment to be indoor only. Another group at the Massachusetts Institute of Technology had developed an active plantarflexion leg exoskeleton using brushless DC motors [22]. The peak torque and power of the exoskeleton were estimated to be 70 Nm and 180 W [22]. While electrical systems demonstrated the ability to generate high power or torque output, either tethered design or significant amounts of weight and inertia were introduced to the system in order to house the actuators, batteries, and controllers [25]. High inertia systems at the extremities of the user may hinder motion, especially in subjects with a mobility disorder [21, 77]. The research group at the University of Minnesota developed a hydraulic AFO which was capable of generating 90 Nm torque [27] and the system was designed to generate a peak power of 100 W [26]. One limitation about the hydraulic design was its low bandwidth (actuation speed). Hydraulic cylinders are often used for low velocity and large linear force generation [27]. Therefore, the system's performance may be limited to meet normal gait speed requirements.

Pneumatic systems, in contrast, possess a number of assets such as high natural compliance due to compressibility and low cost, while maintaining a relatively high power density. A research group at the University of Michigan developed multiple light weight pneumatic powered AFOs. Their second generation AFO was able to provide 60 Nm plantarflexor torque [29]. The system's peak power generation was not recorded. The total weight of the system was 1.7 kg. Our group at the University of Illinois also developed multiple generations of the portable powered ankle-foot orthosis (PPAFO) using pneumatic power [18, 78-80].

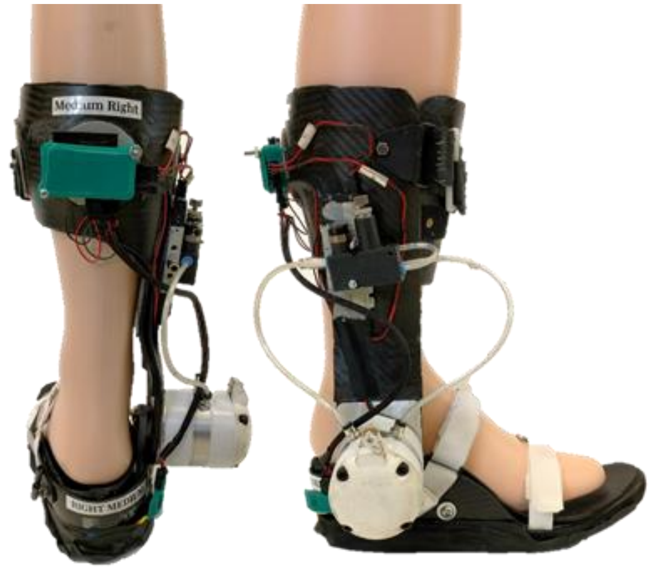

FIGURE 3 GEN 2.0 PPAFO DESIGN

A PPAFO is able to provide bidirectional assistive torque at the ankle joint (dorsiflexion or plantarflexion). The Gen 1.0 and Gen 2.0 PPAFOs have served as testbed platforms for investigating the effect of a powered orthosis on able-bodied and impaired gait [6, 18, 78-82]. Both designs were untethered, allowing it to be used outside of a lab setting by the use of a portable pneumatic power supply. To provide ankle torque, the Gen 2.0 design (Figure 2) used a dual-vane bidirectional off-the-shelf rotatory actuator (PRN30D-90-45, Parker Hannifin, Cleveland, OH). The most recent design, Gen 2.0 PPAFO system, weighed 3.1 kg including power source and had a peak power generation of 50 W at 100 psig during gait [18]. The peak plantarflexor torque was 12 Nm for 100 psig input pressure, which is 17% of the peak ankle torque that an 85 kg healthy walker can generate [19] (Figure 4). In addition, the off-the-shelf rotatory actuator had a large and undesirable lateral profile (Figure 2&Table 3). The bulkiness of the actuator made it difficult to be concealed underneath clothing and increased the risk of interfering with the surrounding environment during gait. Therefore, other options that provide high power and compact designs were needed.

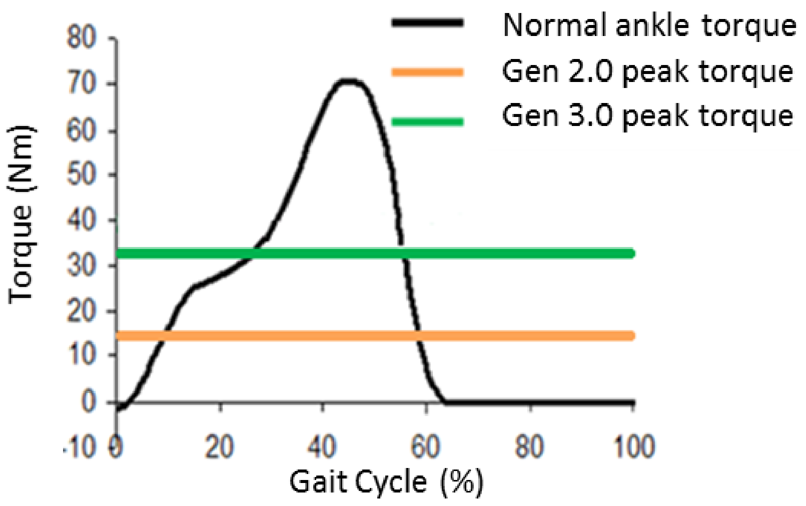

Figure 4 Peak Torque Generation for healthy 85 kg walker. Figure adapted from [19]

compared to output of Gen 2.0 & Gen 3.0 PPAFO at 100 psig operating pressure

We collaborated with several senior design teams at Bradley University aiming to design a working, compact, and efficient actuator for a powered ankle orthosis [83-85]. The design developed by the 2013-2014 school year team [85] used two dual-acting pneumatic air cylinders (091.092-D; Bimba Manufacturing; University Park; IL; USA) to increase the overall piston area (Figure 5). By putting the linear actuators against the lateral side of the shank, the overall effective piston area (EPA) was distributed in the transverse plane along the anterior–posterior direction to reduce the lateral profile of the actuation system. The linear motions of the pneumatic cylinders (contraction, extension) were synchronized by connecting to a custom-made connector block (yoke) and then converted to rotatory motions through a rack and pinion compound gear system. The design had an overall gear ratio of 4:1 and a compound gear with an input gear (IG) to output gear (OG) gear ratio of 1:1 (Figure 5). This design resulted in a large 4 inch pitch diameter (PD) for the sector gear (SG) to achieve 55˚ range of motion (ROM) at the ankle joint.

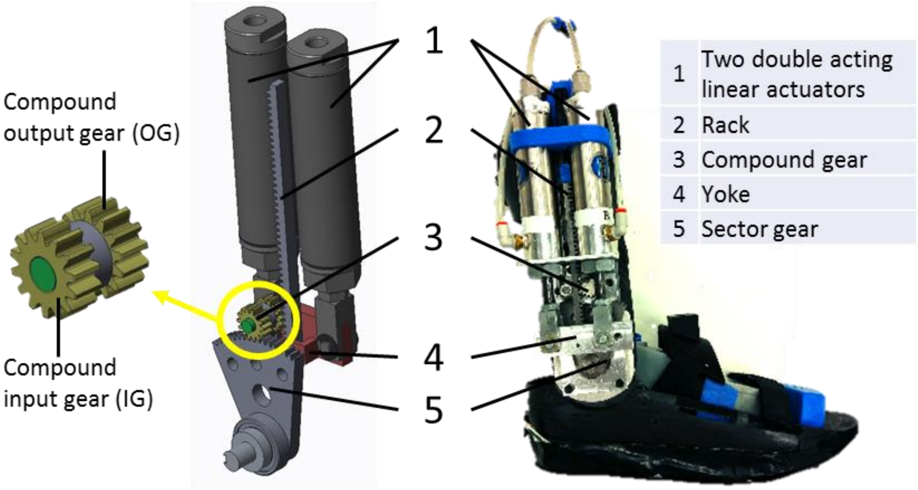

FIGURE 5 2014 DESIGN

The 2014 design compared with the Gen 2.0 PPAFO successfully demonstrated a reduced lateral profile at a cost of increased system weight and profile. In addition, more moving components (gears, rack, and yoke) were introduced to the system with the rack and pinion compound gear design which could increase the risk of injury for users. Therefore, further modifications were needed to optimize the system.

In this chapter, we present the design and evaluation of a compact, high power and torque actuation system for the Gen 3.0 PPAFO. The main objective of the new system design was to increase the maximum torque output while minimizing system volume and weight so that further studies can be conducted through a range of torque settings. This range will allow us to understand how torque magnitude impacts gait function. The new actuation system's physical properties and performances were evaluated in comparison to those of the Gen 2.0 design. For the performances evaluation, a gas consumption (longevity) study was conducted using the Gen 3.0 PPAFO powered by compressed CO_2 tanks. This analysis of compressed gas was performed using both treadmill walking and a test bench setup created to emulate the timing of a walking condition. One able-bodied male subject was tested while walking on a treadmill with the assistance of Gen 3.0 PPAFO. Test bench testing and treadmill testing both used the same Gen 3.0 PPAFO and sensors for data collection.

2.2 Methods

This section is divided into two parts: the first part presents the Gen 3.0 PPAFO hardware design and the second part describes the system evaluation conducted on both a treadmill and a test bench created to emulate the gait cycle.

2.2.1 Gen 3.0 PPAFO Hardware Design

2.2.1.1 Design specifications

The minimum desired torque output and range of motion were 30 Nm and 55 °, respectively. The lateral profile should be less than 5.1 cm to be wearable within a pair of slacks.

2.2.1.2 Actuator configuration

For the actuator configuration, the two dual-action linear actuator concept was adapted from the 2014 Bradley design. For a pneumatic system, the force generated by a piston is proportional to the effective piston area (EPA). Therefore, the bigger the EPA, the higher the force that the actuator could generate while keeping pressure constant. However, for a single linear actuator design, a bigger

EPA also means a bigger lateral profile. The two linear actuator configuration, on the other hand, could distribute the overall EPA by dividing it between two actuators. For a linear actuator, the EPA in the retract chamber is smaller than that in the extend chamber due to the existence of the piston rod. The resulting retraction force is lower than extension force while under the same chamber pressure. Thus the piston's extension force was used to assist plantarflexion because human plantarflexor torque is much higher than dorsiflexor torque [2]. Both air cylinders had a stroke length of 4.9 cm (1.92 inch) and were synchronized by connecting to a custom yoke (Figure 6.b).

2.2.1.3 Compound gear system

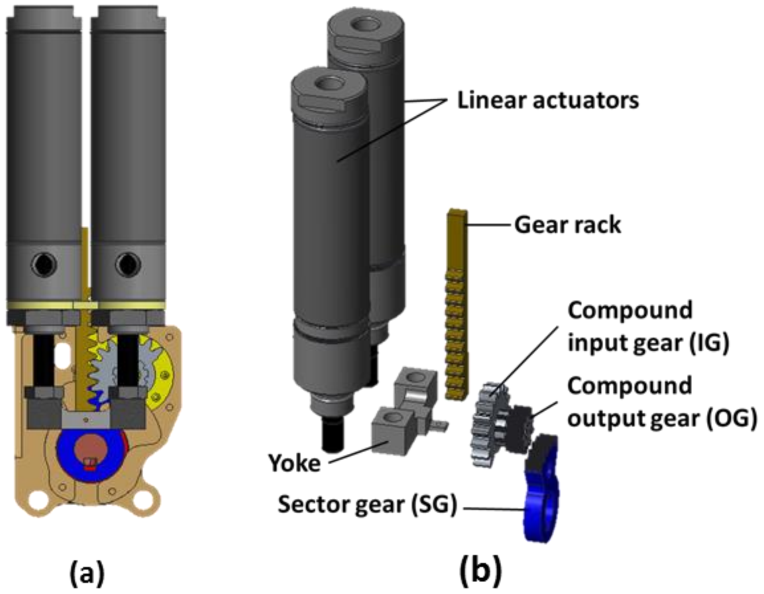

FIGURE 6 ASSEMBLY VIEW (a) AND EXPLODED VIEW (b) OF THE GEN 3.0 PPAFO'S ACTUATION SYSTEM

For a compound gear system (Figure 6), the gear ratio is equivalent to the product of the pitch diameters (PD) of the driven gears divided by the product of the PDs of the driving gears [86]. According to our design concept, compound input gear (IG) and sector gear (SG) are driven gears and compound output gear is a driving gear. The system's equivalent gear ratio was then defined as:

$$\mathrm{R_{eq}} = \frac{\mathrm{PD_{IG}} \cdot \mathrm{PD_{SG}}}{\mathrm{PD_{OG}}} \qquad (1)$$

where:

R_{eq} = equivalent gear ratio of entire system.

Thus, either enlarging $\mathrm{PD_{IG}}$ or reducing $\mathrm{PD_{OG}}$ will reduce the required $\mathrm{PD_{SG}}$ (Figure 6) while maintaining a constant overall gear ratio and a 55˚ ROM. It was hypothesized that there might exist a combination of PDs to result in minimization of gear combination's weight and profile. However both options mentioned above will also increase the mechanical advantage of the compound gear. The tangential load between the SG and compound OG will increase and then raise the gears' root fillet stress [86]. Therefore, additional design considerations had to be taken into account in order to prevent mechanical failure.

Other factors that could affect the root fillet stress are pressure angle (PA) and diametral pitch (DP) [86]. The 2014 design utilized 1215 carbon steel gears with a standard 14.5˚ pressure angle (PA), 24 diametral pitch (DP). Surface wear was noticed after laboratory testing. Prior work showed that high PA of 35˚ resulted in lower stresses and were mostly compressive, leading to good fatigue resistance [87]. A larger than standard PA could both increase efficiency and reduce surface wear by decreasing the amount of sliding between teeth [87]. Therefore, in addition to the standard gear PA of 20˚ and 14.5˚, a 35˚ PA was considered.

Due to the OG's smallest PD in the system relative to all other gears, and the higher tangential loads anticipated at the OG-SG interface, the OG would be the most likely point of failure in the system. Therefore, we focused on OG to identify the strongest possible gear geometry. $\mathrm{PD_{OG}}$ was first constrained accordingly as a starting point from which the PA and DP combination could also be determined. 2014 design had a $\mathrm{PD_{OG}}$ of 0.54 inch. Therefore, we chose to compare a smaller

0.5 inch PD_{OG} at different PA and DP settings. As a basis of comparison, a 12 tooth OG was chosen for the 24 DP gear set. A 10 tooth OG for 20 DP, and a 9 tooth OG for 16 DP were also selected.

Upon completing the potential gear geometries, stress analysis was performed to identify maximum stress of each combination. For the stress analysis, we chose to use both analytical (American Gear Manufacturers Association (AGMA) corrected Lewis equation) and numerical approaches (Finite Element Analysis (FEA) in Creo 3.0). A maximum acceptable pressure of 120 psi was set for the worst-case scenario because it was the maximum documented pressure pf our previous designs [17, 82]. The rack load at 120 psi is expected to be about 216 lbs (pressure times EPA). Thus, the tip load for OG was set as 432 lbf which was the maximum load corresponding to a 2:1 compound gear ratio. The AGMA corrected Lewis equation is [86]:

$$\sigma = \frac{F_t \, DP}{b \, J} \cdot K_v \, K_O \, K_m \qquad (2)$$

where:

J = spur gear geometry factor [87] (0.2 for 14.5˚ PA, 0.21 for 20˚ PA, and 0.25 for 35˚ PA)

DP = diametral pitch

F_t = tangential load on spur gear 432 lbf

b = face width 0.25 inch

K_v= dynamic factor which punishes for high velocity approximated as 1 because pitch line velocity for the system is expected to be very low [86]

K_O = overload factor also approximated as 1 due to the inherent compliance and shock absorption of the pneumatic system [86]

K_m = mounting factor was set to 1.2 for accurate mounting narrow face width and small bearing clearances, etc. [86]

FEA in PTC Creo 3.0 was used to represent a conservative upper limit gear stress by modelling tip loaded tooth with no load sharing amongst neighboring teeth [88] (Figure 7). This condition would never occur in actual gears due to load sharing between teeth. Models of gears used in this software analysis were constructed in Creo 3.0 from DXF profiles constructed in Dr. Rainer Hessmer's Involute Spur Gear Builder web application [89].

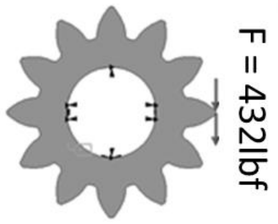

FIGURE 7 : FEA LOAD AND CONSTRAINS. MATERIAL PROPERTIES (AR500) FOR FEA WERE DEFINED AS FOLLOWS: ELASTIC MODULUS = 200 GPA. POISSON'S RATIO = .25. THE INNER BORE OF THE GEAR WAS CONSTRAINED TO 0.0 DISPLACEMENT AND A 432 LBF TIP LOAD WAS APPLIED TO ONE GEAR TOOTH.

Results for constant tip load were determined (Table 1). A 35˚ PA and 16 DP gear resulted in a lowest root fillet stress (133ksi). Therefore we chose to use a 35˚ pressure angle for all of our customized gears.

TABLE 1 MAXIMUM ROOT FILLET STRESS OF COMPOUND OUTPUT GEAR AT DIFFERENT DIAMETRAL PITCHES AND PRESSURE ANGLES

DP	PA(˚)	AGMA Lewis equatoin root fillet stress (ksi)	FEA worst case root fillet stress (ksi)
24	14.5	249	370
24	20	237	331
24	35	199	229
20	14.5	207	349
20	20	197	326
20	35	166	215
16	14.5	166	284
16	20	158	235
16	35	133	189

With the knowledge of the proper PA of the gears, we moved on to the size selection of the compound IG and SG to achieve the optimal weight reduction. As was mentioned previously, enlarging the compound IG’s diameter would reduce the required diameter of the SG while maintaining a constant overall gear ratio and 55˚ ROM. It was assumed that the total surface area of the gear set was proportional to the total weight of the gear set due to the uniform gear thickness (0.25 inch) and material density (steel: 4.5oz/inch^3). Therefore, total surface area with respect to each IG-SG combination was compared (Table 2, formula see Appendix A). The combination of an 18 tooth IG and 32 tooth SG was chosen, as it had the same overall gear ratio with the 2014 design (gear ratio 4:1) and a low overall surface area. The lower limit for the number of the SG teeth was set at 32 due to the maximum tangential load reached 432 lbf.

TABLE 2 OVERALL SURFACE AREA OF DIFFERENT GEAR SET

compound IG tooth count	corresponding SG tooth count	overall gear ratio	surafe area (cm2)
14	40	3.89	11.03
15	39	4.06	11.10
15	38	3.96	10.84
16	37	4.11	10.90
16	36	4.00	10.71
16	35	3.89	10.45
17	34	4.01	10.52
17	33	3.90	10.32
18	32	4.00	10.45

This optimized the weight of the gear train. In addition, the reduced overall profile also motivated the design of a gear box housing (Section 2.1.3). With the gear train being enclosed, the moving components will be less likely to interfere with the surround environment.

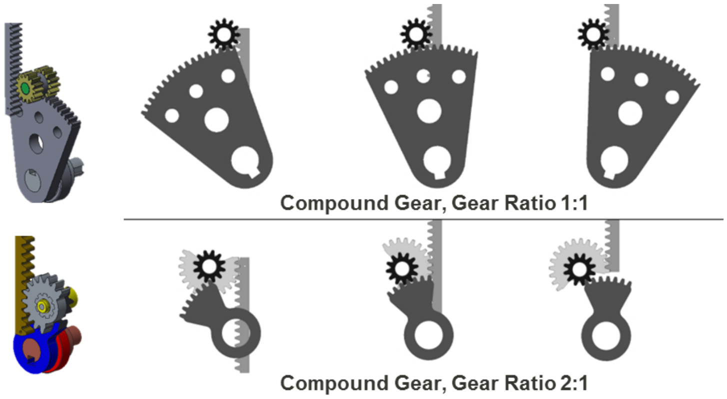

FIGURE 8 COMPOUND GEAR DESIGN COMPARED TO 2014 DESIGN

TOP: 2014 GEAR MECHANISM THROUGH FULL RANGE OF MOTION.

BOTTOM: GEN 3.0 DESIGN THROUGH FULL RANGE OF MOTION.

A list of materials were examined for manufacturing the customized gear. During this process the strength of the materials and manufacturability were considered. AR500 steel was selected for a gear prototype due to its high yield strength (187ksi) and availability off the shelf in the right thickness and annealed state. All other alternative materials that had higher yield strength required proper heat treatment which would complicate the manufacturing process. Gears were cut via a wire electric discharge machining (EDM). The high precision and small cutting diameter of EDM made this manufacturing process suitable for the gears needed. The small heat affected zone at the cutting surfaces required polishing because the surface roughness resulting from the cutting process may otherwise affect reliability of the gears [90].

2.2.1.4 3D printed gearbox

A new gearbox was designed to contain the gear train. The 2014 design simply used an aluminum mounting plate for the gear train that resulted in heavy system weight and exposure of moving components. Therefore, a gearbox (Figure 9) was designed to reduce the weight of the gear housing while fully enclosing the moving components. For producing the gear box, rapid prototyping techniques, specifically 3D printing stereolithography (SLA) technique was used due to its high accuracy, low weight, and fast prototyping. A light weight and low cost material (Somos 18420) was chosen to fabricate the gearbox casing. With a proper post-curing operation, a tensile strength of 66-68 MPa can be obtained. Though the true yield strength of the part was unknown due to the complex printing technique and thermal-deformation, structural reinforcements were applied to minimize internal stress of the gearbox. Aluminum inserts (Figure 9.a) with tapped holes were used to reinforce the mounting of the aluminum cylinder holder (Figure 9.e) so that the mounting bolts could avoid contacting the 3D printed case while still providing rigid attachments to the gearbox. The gearbox was designed to fit the mounting holes on the orthotic shell so that the Gen 2.0 and Gen 3.0 actuation systems were interchangeable. A lubrication channel (Figure 9.g) was also added to the case to provide oxidation resistance and wear reduction for the gear system.

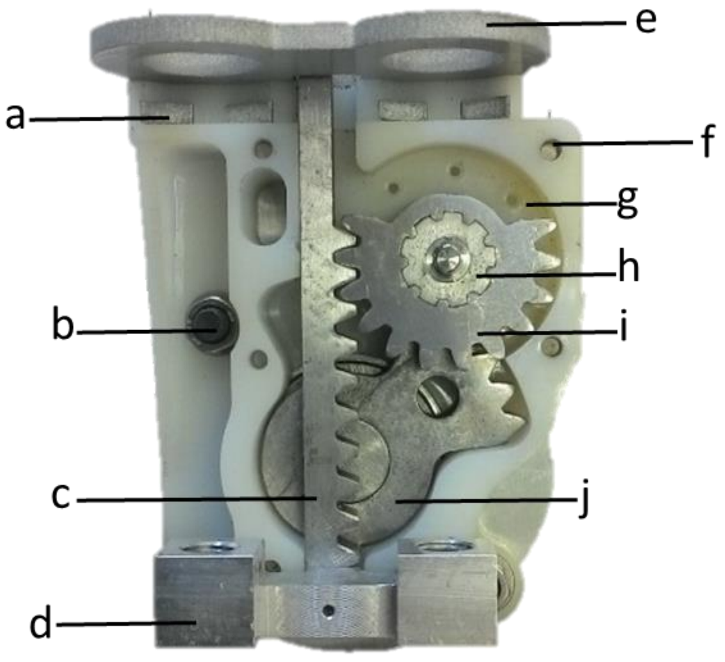

FIGURE 9 SIDE VIEW OF 3D PRINTED GEARBOX (A) LINEAR ACTUATOR MOUNTING REINFORCEMENT/ALUMINUM INSERT, (B) LEG SHELL MOUNTING HOLES, (C) GEAR RACK, (D) YOKE, (E) ALUMINUM CYLINDER HOLDER, (F) TAPPED FRONT COVER MOUNTING HOLE, (G) LUBRICATION CHANNEL, (H) COMPOUND DRIVER GEAR, (I) COMPOUND DRIVEN GEAR, (J) SECTOR GEAR.

An FEA analysis was conducted to estimate the potential stress of the gearbox design (Appendix B). The maximum input force (i.e., push force (Pf)) in this analysis was set equal to the force generated by the linear actuators when both linear actuators' extend chambers were pressurized to 100 psi. The resulting maximum push force applied to the gear rack from linear actuators was about 180 lbf (pressure times extend chamber EPA). Material properties (Somos 18420) for FEA were defined as follows: Tensile Strength = 68 MPa, Elastic Modulus = 2960 MPa, and Poisson's ratio = 0.42 [91]. The four mounting holes were constrained to 0.0 displacement. A maximum stress of 63.0 MPa was observed (Figure 10).

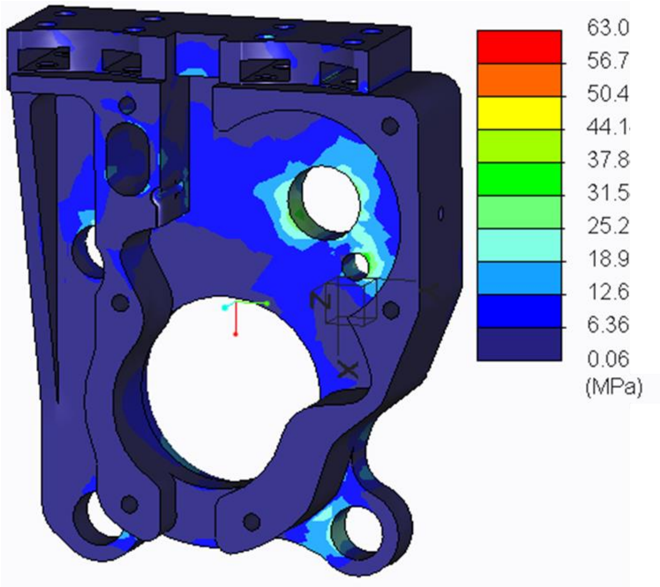

FIGURE 10 FEA RESULT OF THE GEARBOX AT THE PISTON LOAD OF 180 LBF.

2.2.2 Experimental evaluation

The evaluation of the Gen 3.0 was conducted by comparing its physical properties and performances with the Gen 2.0 design.

The physical properties analysis of the Gen 3.0 system included its dimensions, overall weight, maximum chamber volume, and torque output (Figure 11). The maximum chamber volume of Gen 3.0 was calculated using extend chamber EPA (11.55 cm^2) times stroke length (4.88 cm). A static torque measurement was conducted using a uniaxial force gauge (DFG35-10, Omega Engineering, Stamford, CT). The actuator was attached to an aluminum stand using the four bolts that would normally attach to the leg shell. The force gauge was locked to a bolt that was screwed into the triangle plate, which was normally used to attach to the foot shell. The force gauge was clamped perpendicular to the lever arm between the actuators' axis of rotation and the line of action of the force (Figure 11 b&c).

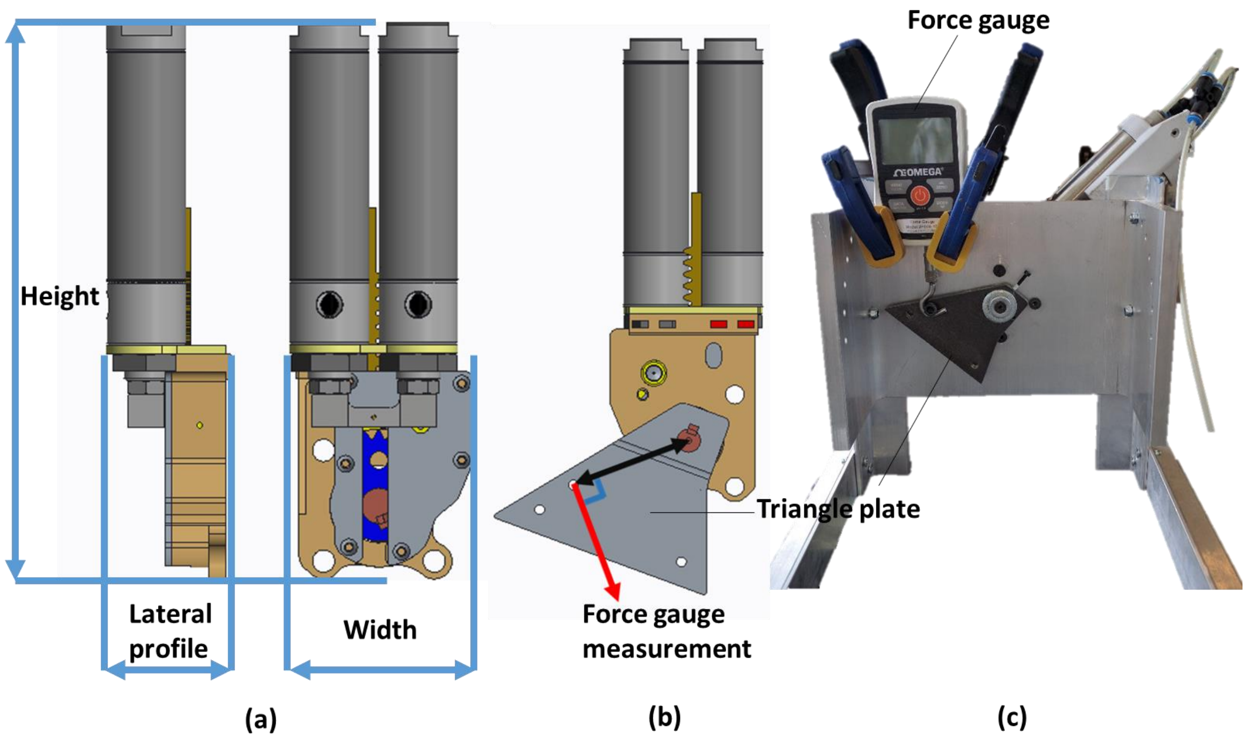

FIGURE 11 DEFINITION OF THE PHYSICAL DIMENSIONS (a) AND TORQUE MEASUREMENT SET UP (b&c)

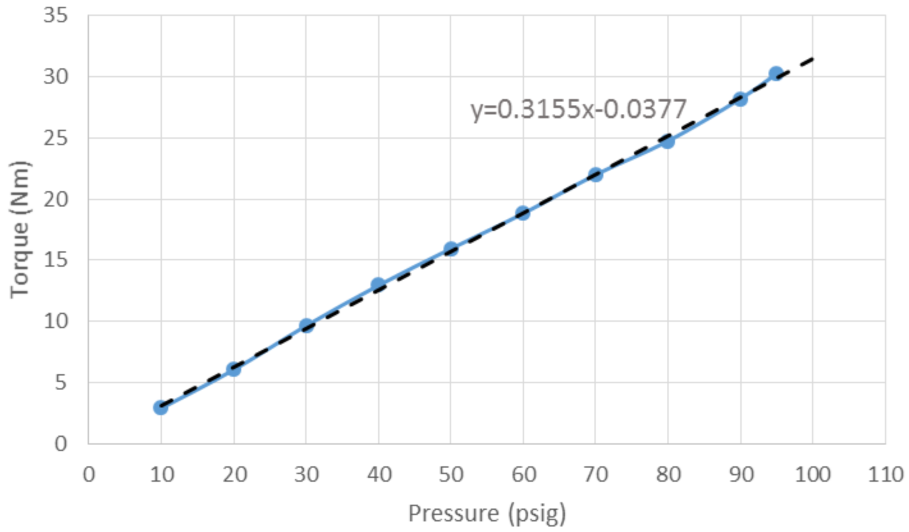

FIGURE 12 TORQUE MEASUREMENT RESULT

To compare the system performance, we conducted a gas consumption (longevity) study on both a treadmill and a test bench created to emulate the walking condition. For the treadmill testing the Gen 3.0 PPAFO's performance was recoded then compared with that of the Gen 2.0 PPAFO [78]. For the test bench testing, both Gen 2.0 and Gen 3.0's performances were recoded then compared.

2.2.2.1 Test bench emulation

The experimental test bench setup consisted of a mock leg and shank with 3D rotational freedom at the ankle joint and 1D sagittal plane rotation at the knee joint (Figure 13). The inertial properties of a mock foot were based on anthropometric data from 50th percentile male (similar to the properties of the able-bodied subject tested in treadmill walking). A rigid aluminum mounting fixture was used because it provided a more controlled environment for the system comparison with Gen 2.0 PPAFO. See Appendix C for details of the off-the-shelf components.

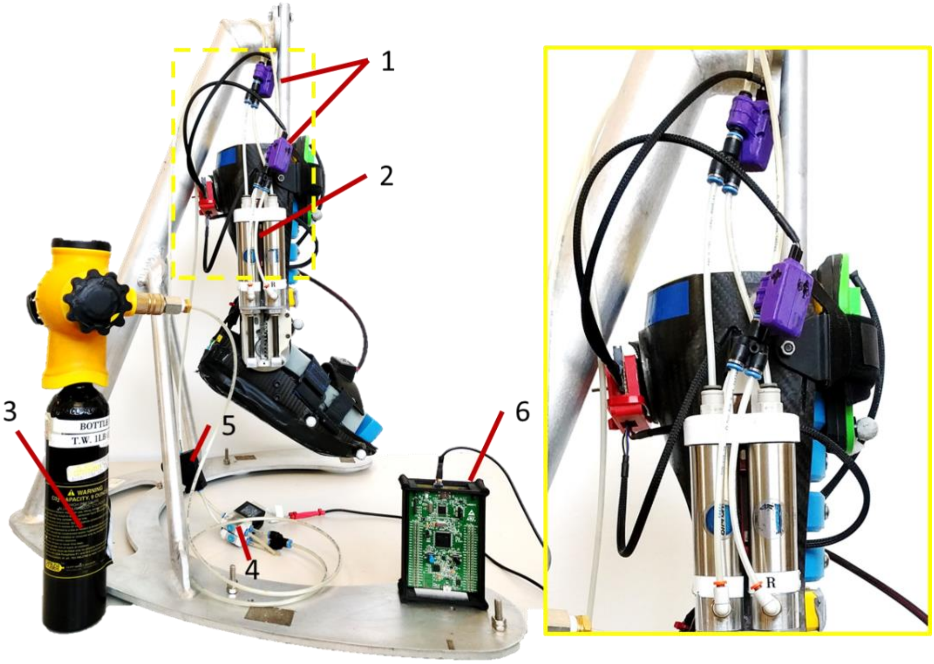

Figure 13 Test bench setup 1) Pressure sensors, 2) Ankle angle sensor, 3) 9oz CO_2 bottle, 4) solenoid valves, 5) dorsiflexion regulator, and 6) Controller & data acquisition box.

For the test bench trials, the onboard microcontroller (STM32F407VG; STMicroelectronics, Geneva, Switzerland) was programmed to simulate a 1 Hz gait cycle (GC) based on healthy normative adult walking timing (dorsiflexion: 0-7 %GC and 62-100 %GC, plantarflexion: 48-62 %GC, no pressurized state: 7-48 %GC) [2, 18]. Two fast switching solenoid valves (MHE2-MS1H- 3/2O-QS-4; Festo Corp US; Hauppauge, NY) were used to control the pressurization and depressurization of the actuators. A pressure regulator (LRMA-QS-4; Festo Corp-US, Hauppauge, NY) was mounted in-line with the retract chambers to reduce the input pressure to ~14.5 psig (1 bar) and achieve the desired smaller dorsiflexor torque. Two pressure sensors (TBPDANN150PGUCV; Honeywell; Morristown, NJ) were also placed in-line with both extend and retract chambers to track the chamber pressure. 9 oz CO_2 bottles (Catalina Cylinders, Hampton, VA) were used, to control the amount of gas consumed within each trial. A linear potentiometer (MP1-L-0050-103-5%-RH;

Spectrasymbol; Salt Lake City, UT) was used to track the movement of the piston. The microcontroller board was set at 500Hz sampling frequency to record data from all sensors. The CO_2 bottles were filled to their maximum capacity (9 oz + bottle tear weight) before use. Each trial started with a full bottle and ended when the actuators could no longer complete the normal range of motion. Time (in s), number of completed cycles (i.e., number of steps) and bottle weight (in g) were recorded at both the beginning and the end of each trial for measurements of runtime. Internal chamber pressure (in Pa) of each actuator and actuator piston motion (in m) were also recorded for measurements of system power output. The pressure sensors used were custom made utilizing an instrumentation amplifier (AD623 AN, Analog Devices, Norwood, MA) and a board mounted pressure sensor (TBPDANN150PGUCV, Honeywell, Morris Plains, New Jersey). Details for pressure circuit and housing can be found in Appendix D.

Two testing conditions with different bottle pressures were evaluated for Gen 3.0 design. Six bottles were regulated down to two different pressure levels (38 and 100 psig) to simulate two types of peak plantarflexor torque outputs (12 and 32 Nm); thus, three bottles per condition were tested. The lower pressure condition was regulated to reproduce the plantarflexor torque output of the Gen 2.0 PPAFO at 100 psig, while the higher pressure condition was for testing the full capacity of the Gen 3.0 PPAFO.

For the test bench comparison, Gen 2.0's performance was also evaluated. We used the same test bench setup as the Gen 3.0 design. Three 9 oz bottles were regulated to 100 psig for Gen 2.0 to have a peak torque output of 12 Nm. The total runtime and mass consumed were recorded.

2.2.2.2 Able-bodied treadmill walking

To evaluate the performance of the Gen 3.0 PPAFO, able-bodied treadmill waking test was also conducted. All procedures were approved by the institutional review board of the University of Illinois. The subject was given informed consent. One able-bodied male subject (age 27 years, height

178 cm, weight 80 kg) was tested while walking on an instrumented treadmill (Bertec Corp., Columbus, OH) with the assistance of Gen 3.0 PPAFO. The subject walked on the treadmill while wearing the Gen 3.0 PPAFO on his right leg and his personal running shoe on the other leg. The subject was encouraged to maintain a 1 Hz step rate with the help of a 60 bpm metronome. The PPAFO actuation timing was controlled by the a fractional time controller [71] with the same actuation timing used for the test bench emulation. Three 9 oz CO_2 bottles were also used during treadmill walking. The trial ended when the subject no longer felt any assistance from the PPAFO. The total consumed mass of CO_2 (in g), the total walking time (in s) and number of steps were recorded.

2.2.2.3 Data Analysis

For both treadmill walking and test bench testing, the normalized runtime (min/g) and mass consumption per step (g/step) between Gen 3.0 and Gen 2.0 designs were compared. Normalized runtime was calculated as total runtime divided by the total mass consumed. Mass consumption per step was calculated as total mass consumed divided by the total number of steps.

In addition, the power output (in W) was derived by tracking the piston velocity (in m/s) and pressure in the actuator of the Gen 3.0 PPAFO. The raw piston velocity was calculated using the difference between piston position measurements divided by the sampling time (2ms). The raw piston velocity was then filtered with a 4th order Butterworth low pass filter with a cut-off frequency of 10Hz. Power output indicates the amount of assistance per sampling time given to the wearer of the device. Pressure sensor outputs (in Pa) and effective pistons area (EPA, in m^2) were used to calculate the net force (in N) generated by the actuator piston. The equation for calculating power was:

$$\text{Power}= (P_\text{e}\,A_e - P_r A_r)\text{Vel} \qquad (3)$$

where:

$P_{e,r}$ = extend and retract chamber pressure

$A_{e,r}$ = extend and retract chamber effective piston area

Vel = piston velocity

$A_{e,r}$ = extend chamber EPA 1.155E-3 m^2 & retract chamber EPA 1.056E-3 m^2 [92]

2.3 Results

FIGURE 14 *GEN 3.0 PPAFO (LINEAR ACTUATOR DESIGN)*

A compact high torque actuation system (Figure 14) for the PPAFO was designed. For physical properties comparison, the Gen 3.0 design had a 45.1% reduction in lateral profile and a 166.7% torque output increase (Table 3). While the width of the design remain similar, the overall height and weight of the design had 215% and 21.4% increases, respectively. The maximum chamber volume of Gen 3.0 increased by 67.6%.

*Table 3 Physical characteristics comparison between Gen 2.0 PPAFO and Gen 3.0 PPAFO design. *[93].*

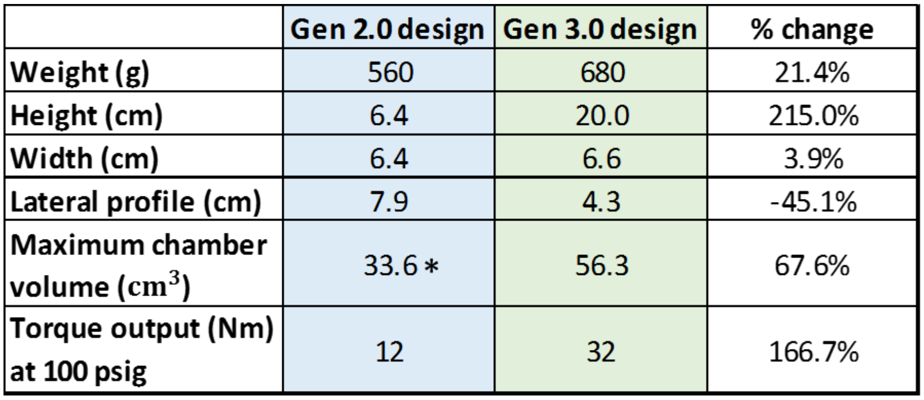

	Gen 2.0 design	Gen 3.0 design	% change
Weight (g)	560	680	21.4%
Height (cm)	6.4	20.0	215.0%
Width (cm)	6.4	6.6	3.9%
Lateral profile (cm)	7.9	4.3	-45.1%
Maximum chamber volume (cm^3)	33.6 *	56.3	67.6%
Torque output (Nm) at 100 psig	12	32	166.7%

For the power output comparison, the Gen 3.0 PPAFO was capable of generating an equal amount of power at a much lower operating pressure. The peak power output of the Gen 3.0 PPAFO at 38 psig was close to Gen 2.0 PPAFO at 100 psig (50 W), while Gen 3.0's power more than doubled when operated at 100 psig (110 W) (Figure 15 & Table 4).

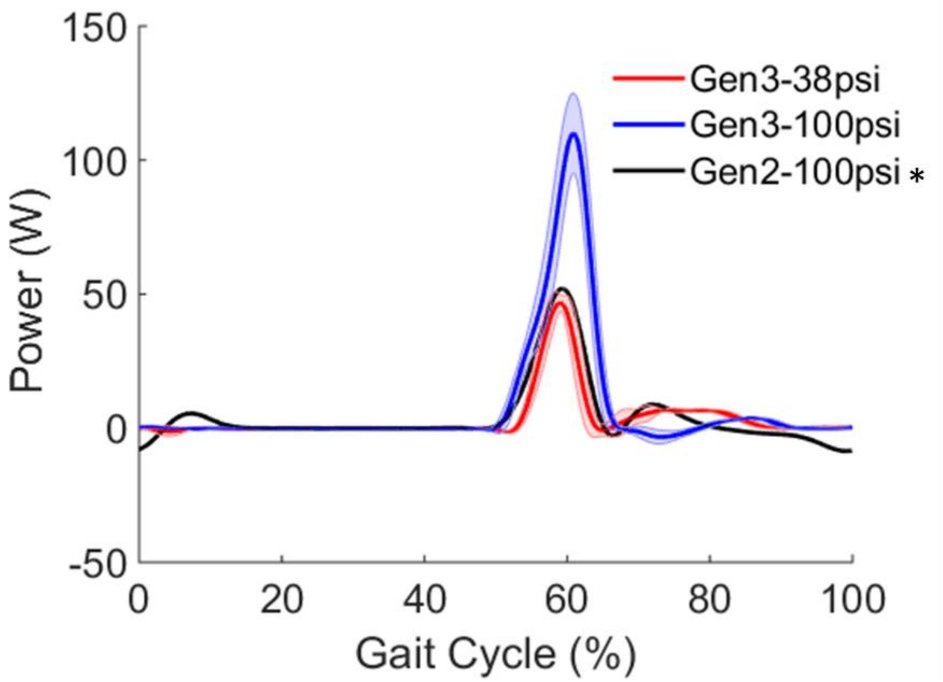

FIGURE 15 AVERAGE *POWER OUTPUT OF GEN 2.0 & GEN 3.0 PPAFOS. SHADED AREAS REPRESENT THE STANDARD DEVIATIONS OF POWER OUTPUT OF THREE TRIALS PER GEN 3.0 TEST CONDITION. *[18]*

For the gas consumption comparison, the Gen 3.0 PPAFO had 0.021 min/g and 0.048 min/g increases in normalized runtime, compared to Gen 2.0, for test bench emulation and treadmill walking while under the same torque output condition (12 Nm target). When operating under the same pressure (100 psig) as the Gen 2.0 PPAFO, the Gen 3.0 PPAFO's normalized runtime was reduced by 0.012 min/g.

Table 4 Mean and standard deviation of Run time, Normalized Runtime, and Mass consumption per step comparison of all experimental trials. *[78],**[18]

	PPAFO	Operating Pressure (psig)	Torque Output (Nm)	Peak Power (W)	Run Time (min)	Normalized Runtime (min/g)	Mean Mass Consumed per Step (g/step)
Test Bench Emulation	Gen 2	100	12	50 **	10.2±0.3	0.049±0.003	0.335±0.002
	Gen 3	38	12	50	17.0±2.7	0.070±0.004	0.238±0.012
	Gen 3	100	32	110	9.0±0.3	0.037±0.003	0.444±0.036
Treadmill Walking	Gen 2 *	100	12	50 **	13.7±2.6	0.059±0.006	0.284±0.303
	Gen 3	38	12	50	22.7±1.9	0.107±0.005	0.165±0.012

2.4 Discussion

In this chapter, we presented the design and evaluation of a compact, higher torque actuation system for PPAFO. The previous design (Gen 2.0 PPAFO) served as a testbed platform for investigating the effect of a powered orthosis on able-bodied and impaired gait [78-80]. Early studies recorded improved gait functionality, however that design’s peak plantarflexor torque was only 12 Nm for 100 psig input pressure. In addition, the off-the-shelf rotatory actuator had a large and undesirable lateral profile. The main objective of the new system design was to increase the maximum torque output, while also minimizing system volume and weight, so that further studies can be conducted through a range of torque settings.

The new actuation system consisted of two linear actuators, a customized compound gear train and a gear housing. The compound gear train was used to convert the actuators’ linear motion to rotatory motion, and the gear housing was used to contain the gear train. The evaluation of the Gen 3.0 PPAFO was conducted by comparing its physical properties and performances with the Gen 2.0 design.

For physical properties evaluation, the two systems’ dimensions, overall weights and maximum torque outputs were compared (Table 3). The Gen 3.0 design had a 45.1% reduction in lateral profile. A decreased lateral profile will enable the possibility of fitting the system within a pair of slacks, as well as reduced the risk of interfering with the surrounding environment. The overall height of the design, though at a 215% increase, reduced the added device weight's radius of gyration relative to the medial-lateral axis of rotation of the knee joint by shifting the center of mass of the actuation system more proximal along the shank. This could be beneficial since the more moment of inertia added to the distal joint, the more energy is needed to swing the limb during gait [21]. The peak torque that the Gen 3.0 system could generate at 100 psig was 32 Nm, which was 166.7% higher than previous design. Although the overall weight of the new system had a 20% increase compared with Gen 2.0, the new design was capable of providing the same amount of torque and power (Figure 15) at a lower operating pressure and a longer normalized runtime (Table 4).

For the performance evaluation, the systems' power generation, normalized runtime, as well as CO_2 mass consumption per step were compared. The system was capable of generating an equal amount of power as the Gen 2.0 system at a much lower operating pressure. The peak power output of Gen 3.0 PPAFO at 38 psig was close to Gen 2.0 PPAFO at 100 psig (50 W). Moreover, the average peak power of Gen 3.0 PPAFO when operating under 100 psig was 110 W (Figure 15, Table 4). This amount was 120% more than what Gen 2.0 PPAFO could generate. The increased the maximum power and torque output of the new design extended the range of power and torque settings. These extended ranges would allow us to understand how torque and power impacts gait functions.

For the gas consumption (longevity) study, the Gen 3.0 PPAFO had 0.021 min/g and 0.048 min/g increases in normalized runtime for test bench emulation and treadmill walking while under the same torque output condition (12 Nm target, Table 4). The normalized runtime of Gen 3.0 PPAFO for both bench test and treadmill walking were longer than the Gen 2.0 PPAFO. Moreover, the mass consumed per step for Gen 3.0 PPAFO was also lower than Gen 2.0 PPAFO. These results suggested that the new system, when running under same torque and power setting, offered better longevity. The operating pressure was increased to compare the runtime of Gen 3.0 and Gen 2.0 under the same operating pressure of 100 psig (Table 4). This comparison was conducted in the test bench condition only because the high torque output of the Gen 3.0 design could result in injury to the wearer if not properly controlled. Results suggested that when operating under 100 psig, the Gen 3.0 PPAFO's normalized runtime was 0.012 min/g shorter than that of the Gen 2.0 PPAFO.

To conclude, the new system achieved a higher torque output, while meeting range of motion requirements and reducing the actuation system's lateral profile. The maximum torque that Gen 3.0 system could generate was 32 Nm and the maximum power was 110 W. In addition, the system's normalized run time was reduced when operating under a torque setting equivalent to the Gen 2.0 design's normal operating torque (12 Nm). This result was expected because the pneumatic cylinders consumed more power fuel per step when running at 100 psig.

Although results from the new design are encouraging, a few limitations must be addressed. Firstly, the weight of the current system is slightly heavier than the Gen 2.0 design (21.4% increase). The weight could be further reduced using lightweight actuators (fiberglass cylinders). Use of fiberglass cylinders could possibly bring the weight of the linear pneumatic system below that of the rotary actuator system. Secondly, a couple of the moving compounds (yoke and actuators' pistons) were still exposed. Because the moving components could possibly injure the wearer, further modification might be needed to fully contain these components. Lastly, as the system was capable of generating high torque, the current binary control strategy becomes problematic. Inaccurate actuation timing of plantarflexion could cause limb discomfort for a low torque system [94]; however, a high torque system could further amplify this error and possibly injure the wearer. Thus, an advanced control strategy is required. Other alternative solutions may include proportional control valves or novel piezoelectric valves. While, most commercially available proportional valves are heavy, piezoelectric valves are limited to a low maximum operating pressure and low flow rate [95, 96]. Though the flow rate could be overcome by using multiple piezoelectric valves in parallel, the low operating pressure could still be a problem. Further investigation on identifying proper control strategies is needed.

2.5 Conclusion

The design and evaluation of a compact and high torque actuation system for a new PPAFO design (Gen 3.0) was presented. The actuation system utilized two dual-action linear actuators and a customized gear train to provide plantarflexion and dorsiflexion actuation to the ankle joint. The system, compared with a previous generation design (Gen 2.0), was capable of generating higher torque (166.7% increase) and power (120% increase) output while delivering a thinner lateral profile (45.1% decrease). The runtime of the Gen 3.0 PPAFO under same power torque output condition (12 Nm) was longer than the Gen 2.0 design (42.9% and 81.4% increases for test bench emulation and treadmill walking). The runtime at maximum torque and power conditions was shorter than that of Gen 2.0 design (24.4% decrease). This result was expected because the pneumatic cylinders consumed more fuel per step when running at 100 psig. Although the overall weight of the new system had a 21.4% increase compared with Gen 2.0, the Gen 3.0 design could generate substantially more torque which will enable future testing of the system at various torque settings.

Chapter 3:

MINIMUM SENSOR CONFIGURATION FOR GAIT EVENT DETECTION FOR A PORTABLE POWERED ANKLE-FOOT ORTHOSIS

Abstract

Receiving gait information from external sensors is essential for successfully controlling a powered ankle-foot orthosis (AFO). Many wearable sensors and gait detection algorithms have been investigated for gait event detection. However, with the increasing number of sensors and algorithms, gait estimation systems' complexities have increased. To our knowledge, there has been no systematic study on identifying the simplest cost-effective and robust sensor configuration for a powered AFO. In the present study, we investigated the minimum sensor configuration for detecting gait events. A total of five sensors were selected (two force sensitive sensors, one ankle angle sensor, and two inertial measurement units (IMU)). The performances of selected sensor configurations were quantified and compared through state-based and event-based approaches in terms of gait state estimation and gait event detection timing, respectively. Gait data were collected from five subjects while walking on a treadmill wearing a powered AFO. Results indicated that, while the single IMU configurations (on the shank or foot) both outperformed all other configurations (mean state estimation error: < 2% gait cycle; mean event detection timing error: < 23ms), the shank IMU was able to detect more gait events than the foot IMU. Since more detectable events could improve system robustness (i.e., adjusting to variable speeds) by updating estimation more frequently, a single shank IMU configuration was recommended for powered AFO applications.

3.1. Introduction

A powered ankle-foot orthosis (AFO) is a special class of gait assistive device that employs an actuation system to enhance movement of ankle articulation. Over the past decade, research on powered orthoses have expanded considerably [12, 25, 75]. The functions of lower limb powered orthoses range from power enhancement to gait function restoration [6, 13, 21, 23, 41, 57, 97]. For these different functionalities, the mechanical structures, actuators and interfaces vary. However, when it comes to sensing and control processes, they usually follow a series of common steps [6, 13, 21, 23, 41, 57, 71]: (1) detect the lower limb kinematics and kinetics, (2) identify key gait events, and (3) apply control to meet the functional objective determined by the gait events. Therefore, proper tracking of gait (steps 1 and 2) is essential for successfully controlling a powered AFO.

Gait is a cyclic task characterized by repetitive events [71]. A normal gait cycle generally begins from initial heel strike, 0% gait cycle (GC), and ends at the next heel strike of the same foot, 100% GC. A normal walking gait cycle can be divided into three functional tasks (weight acceptance, single-limb support and limb advancement) [1] and eight different sub-phases (initial contact (IC), loading response (LR), mid stance (MSt), terminal stance (TSt), pre-swing (PSw), initial swing (ISw), mid-swing (MSw), and terminal swing (TSw)) [2] (Figure 16). Efficient segmentation of the gait cycle into these gait sub-phases is a critical component of gait estimation and can be achieved through the detection of gait events. Ten possible gait events during a gait cycle are presented (Figure 16).

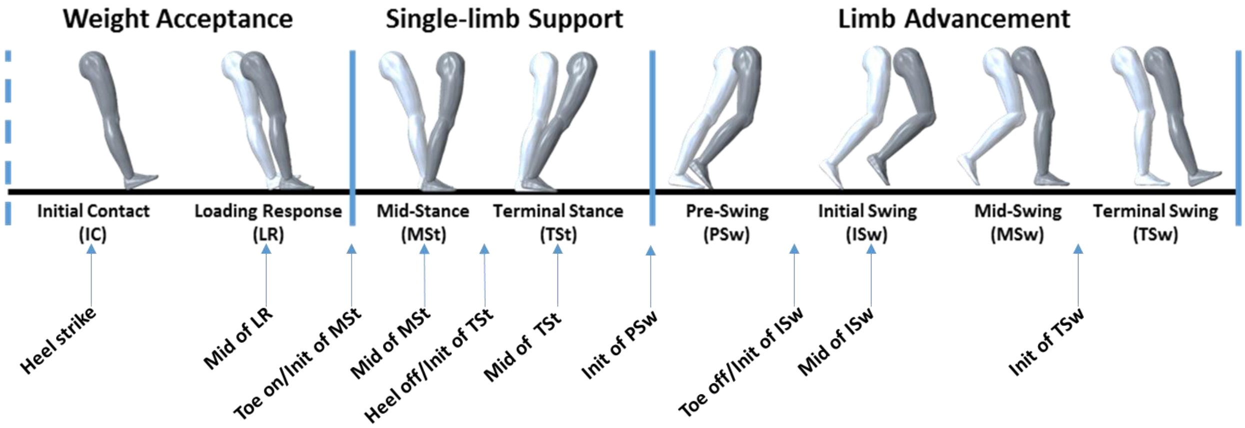

FIGURE 16 DIFFERENT FUNCTIONAL TASKS, SUB-PHASES, AND POSSIBLE GAIT EVENTS OF A GAIT CYCLE (FIGURE CREATED USING HUMAN MODEL DOWNLOADED FROM [3])

The detection of gait events has been of interest in several fields of studies. Its applications range from classification of daily activities such as stair climbing [59, 74], distinguishing abnormal gait behavior [98, 99], to controlling robotic devices such as powered prostheses or orthoses [6, 13, 21, 23, 41, 57, 97]. According to the literature, common wearable sensors used for gait event detection are: footswitches [6, 35-37] (e.g. pressure insoles, force sensitive resistors (FSR)), joint angle measurement sensors [38, 39, 41] (potentiometer, goniometer and Hall Effect sensor), electromyography (EMG) sensors [31, 100, 101], and other inertial sensors such as accelerometers, gyroscopes and their combination which is known as an inertial measurement unit (IMU) [21, 22, 59, 102]. With a proper developed gait event detection algorithm, one can detect gait events within each gait cycle.

In both clinical and powered orthotic applications, most existing gait event detection methods utilized detection of local maxima, minima and/or crossing pre-defined threshold values [6, 23, 31, 36, 44, 49, 74]. Advanced methods such as curve-alignment, pattern fitting and model based identification have also been proposed [13, 37, 38, 41, 46, 71]. However, some of these advanced algorithms either cannot achieve satisfactory control for AFOs due to susceptibility to chattering and delays in the classification process [13, 71] or a model of the system was necessary to identify gait events [38].

In our group, two types of gait detection approaches have been used for controlling a portable powered ankle-foot orthosis (PPAFO). The first approach, event-based approach, provided torque assistance simply based on the detection of gait events of interest (the events that can be used to control powered AFO directly) [6]. Shorter et al. mentioned an event-based Direct Event (DE) controller that used heel and toe FSR “on” and “off” states to control the actuation of the PPAFO [6]. FSR “on” and “off” states were defined when sensor magnitudes exceeded or fell below a set of thresholds, respectively. Dorsiflexor torque was applied when the heel FSR was “on” and the toe FSR was “off”, and plantarflexor torque was applied when the heel FSR was “off” and the toe FSR was “on”. Similar approaches have been seen in other applications such as the use of Functional Electrical Stimulation (FES) systems for correction of foot drop, which often require detection of the heel strike (HS) and toe off (TO) events to stimulate the paralyzed muscles [74]. For the event-based approach, accurate event detection timing is crucial. This is because the control of the device is depended on the detection of certain gait events of interest. It was observed that for some users with impaired gait function who did not follow typical heel-toe gait, the event-based approach did not provide appropriate control of the PPAFO since the sensors could not detect all DE gait events of interest [71]. Therefore, the following state-based approach was developed.

The second approach, state-based approach, characterized the gait cycle as a set of gait states. A full gait cycle was divided into 101 states (0-100) to represent 0% to 100% GC [41, 71]. The gait state was determined by sensor measurements and then used to identify the gait events of interests in %GC to provide control to the PPAFO [41, 71]. Li et al. [71] used a state-based Fractional Time (FT) estimator that depended only on the HS event. The gait state was then estimated with the assumption that subsequent gait states increased linearly within the time between consecutive ipsilateral HS events. Once the estimated gait state reached a set of predefined %GC, the PPAFO applied appropriate torque assistance (e.g., dorsiflexion: 0-7 %GC and 62-100 %GC, plantarflexion: 48-62 %GC, no pressurized state: 7-48 %GC). This controller's robustness, however, was limited when gait speed changed [41]. Since it could only detect the start and end of a gait cycle via the HS event, the FT controller was not able to update gait states within a gait cycle. To increase the system's robustness, Islam et al. [41] proposed two new state-based estimators (Modified Fractional Time (MFT) and Artificial Neural Network (ANN)), which utilized both heel and toe FSRs and an additional ankle angle sensor (Hall Effect sensor) to estimate the gait state. MFT was able to detect events and update gait state estimation up to eight times within a single gait cycle, and ANN was capable of estimating gait states continuously across the gait cycle by using a moving window of six previous sets of data points. Both state-based MFT and ANN estimators showed significant improvements when compared with the FT estimator; however they were also computationally expensive.

Advanced approaches and multi-sensor configurations showed improvements in gait event detection in terms of accuracy and number of detectable events [37, 38, 41]. However, with the increasing number of sensors introduced to the systems, system complexity could also increase due to complex data collection protocols and computationally expensive algorithms [74]. Applying multiple sensors and complex algorithms does not necessarily indicate the best solution, and to our knowledge, the most cost-effective sensor configuration for robust gait event estimation is still unknown. Thus, we were interested in investigating the minimum number of sensors needed for gait event estimation.

In this study, we investigated the minimum sensor configuration needed for gait event estimation for a powered AFO (Figure 17) [103]. A total of five sensors were considered (two force sensitive sensors, one ankle angle sensor, and two inertial measurement units (IMUs)). Since the previous state-based algorithms developed in our lab used at most three sensors, only single and double sensors configurations were evaluated in this study. Selected sensor configuration performances were quantified and compared through event-based and state-based approaches in terms of gait event detection timing and gait state estimation, respectively. Gait events were first detected through the use of a combination of local maxima, minima and threshold-crossing methods. Then the detected events were used to perform gait state estimation. Gait data were collected from five subjects while walking on an instrumented treadmill wearing a powered AFO on their right foot.

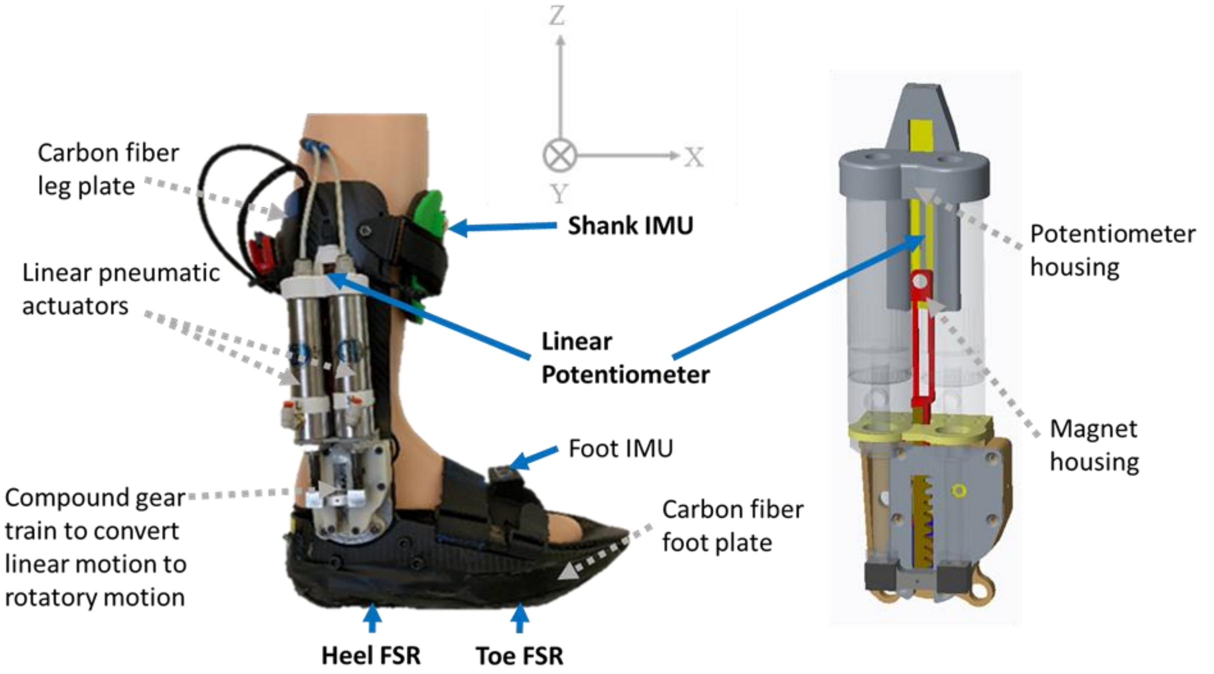

Figure 17 PPAFO hardware overview. The shank and foot plate are connected by a pneumatic actuation system (gray), which can provide dorsi- or plantarflexor torque. Five selected sensors and their placements for gait event detection are highlighted with blue arrows.

3.2 Method

This section is divided into six parts. The first part describes the sensors and their placements. The second part explains gait event detection methods and presents the detectable gait events for each sensor. With the knowledge of each sensor's detectable events, the third part lists the selected sensor configurations compared in this study. The fourth part introduces the data collection procedure. The fifth part describes the state estimation process using collected data. Upon the completion of gait event detection and state estimation, the last part introduces the performance evaluation methods.

3.2.1 Sensor description

A total of five sensors were compared in this study (Figure 17). Two force sensitive sensors (FSRs) were used for detecting foot contact under the heel and ball of the foot (FSR-square, SEN-09376 ROHS, SparkFun Electronics, Niwot, Colorado, USA). The FSRs were embedded between the shoe foam sole and rubber tread. Footswitches are low cost and reliable for the detection of the foot contacting the floor [47]. However, the number of detectable events are limited, and a FSR's performance is highly depending on its placement [47, 104, 105]. In addition, the wire connections embedded in the shoe foam sole are exposed to repetitive load which decreases its service life [47].

A linear magnetic potentiometer (MagnetoPot; Spectra Symbol; West Valley City, UT) was attached to the linear pneumatic actuators (Figure 2). Due to the actuators' linear motion being directly translated to ankle joint through the gear train, the potentiometer measurement could be converted to ankle angle measurement (Appendix E). The validation of the angle measurement was performed by comparing the calculated joint angles with the joint angles measured with a goniometer. The discrepancies were assessed by the Pearson correlation coefficient. The two sets of measurements had a correlation coefficient of 0.99. The linear potentiometer output was directly proportional to the ankle angle. However, the potentiometer also requires a proper placement. There are two parts in this linear magnetic potentiometer, a stationary magnetic sensor and a moving magnet (Figure 17). The magnetic sensor was fixed to the outside of the linear actuators through the potentiometer housing, and a magnet was synced to the linear rack motion through the use of a magnet housing.

Two IMUs (MPU9250; InvenSense; San Jose, CA) were attached to the bony landmarks of the foot and shank segments (anterior shin at tibial strap (Figure 18.b) and dorsal surface of foot strap (Figure 18.c)) to track the kinematics of these segments. Custom housings were designed to contain the shank and foot IMUs (Figure 18.b & c). Each IMU consisted of one 3D accelerometer, one 3D gyroscope and one 3D magnetometer. The magnetometer was not used in this study due to its poor performance during indoor activities [59]. This IMU is low-cost, light weight [47], and also has a minimal profile and low power consumption [51]. Additional signal processing such as filtering might be required for certain IMU measurements [106]. In this study, each IMU was considered as one sensor.

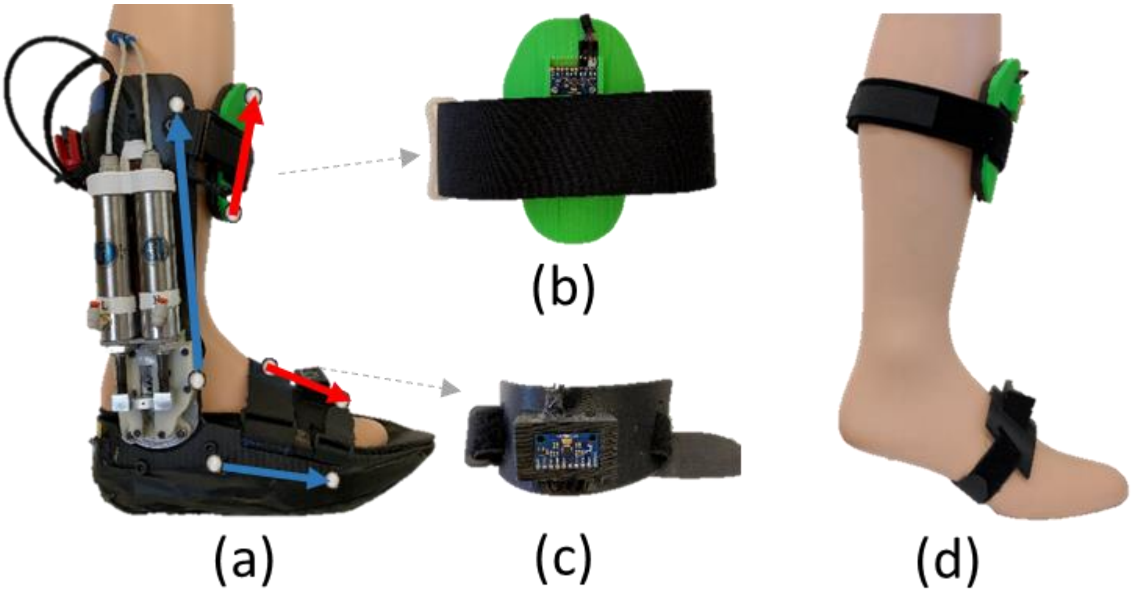

FIGURE 18 (a) MARKER PLACEMENT AND VECTOR REPRESENTATION FOR COMPARING ANGLES COMPUTED USING PPAFO SHELL (OPTION 1 BLUE) OR BODY SEGMENT (OPTION 2 RED). (b) TIBIAL STRAP AND CUSTOM SHANK IMU HOUSING (ANTERIOR SHIN). (c) FOOT STRAP AND CUSTOM FOOT IMU HOUSING (DORSAL SURFACE OF FOOT). (d) IMU STRAP-ON FEATURE WITHOUT PPAFO.

A supplemental study was conducted to find the best IMU placement because there were two options of where to place the IMU sensors when measuring segment orientation (either on the carbon fiber shells of the orthosis (shank and foot shell) or strapped directly to the shank and foot segments). We used a motion capture system (Model 460; Vicon, Oxford, UK) to capture the shell-based vectors angle and body segment-based vectors angle in sagittal plane. A total of eight markers were placed on the carbon fiber shells and the straps on the body segments with four vectors representing the orientation of the attached surfaces in sagittal plane (Figure 18.a). Shell-based vectors angle (angle between two blue vectors in sagittal plane) and body segment-based vectors angle (angle between two red vectors in sagittal plane) were then derived (Appendix F). This supplemental study found that the two angles had a correlation coefficient of 0.99. This result effectively meant that with the PPAFO securely attached to the shank-foot segments, the movement artifact between the body and PPAFO was minimal. In this study, we chose to strap the IMUs on the shank and foot segments. The strap-on feature would not only simplify the donning and doffing process, but also allowed for the possibility of collecting subject data with or without wearing the PPAFO (Figure 18.d).

3.2.2 Gait event detection methods for each individual sensor

We first used a combination of local maxima, minima and threshold-crossing methods to identify potential points within the collected data that may qualify as gait events. Ten potential events were identified (Figure 16&Table 5): (1) Heel Strike, (2) Middle of the loading response (mid of LR), (3) Toe on or Beginning of the mid-stance (init of MSt), (4) Middle of the mid-stance (mid of MSt), (5) Heel off or Beginning of the terminal stance (init of TSt), (6) Middle of the terminal stance (mid of TSt), (7) Beginning of the pre-swing (init of PSw), (8) Toe off or Beginning of the initial swing (init of ISw), (9) Middle of the initial swing (mid of ISw), and (10) Beginning of the terminal swing (init of TSw). Events 1, 3, 5, 7, 8 and 10 are the events which indicated the transition between two sub-phases. Events 2, 4, 6, and 9 are the gait events which indicated the middle of certain sub-phases.

TABLE 5. GAIT EVENTS AS DETECTED BY EACH SENSOR.

Functional tasks	Weigth Acceptance				Single-limb Support				Limb Advancement						
Sub-phases	IC		LR		MSt		TSt		PSw		ISw		MSw		TSw
Events Sensors	1. heel strike		2. mid of LR	3. toe on/init of MSt	4. mid of MSt	5. heel off/init of TSt	6. mid of TSt	7. init of PSw		8. toe off/init of Isw	9. mid of ISw			10. init of TSw	
shank IMU	×		×		×		×	×		×	×			×	
foot IMU	×		×	×				×		×	×			×	
Ankle Angle				×				×		×	×				
Heel FSR	×					×									
Toe FSR				×						×					

3.2.2.1 FSRs

Each of the FSRs embedded in the PPAFO foot piece were able to detect two events (Table 5). These events were detected when the sensor magnitudes rose above or fell below a set of predefined thresholds (Figure 19). The ***heel strike*** event indicated the start of the gait cycle and was detected when the heel sensor reading rose above the heel strike threshold (i.e., 0.3V). The beginning of the mid-stance or ***toe on*** event was defined when the toe sensor signal was in a rising edge. The ***heel off*** event was detected when the heel sensor faced a falling edge and the ***toe off*** event was detected by the falling edge of the toe sensor. These last three events were detected when sensor readings crossed the thresholds (i.e., 1.0V). This higher voltage threshold value was used for these events due to large variability in the sensor signals around the timings of these events (Figure 4).

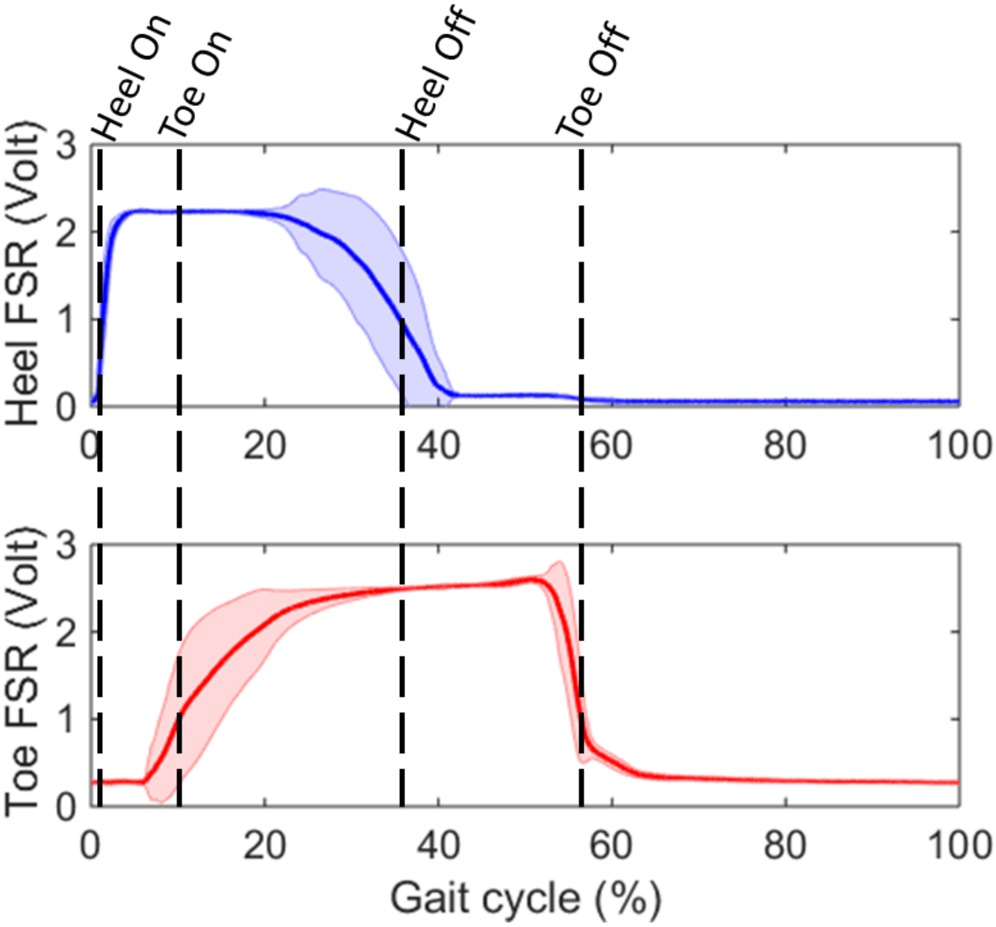

FIGURE 19 MEAN VALUES (SOLID LINE) AND STANDARD DEVIATION (SHADED AREAS) OF HEEL AND TOE FSRS MEASUREMENTS OVER ONE SUBJECT'S MULTIPLE GAIT CYCLES

3.2.2.2 Ankle angle

The ankle angle and its derivative (angular velocity) were capable of detecting four events consistently (Figure 20). ***Init of MSt*** was detected when the ankle joint started the rotation towards the dorsal direction due to the body weight shifting to the ipsilateral limb, as indicated by finding the angular velocity rising and crossing 0˚/s. ***Init of PSw*** was detected when the ankle joint reached maximum dorsiflexion between the terminal stance and pre-swing. ***Mid of ISw*** event was detected when the ankle joint reached maximum plantarflexion. One more event, ***Init of ISw***, was also defined by detecting the maximum plantarflexion-directed velocity, as noted by the minima of the angular velocity (Figure 20). The angular velocity was calculated using the difference between angle measurements divided by the sampling time (2 ms) then filtered with a 4th order Butterworth low pass filter with a cut-off frequency of 30 Hz. Cut-off frequencies within the range of 25-35 Hz have been commonly used for providing real-time sensing [36, 49, 105, 107, 108] as they removed unwanted noise while retaining gait information [105].

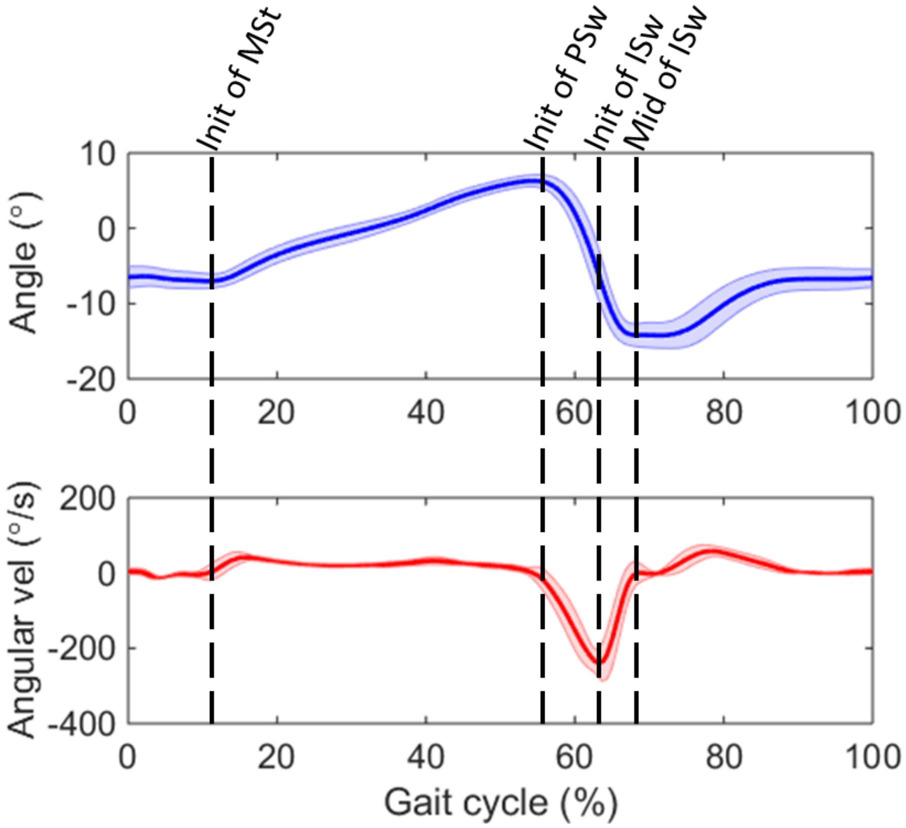

FIGURE 20 MEAN VALUES (SOLID LINE) AND STANDARD DEVIATION (SHADED AREAS) OF ANKLE ANGLE POSITION AND VELOCITY OVER ONE SUBJECT'S MULTIPLE GAIT CYCLES (POSITIVE VALUES INDICATE DORSIFLEXION ANGULAR POSITION AND VELOCITY)

3.2.2.3 Shank and foot IMU

The shank and foot IMUs were capable of detecting multiple events (Table 5). For example, looking at the shank IMU (Figure 21), since we were focusing on the sagittal plane (x-z) movement, we only examined the sagittal plane x-direction acceleration (a_x), z-direction acceleration (a_z), and y-direction gyroscope angular velocity (ω_{gyr}) from the respective accelerometers and gyroscope in the shank IMU (Figure 17 & Figure 21). The unit for acceleration was in g (standard gravity; g = 9.8 m/s^2), and the unit for angular velocity was in (˚/s). In addition to these direct measurements, z-direction jerk ($\dot{a}_z$, in g/s) and y-direction gyroscope angular acceleration (α_{gyr}, in ˚/s^2) were recorded. Both $\dot{a}_z$ and α_{gyr} were derived using the same method mentioned previously. The shank segment angular position, velocity, and acceleration were defined as positive when considered counterclockwise from the positive global X-axis (color gray in Figure 21). For shank angular velocity and acceleration, these directions are opposite to the y-direction of the gyroscope (Figure 21). Therefore, we defined $\omega_{shank} = -\omega_{gyr}$ and $\alpha_{shank} = -\alpha_{gyr}$.

Because the segment angular position orientation could also be used to indicate certain gait events (i.e., shank segment angle was 90˚ to the ground at ***Mid of MSt***), we implemented a Kalman filter to estimate the shank IMU orientation (θ_{kalman}) using combined data from the accelerometers and gyroscope. This value was then converted to the shank segment angular position orientation ($\theta_{shank} = 90^{\circ} - \theta_{kalman}$) [53, 64, 109] (Appendix G). The IMU orientation was first calculated through the gyroscope (θ_{gyr}) by integrating the gyroscope reading ω_{gyr}. The integration error (drift over time) was then corrected through the Kalman filter using the angle calculated from accelerometer readings a_x and a_z using trigonometry ($e.g.,\ \theta_{acc} = \tan^{-1}\left(-\frac{a_x}{a_z}\right)$, Figure 21). This method for computing θ_{shank} was preferred over integrating ω_{shank}, as derived from only the gyroscope, because integration method caused errors (i.e., signal noise) to accumulate and caused the calculated values to ‘drift’ from the true value.

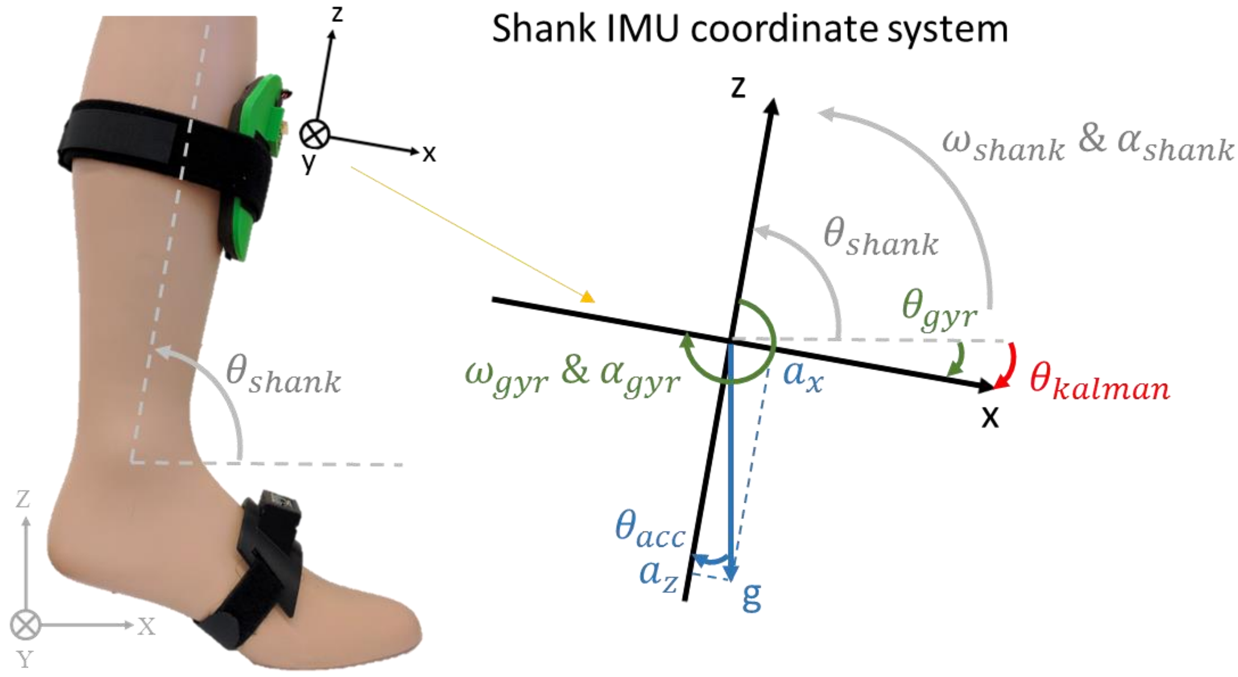

FIGURE 21 OUTLINE OF SHANK ORIENTATION ESTIMATION IN GLOBAL COORDINATE SYSTEM (GRAY) THROUGH THE SHANK IMU'S KALMAN FILTER RESULT (RED) DERIVED FROM THE COMBINATION OF BOTH GYROSCOPE (GREEN) AND ACCELEROMETER (BLUE) DERIVED ANGLE MEASUREMENTS

The following gait events were detected from the shank IMU signals. ***Heel strike*** was detected as when $\dot{a}_z$ or α_{shank} reached a certain threshold (i.e., 50 g/s or -10000˚/s^2). ***Mid of LR*** was defined as when the jerk's magnitude fell below a certain threshold (i.e., $\dot{a}_z < 50$ g/s). ***Mid of MSt*** was defined when the ipsilateral shank reached a vertical position, and ***mid of TSt*** was defined as when ipsilateral shank orientation (θ_{shank}) approached 80˚ (i.e., 10˚ dorsiflexion). ***Init of PSw*** was defined when the shank angular velocity decreased and reached a certain threshold (i.e., $\omega_{shank} = -100^\circ/\mathrm{s}$). ***Toe off*** was defined when shank angular velocity reached a local minima. ***Mid of ISw*** was detected when ω_{shank} crossed zero angular velocity. From a pilot study, we found that ω_{shank} reached a local maxima, and θ_{shank} = 90˚ (vertical to the ground) during the beginning of the terminal swing phase (***init of TSw***) (Figure 22). During swing, the hip flexes and knee extends which combined created a peak positive shank angular velocity [2, 49, 110]. Therefore we used the local maxima of the shank angular velocity (ω_{shank}) as an indicator to reset the estimation process and started to look for the heel strike by monitoring the z-direction jerk ($\dot{a}_z$) and shank angular acceleration (α_{shank}).

The gait events detected from the foot IMU were the same as the shank IMU, except for three events during the stance phase (foot flat on the ground). Due to a lack of the variance within foot IMU measurements during stance, the foot IMU could not detect ***mid of MSt***, ***init of TSt***, and ***mid of TSt*** during mid stance (Figure 23).

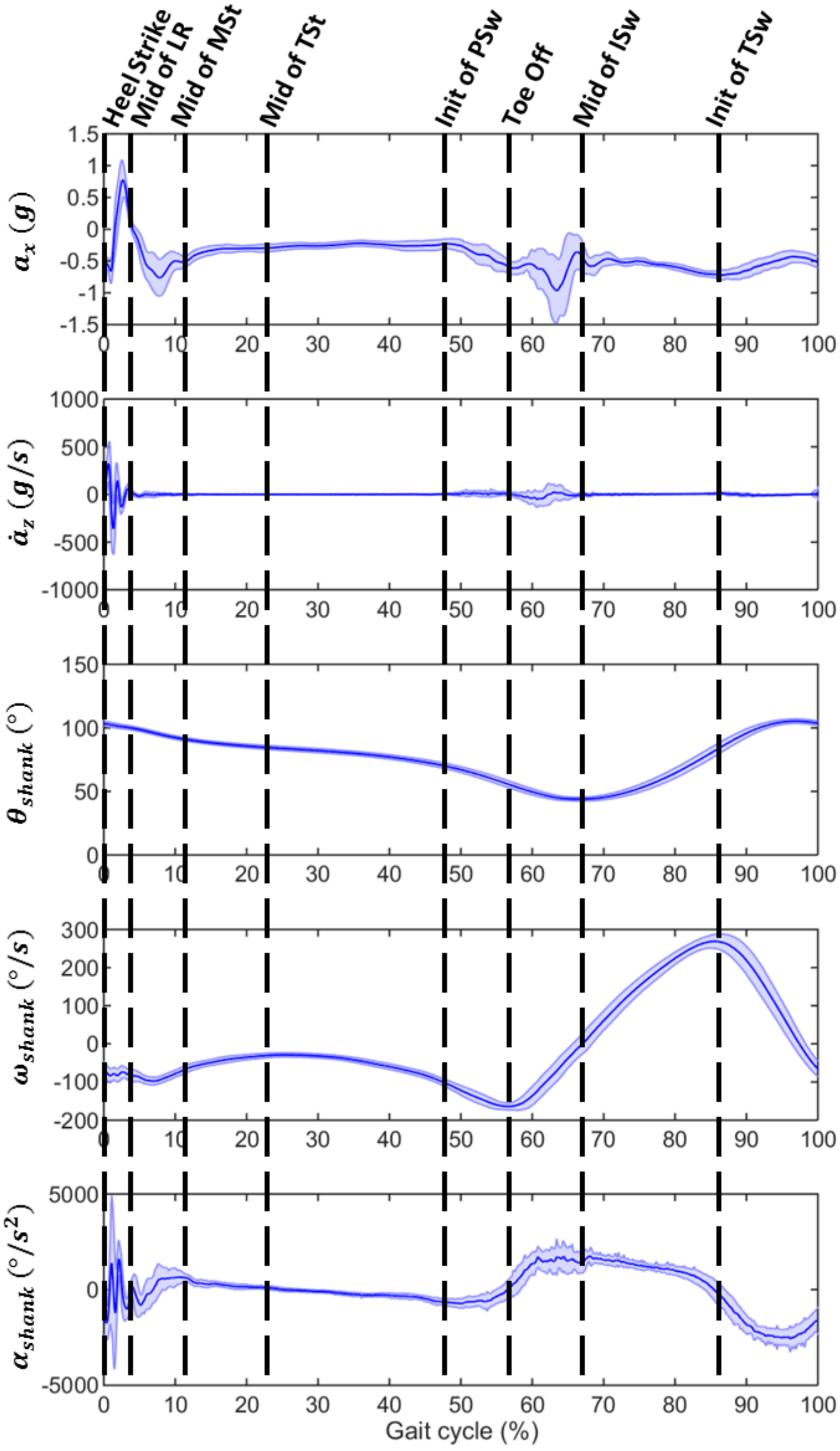

FIGURE 22 MEAN VALUES (SOLID LINE) AND STANDARD DEVIATION (SHADED AREAS) OF SHANK IMU MEASUREMENTS OVER ONE SUBJECT'S MULTIPLE GAIT CYCLES

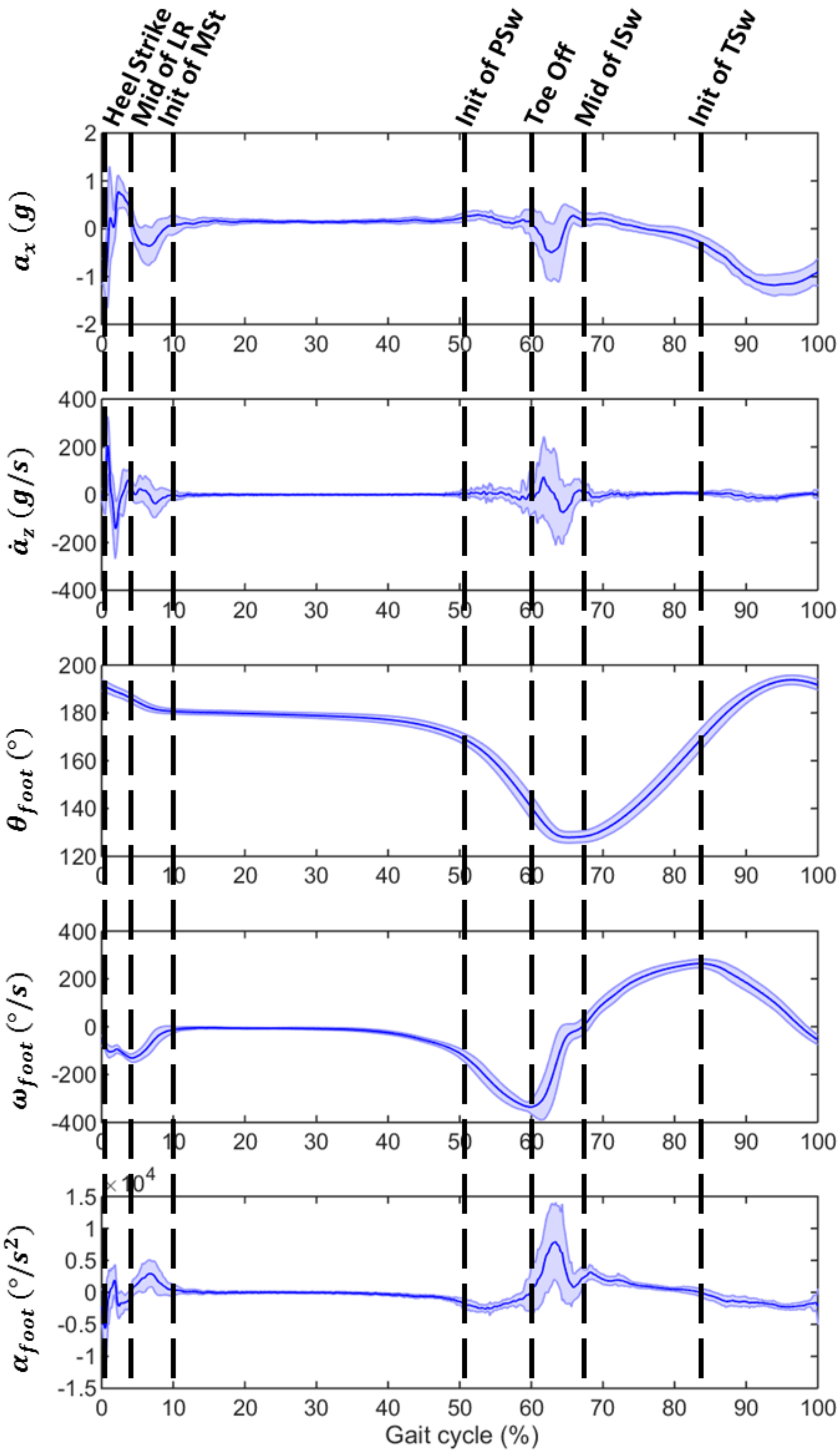

FIGURE 23 MEAN VALUES (SOLID LINE) AND STANDARD DEVIATION (SHADED AREAS) OF FOOT IMU MEASUREMENTS OVER ONE SUBJECT'S MULTIPLE GAIT CYCLES

3.2.3 Identify potential sensor configurations

After determining which gait events could be detected for a given sensor, a total of nine sensor configurations were chosen to be evaluated (Table 6). These configurations were either using a single sensor (blue cells) or dual sensor configurations (green). Sensor configurations that could not detect heel strike, such as a single toe sensor configuration, were ignored (×, grey). Dual sensor configurations, such as ankle angle and IMU, were also ignored since the events detected by ankle angle sensor were redundant to the IMU events (***init of MSt***, ***init of PSw***, ***init of ISw***, and ***mid of ISw***; Table 5) (•, grey).

TABLE 6 SENSOR CONFIGURATIONS CONSIDERED FOR COMPARISON (ROW ELEMENT REPRESENTS FIRST SENSOR AND COLUMN REPRESENTS THE SECOND SENSOR)

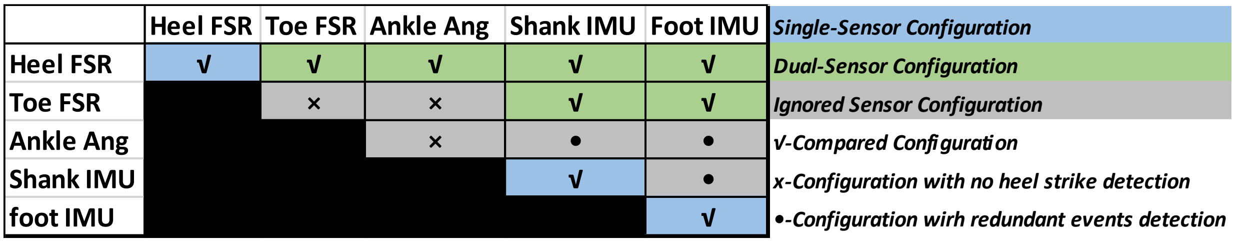

	Heel FSR	Toe FSR	Ankle Ang	Shank IMU	Foot IMU
Heel FSR	√	√	√	√	√
Toe FSR		×	×	√	√
Ankle Ang			×	•	•
Shank IMU				√	•
foot IMU					√

Single-Sensor Configuration
Dual-Sensor Configuration
Ignored Sensor Configuration
√-Compared Configuration
x-Configuration with no heel strike detection
•-Configuration wirh redundant events detection

3.2.4 Data Collection

3.2.4.1 Subjects

Five adult male subjects participated in this study. All subjects were healthy (age 24.2 ± 5.1 years, height 173.8 ± 8.9 cm, weight 75.9 ± 9.5 kg) and did not have any neurological, gait, or postural disorders. All procedures were approved by the institutional review boards of the University of Illinois, and all participants gave informed consent.

3.2.4.2 Experimental setup

Subjects walked with the PPAFO on an instrumented split-belt treadmill (Bertec, Columbus, OH) at their self-selected comfortable walking speed. The average gait period of all five subjects was

1.3s. The PPAFO was worn on the right limb. The subject's own shoe (running/walking) was worn on the left limb. A total of five one-minute trials of data per subject were collected. Four reflective markers were attached to the PPAFO shell (Figure 18, option 1). Only one option was used due to both option 1 and 2 are essentially outputting same patterns (correlation coefficient of 0.99). Kinematic data were collected using a motion capture system with a sampling rate set at 100 Hz (Model 460; Vicon, Oxford, U.K.). Kinetic data (ground reaction forces, GRFs) were also collected an instrumented treadmill (Bertec, Columbus, OH) at a sampling rate of 1000 Hz.

3.2.5 State Estimation Procedure

3.2.5.1 Identifying true gait state

The "true" gait state was considered as a gold standard to describe gait and was derived via kinematic and kinetic data collected following the method described in [41, 71]. We used a total of eight signals to define the "true" gait state (ankle angle and shank angle determined from the motion capture data, right and left vertical ground reaction forces (GRFs) from the treadmill, and their derivatives). An eight dimensional (8-D) vector $\boldsymbol{p}(t)$ was used to describe time t's position in a gait cycle. Each gait cycle was divided into 101 states (from 0% to 100% GC). A linearly weighted regression model $\overline{\boldsymbol{p}}$, with the dimension of 8×101, was then built using the $\boldsymbol{p}(t)$ data sets across all gait cycles (60s × 5 trials). Upon the completion of building the model matrix $\overline{\boldsymbol{p}}$, at any time stamp t, the "true" state $\lambda(t)$ was defined by comparing the vector $\boldsymbol{p}(t)$ to the regression model $\overline{\boldsymbol{p}}(\lambda^*)$ where λ^* was the gait state. The state λ at time t was defined as

$$\lambda(t) = \underset{\lambda^* \in [0,100]}{\arg min} \|\boldsymbol{p}(t) - \overline{\boldsymbol{p}}(\lambda^*)\|_2 \qquad (4)$$

3.2.5.2 Training procedure for each sensor configuration

All sensor configurations required a preliminary training process to fit the uniqueness of each subject's gait pattern, similar to that used in [41]. The first trial of each subject's walking data was used to serve this purpose. We used the methods described in section 2.2 to identify gait events from the training data and the methods described in section 2.5.1 to identify "true" gait state. During subject-specific training of the estimator, we saved the corresponding state value (i.e., % GC) for each event. While gait patterns varied among the subjects, the state value of each event was relatively consistent between subjects. Therefore, we defined the state value of each captured event as the mean of the "true" percentage gait cycles of each event within the training data. These state values were then saved in a vector for state estimation use (L_e, where e is from 1 to the total number of events detected from each sensor configuration).

3.2.5.3 Gait state estimation

Upon the completion of the training procedure, the remaining four trials were used as testing trials to perform gait state estimation following the Fractional Time (FT) and Modified Fractional Time (MFT) methods described in [41, 71]. During each gait cycle, the saved values of $\boldsymbol{L_e}$ were used to update the estimated state $\hat{\lambda}$. We assumed that the gait state increased linearly between two detectable events according to the average period of the gait cycle. Note that the state of the last detected event L_{LE} is a single scalar value within $\boldsymbol{L_e}$. Therefore, for current time t, the estimated state will be calculated by following equation.

$$\hat{\lambda} = L_{LE} + 100\frac{t-t_{LE}}{T(t)} \qquad (5)$$

With

$$T(t) = 0.8T(t-\Delta t) + 0.2T_{current} \qquad (6)$$

Where T was the average period of the gait cycle and was updated every time a new event was being detected. $T_{current}$ was the time between two consecutive occurrences of event L_{LE}.

t and t_{LE} each represented the time for the current detected event and the time for the last detected event, respectively. The number 0.8 and 0.2 each indicated the weight ratio of T and $T_{current}$. The higher the weight ratio of $T_{current}$, the faster that the estimator adjusts to a changing gait behavior.

3.2.6 Performance evaluation

The performances of selected sensor configurations were quantified and compared through event-based and state-based approaches in terms of gait event detection timing and gait state estimation, respectively. The mean absolute error (MAE) was used to quantify each sensor configuration performance. The MAE was defined by taking the average of the absolute values of differences between the estimated values $\hat{x}$ from the sensors and "true" values x.

$$MAE = \underset{i \in [0,n]}{\text{average}} |\hat{x}(i) - x(i)| \qquad (7)$$

Where n represented the total number of data points.

1) *Gait event detection timing*

For the gait event detection timing comparison, only heel strike (HS) and toe off (TO) detection timings were compared because their "true" timings t were identifiable using the GRF data from the treadmill. The HS and TO events marked the start of stance and swing phase, respectively. The "true" timings of the HS and TO events were identified as when the vertical GRF exceed or fell below 10N. Since each sensor configuration's HS and TO detection was achieved through one or two of the five sensors, we were essentially comparing the event detection timing of each individual sensor. Therefore, the estimated event detection timing $\hat{t}$ was identified from the shank IMU, foot IMU, heel FSR, toe FSR and ankle angle sensor (Table 5). The MAE_{event} between the each sensor's event detection timing $\hat{t}$ and the "true" event timing t was calculated. In this case, n in equation 4 represented the total number of steps.

2) *Gait state estimation*

For the gait state estimation evaluation, the MAE_{state} between each sensor configuration's estimated gait state $\hat{\lambda}$ and the "true" gait state λ was calculated. In this case, n in equation 4 represented the last 4 minutes of testing data (n=4min×60s/min×500Hz/s, where 500Hz is the sampling frequency). In addition to the sensor configurations presented in section 2.3, we also included a previously used the single heel FSR sensor based state estimator, the FT estimator [71], to represent the earliest level of state estimation performance. The FT state estimator used the same method presented in section 2.4.3 except that it relied on the detection of heel strike event only.

3.3 Results

For the gait event detection timing comparison, five sensors' HS and TO events event detection timing error were compared (Table 7). The MAE_{event} for both HS and TO events of the single IMUs were lower than that of the heel, toe FSR as well as ankle angle sensor.

TABLE 7 MEAN ABSOLUTE ERROR OF GAIT EVENT DETECTION TIMING FOR SELECTED SENSOR CONFIGURATIONS

MAE_{event} **(ms)**	***HS***	***TO***
Shank IMU	8.9 ± 10.9	22.8 ± 27.4
Foot IMU	8.4 ± 9.4	13.6 ± 15.9
Ankle Ang	N/A	53.7 ± 15.7
Heel FSR	23.9 ± 11.2	N/A
Toe FSR	N/A	33 ± 20.8

For gait state estimation, all sensor configurations had MAE_{state} less than 3.5 %GC. In general, configurations that included an IMU had better performance than non-IMU configurations (Figure 24). Among all the IMU configurations, the single IMU configurations (shank or foot IMU only) had the best performances, reducing the MAE_{state} by up to 44% when compared to the FT state estimator. Among all the non-IMU configurations, the heel-toe FSR configuration showed relatively better performance.

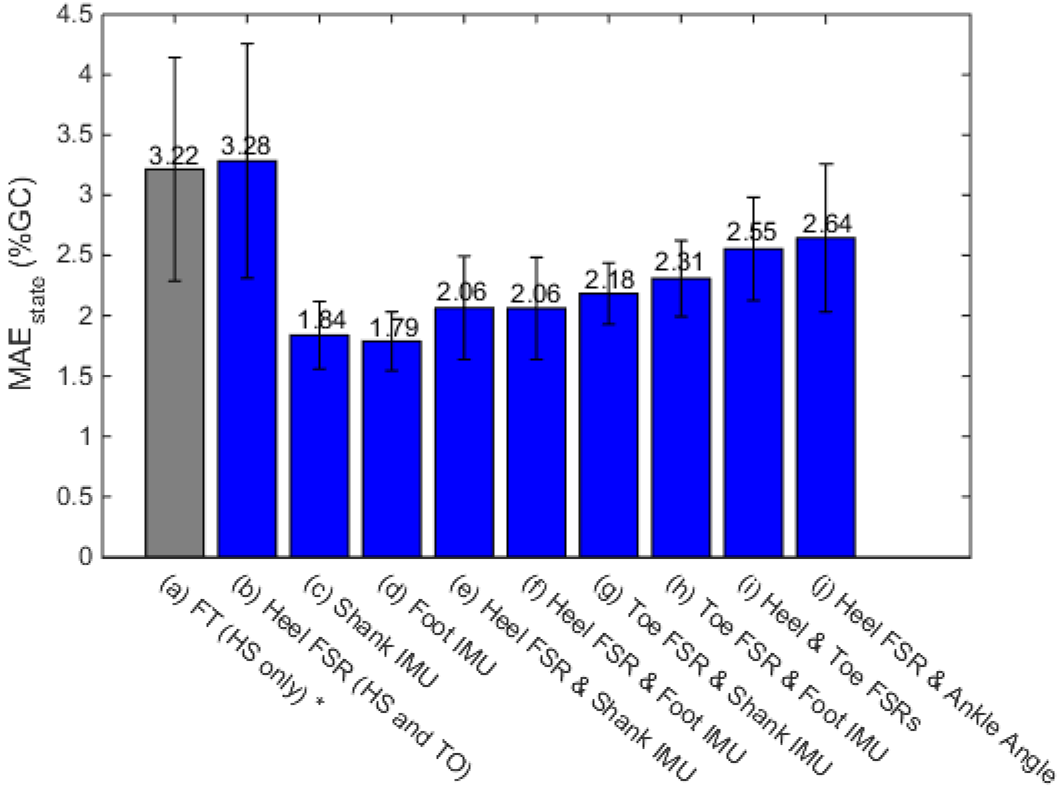

FIGURE 24 MEAN ABSOLUTE ERROR OF GAIT STATE ESTIMATION (%GC) FOR DIFFERENT SENSOR CONFIGURATIONS (HIGHLIGHTED IN BLUE). THE FT STATE ESTIMATER (HIGHLIGHTED IN GRAY) REPRESENTS THE EARLIEST LEVEL OF STATE ESTIMATION PERFORMANCE. *[71]

3.4 Discussion

The main purpose of this study was to investigate the minimum sensor configuration to achieve the simplest cost-effective sensor configuration for robust gait event estimation for a powered ankle-foot orthosis. A total of nine single and dual sensor configurations were compared to identify which configuration(s) resulted in the most accurate performance. Gait data from the sensor were collected from five healthy young subjects while walking on an instrumented treadmill wearing a powered AFO. The results from the sensor data were compared to "true" gait data derived from motion captured kinematic data and ground reaction force data from the treadmill.

In our group, two types of gait event detection approaches have been used for controlling the powered AFO [6, 41, 71]. The first approach, event-based approach, provided torque assistance simply based on the detection of gait events directly from sensor measurements [6]. The second approach, state-based approach, characterized the gait cycle as a set of gait states [41, 71]. Gait state (i.e., % GC) was determined by sensor measurements and used to identify gait events of interests to provide control to the PPAFO. In this study, each selected sensor configuration performance was examined through both event-based and state-based approaches. Selected sensor configuration performances were quantified and compared through event-based and state-based approaches in terms of gait event detection timing and gait state estimation, respectively.

For the gait event detection timing comparison, only heel strike and toe off events were compared since the "true" event timings of these two events were identifiable from GRFs of the treadmill. Out of all sensors, the ankle angle sensor had the highest accuracy error for TO detection. The heel-toe sensors had relatively greater accuracy error for HS and TO detection compared with the two IMU configurations (Table 7). This was because the FSR configurations were heavily reliant on sensor sensitivity and placement. If the heel FSR was not placed at the direct contact point where the physical heel strike happened, it could cause a delay in heel strike detection. On the other hand, IMU configurations did not have this issue since an IMU monitored lower limb kinematics (acceleration, jerk, etc.) directly. The results from the event timing comparison suggested that the sensor configuration that involve IMU had better performances at detecting HS and TO events.

The state estimation comparison suggested that all the sensor configurations that involved an IMU (Figure 24, c-h) appeared to have better performance than the non IMU configurations (Figure 24, a, b, i, j). The single IMU configurations (shank IMU and foot IMU) were able to perform gait state estimation with multiple detected events while maintaining a low error (MAE_{state} < 2% GC) (Figure 24, c&d). The difference between the errors for the two single IMU configurations was minimal (0.05% GC).

From these state estimation comparison results, we concluded that there were two factors that could affect the overall robustness of each sensor configuration: (I) the number of events detected, and (II) the variability of the sensor signals of these events. By comparing the MAE_{state} of the single heel FSR configuration (detecting heel on and heel off events) with the FT state estimator (detecting only heel event) (Figure 24, a&b), we observed that although the single heel FSR configuration could detect two events, the high variability of the heel FSR's signal at the heel off event (Figure 19) slightly increased the MAE_{state} for this configuration (b) compared to (a). However, by adding an additional sensor, e.g., toe FSR or ankle angle sensor, to the heel FSR configuration (Figure 24, i&j), we introduced more events that had less variability, such that the MAE_{state} were reduced for (i) and (j) compared to (b). This reduction was due to the inclusion of more consistent events that not only provided better adjustment to gait variability, but also corrected for the poor performance caused by the events with high variability.

Further comparison between single IMU configurations (shank IMU, foot IMU) were considered. When comparing the number of events detected from each sensor, the shank IMU was capable of detecting more events than the foot IMU (8 vs. 7 events, Table 6). Due to the lack of substantial movement of the foot during the stance phase, the foot IMU was not able to detect events within this phase.

To conclude, single IMU configurations (shank IMU, foot IMU) outperformed other sensor configurations for all comparisons proposed in this study (Figure 24, Table 7). Although the shank IMU had slightly larger errors (MAE) for both event detection timing and gait state estimation when comparing to the foot IMU, the amount of the differences were at minimal. Therefore, since the shank IMU is able to detect more gait events, it is recommended that the single shank IMU is the most cost-effective sensor configuration.

One limitation about the single IMU configuration is that, its performance may be affected if a certain kinematic features during gait are missing (e.g. pathological gait, slipping, tripping etc.). Therefore, an additional failsafe feature might be included. It is worth mentioning that, though a FSR sensor had many limitations such as high event detection timing error and low service life due to repetitive loading, it is still relatively reliable on detecting whether the foot segment is in contact with the ground. This information can be used to provide a failsafe since it increases event detection redundancy. From the event detection timing comparison of this study, we found out that the heel FSR's detection of heel strike event always came in after the IMU's. Therefore we could add in a heel FSR as a failsafe without affecting the IMU's overall performance. Note that this failsafe does not make it equal to configuration (c) because configuration (c) used heel sensor detected as part of its state estimation. The high variability of the heel off event in (c) increased state estimation error.

There were a few limitations in this study. Firstly, this study was performed with healthy subjects walking at their comfortable speed. Gait speed variation may affect the overall performance of the sensor configurations. Further study could be conducted in evaluating different sensor configuration performances on state estimation at different gait speeds. Future study could also focus on investigating the sensor detected events that are not only consistently detectable but also sensitive to variations of gait speed. Secondly, sensor configuration performances can also be evaluated base on their capability of recognizing gait modes (e.g. level ground walking, stair descending and ascending). A pilot study was conducted to investigate the performance of using IMUs to recognize and classify gait modes (Appendix H). The results suggested that the foot IMU was able to classify these three gait modes using 0.1s of inertial sensor data captured after the toe off event (Figure 34).

This pilot study on gait mode classification was done with only one subject. Although the results were promising, more test subjects would help to evaluate the performance of the sensor configurations more accurately.

3.5 Conclusion

For a successful powered AFO application, it is essential to receive information from external sensors to apply control. While many sensors can be used for gait estimation, they also increase the system complexity. The goal of this study was to discover the minimum sensor configuration needed for real-time gait event detection. Multiple sensors as well as their combinations were compared. We conducted the performances evaluation through both event-based approach and state-based approach. As a result, a shank IMU configuration was recommended due to its capability of detecting more events than the foot IMU.

Chapter 4:
CONCLUSIONS AND FUTURE WORK

This thesis was focused on the design of a compact higher torque actuation system and the identification of minimum sensor configuration for a portable powered ankle-foot orthosis (PPAFO). A compact, lightweight, and efficient PPAFO will expand treatment and rehabilitation opportunities for individuals with impairments to the ankle joint complex. Our previous PPAFO design had peak plantarflexor torque of 12 Nm for 100 psig input pressure, which was 17% of peak ankle torque that an 85 kg healthy walker can generate. In addition, the off-the-shelf rotatory actuator had a large and undesirable lateral profile. The bulkiness of the actuator made it difficult to be concealed underneath clothing and increased the risk of interfering with the surrounding environment during gait. To address this issue, we developed a compact high torque system with the goal of enabling future studies on testing the device with various torque settings. With the high torque system being developed, appropriate gait state estimation also becomes essential. If gait can be monitored accurately, the control of a powered AFO can be more effective. There were many studies investigating low-cost, robust wearable sensors for gait event detection. However, with the increasing number of sensors and gait detection methods introduced to gait monitoring systems, the complexity of these systems could also be increased due to the intricate data collection protocols and computationally expensive algorithms. To address this problem, we conducted a study investigating the minimum sensor configuration that would be needed for robust gait event estimation.

4.1. A COMPACT HIGH TORQUE ACTUATION SYSTEM FOR A PORTABLE POWERED ANKLE-FOOT ORTHOSIS (Chapter 2)

4.1.1 Conclusion

Chapter 2 introduced the design and evaluation of a compact and higher torque actuation system for the PPAFO. The actuation system utilized two dual-action linear actuators and a customized gear train to provide plantarflexion and dorsiflexion actuation to the ankle joint. The system, compared with a previous generation design (Gen 2.0), was capable of generating higher torque (166.7% increase) and power (120% increase) output, while delivering a thinner lateral profile (45.1% decrease). The runtime of the Gen 3.0 PPAFO under the same power torque output condition (12 Nm) was longer than the Gen 2.0 design (42.9% and 81.4% increases for test bench emulation and treadmill walking). The runtime at maximum torque and power conditions was shorter than that of Gen 2.0 design (24.4% decrease). This result was expected because the pneumatic cylinders consumed more fuel per step when running at 100 psig. Although the overall weight of the new system had a 21.4% increase compared with Gen 2.0, the Gen 3.0 design could generate substantially more torque which will enable future testing of the system at various torque settings.

4.1.2 Limitations and Future Work

There were a few limitations in this design. Firstly, the weight of the current system was slightly heavier than the Gen 2.0 design (21.4% increase). The weight could be further reduced using lightweight actuators (fiberglass cylinders). Use of fiberglass cylinders could possibly bring the weight of the linear pneumatic system below that of the rotary actuator system. Secondly, a couple of the moving compounds (yoke and actuators' pistons) were still exposed. Because the moving components could possibly injure the wearer, further modification might be needed to fully contain these components. Lastly, as the system was capable of generating high torque, the current binary control strategy becomes problematic. Inaccurate actuation timing of plantarflexion could cause limb discomfort for a low torque system; however, a high torque system could further amplify this error and possibly injure the wearer. Thus, an advanced control strategy is required. Other alternative solutions may include proportional control valves or novel piezoelectric valves. While most commercially available proportional valves are heavy, piezoelectric valves are limited to a low maximum operating pressure and low flow rate. Though the flow rate could be overcome by using multiple piezoelectric valves in parallel, the low operating pressure could still be a problem. Further investigation on identifying proper control strategies is needed.

4.2. MINIMUM SENSOR CONFIGURATION FOR GAIT EVENT DETECTION FOR A PORTABLE POWERED ANKLE-FOOT ORTHOSIS (Chapter 3)

4.2.1 Conclusion

Chapter 3 presented the investigation of a minimum sensor configuration needed for real-time gait event detection. Selected sensor configuration performances were quantified and compared through event-based and state-based approaches in terms of gait event detection timing and gait state estimation, respectively. Gait data were collected from five subjects while walking on a treadmill wearing a powered AFO. Results indicated that, while the single IMU configurations (shank IMU, foot IMU) both outperformed all other configurations (mean state estimation error: < 2% gait cycle; mean event detection timing error: < 23ms), the shank IMU was able to detect more gait events than the foot IMU. Therefore, a shank IMU configuration was recommended for powered AFO applications.

4.2.2 Limitations and Future Work

There were a few limitations in this study. Firstly, this study was performed with healthy subjects walking at their comfortable speed. Gait speed variation may affect the overall performance of the sensor configurations. Further study could be conducted in evaluating different sensor configuration performances on state estimation at different gait speeds. Future study could also focus on investigating the sensor detected events that are not only consistently detectable but also sensitive to variations of gait speed. Secondly, sensor configuration performances can also be evaluated based on their capability of recognizing gait modes (e.g. level ground walking, stair descending and ascending). A pilot study was conducted to investigate the performance of using IMUs to recognize and classify gait modes. The results suggested that the foot IMU was able to classify these three gait modes using 0.1s of inertial sensor data captured after the toe off event. This pilot study on gait mode classification was done with only one subject. Although the results were promising, more test subjects would help to evaluate the performance of the sensor configurations more accurately.

Appendix A: Gear Surface Area Calculations [*]

It was assumed that the total surface area of the gear set was proportional to its total weight due to the uniform gear thickness (0.25 inch) and material density (steel: 4.5oz/inch^3). Therefore, total surface area with respect to each input gear (IG) and sector gear (SG) combination was calculated. Surface area (SA) estimations were performed by approximating each gear as an annulus with an outer diameter (OD) equal to the pitch diameter (PD). The inner diameter (ID) of the annulus corresponded to gear shaft diameter. ID on the SG was 0.5" and ID on the IG and output gear (OG) were 0.25". Area of addendums and negative area of dedendums were ignored (and assumed to roughly negate one another). Surface area of the OG was estimated based on the following relationship representing area of the pitch circle minus area of the shaft:

$$SA_{\mathrm{OG}} = \left[\pi \cdot \left(\frac{PD_{OG}}{2}\right)^2 - \pi \cdot (.125")^2\right] \qquad (8)$$

Approximation of SA_{SG} was more complex due to the trimming of additional material from a full circular gear. The area of a wedge had to be calculated and then the area corresponding to the gear hub had to be added:

$$SA_{\mathrm{SG}} = \left[\pi \cdot \left(\frac{PD_{SG}}{2}\right)^2 - \pi \cdot (.25")^2\right] \cdot \frac{55}{360} \quad + \quad [\pi \cdot (.5")^2 - \pi \cdot (.25")^2] \cdot \frac{360-55}{360} \; (9)$$

The expression of SA_{SG} represents a 55° wedge of an annulus of ID = .5" and OD = PD_{OG}. The second portion of SA_{SG} represents the addition o[1]f hub material to the sector gear. This hub is represented by an annulus with an ID of .5" and an OD of 1". This annulus only takes up the fraction of the circle complimentary to the 55° already occupied by the wedge shaped component or $\frac{360-55}{360}$ (Figure 25).

---

[*] This work is adapted from Aaron Benjamin, the 2015 summer REU student.

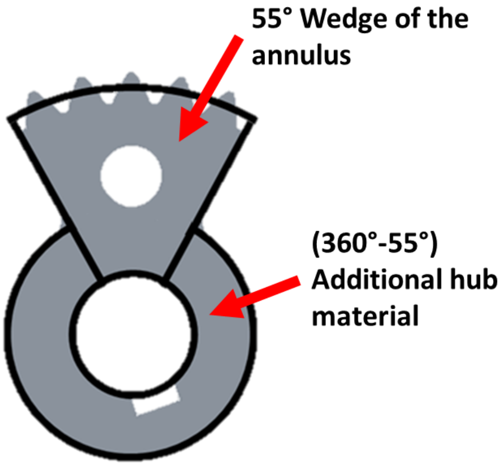

FIGURE 25 ANNULUS REPRESENTATION OF GEAR SURFACE AREA ESTIMATION

The surface area of the trimmed IG can be approximated by the same method as SA_{SG} using different circular fractions, IDs, and ODs (ID = .25”, OD = PD_{IG})

$$SA_{\text{IG}} = \left[\pi\left(\frac{PD_{IG}}{2}\right)^2 - \pi(.125")^2\right]\frac{12}{PD_{IG}\cdot DP} + [\pi(.25")^2 - \pi(.125")^2]\,\frac{PD_{IG}\cdot DP-12}{PD_{IG}\cdot DP} \qquad (10)$$

This calculation becomes slightly more complex because the angle required to trim this gear (to retain 12 and only 12 teeth) varies with PD. Thus, the fraction of gear retained becomes $\frac{12}{PD_{IG}\cdot DP}$ (where $PD_{IG}\cdot DP$ = the number of IG teeth). The fraction of hub added to the wedge then becomes the compliment to the circle of the fraction of wedge retained or $\frac{PD_{IG}\cdot DP-12}{PD_{IG}\cdot DP}$.

Appendix B: Gear box FEA analysis

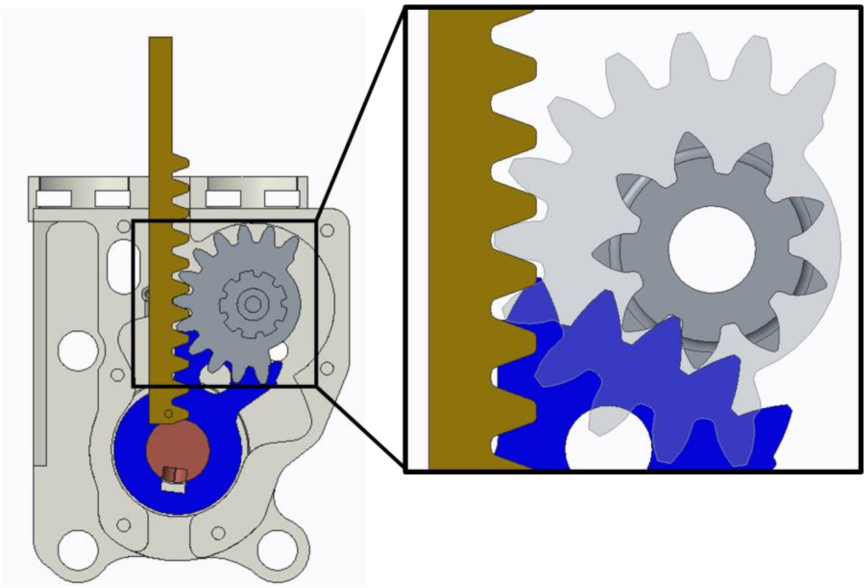

Figure 26 Model of gear box and compound gear train (compound input gear was set transparent for better visualization)

Though the true 3D printed material properties were unknown, an FEA analysis was conducted to estimate the potential stresses that our gearbox design might experience during operation. The maximum input force (i.e., push force (Pf)) in this analysis was set equal to the force generated by the linear actuators when both linear actuators' extend chambers were pressurized to 100 psi. The resulting maximum push force applied to the gear rack from linear actuators was about 180 lbf (pressure times extend chamber EPA). For the gear system, the force between mating teeth can be resolved at the contacting point into two components [86]; tangential force Ft and radial force Fr. The equation used to calculate the Fr from known tangential load is:

$$Fr = Ft \tan(\phi) \qquad (11)[86]$$

where:

ϕ = pressure angle (35˚)

The tangential force between the linear rack and the compound input gear Ft_1 was 180 lbf as mentioned previously and the tangential force between compound output gear and sector gear Ft_2 was 360 lbf (twice of 180 lbf due to compound gear ratio of 2:1) (Figure 27). We then applied the tangential forces to equation (11) to find the radial loads (i.e., $Fr_1 = Ft_1 \tan(\phi)$ & $Fr_2 = Ft_2 \tan(\phi)$). The resulting radial loads $Fr_1$and Fr_2 were 126 lbf and 252 lbf, respectively.

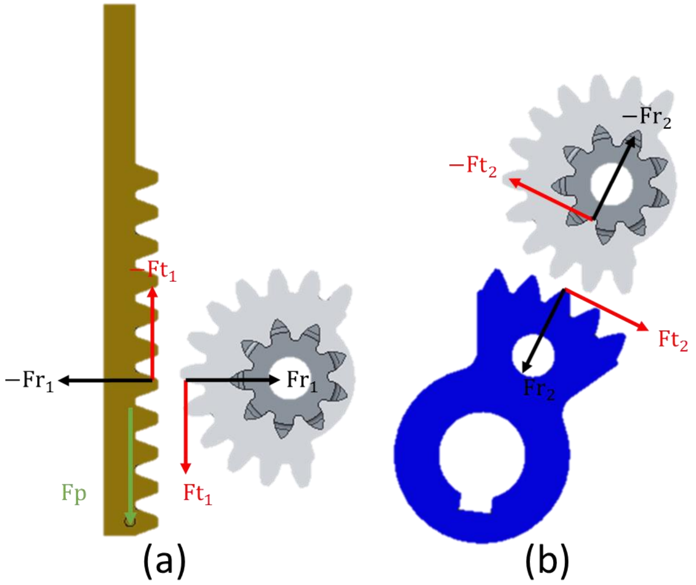

FIGURE 27 TANGENTIAL AND RADIAL FORCES BETWEEN (A) LINEAR RACK AND COMPOUND INPUT GEAR, (B) COMPOUND OUTPUT GEAR AND SECTOR GEAR.

The sum of the forces for each gear was calculated then applied to the gear box model in Creo (Figure 28). In addition to the forces that were generated between gears, an additional pull force was also considered (Figure 28). The pull force (180lbf) was the result from the aluminum inserts holding linear actuators in position (i.e., countering the 180 lbf push force).

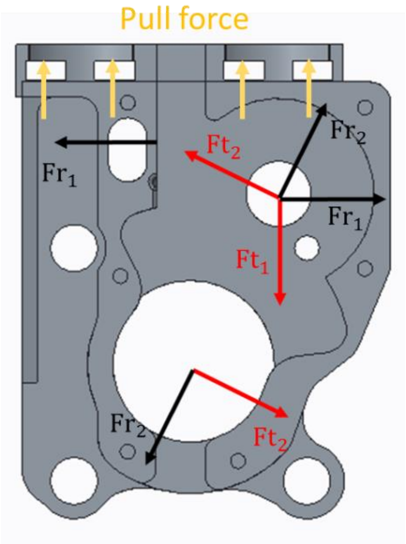

FIGURE 28 FORCES BEING APPLIED TO THE GEAR BOX.

Appendix C: Off-the-shelf components used for Gen 3.0 PPAFO

Component	**Part number**	**Manufacture**	**Location**	**Quantity**
Dual action linear actuator	091.092-D	Bimba	University Park, IL	2
Fast switching solenoid valve	MHE2-MS1H- 3/2O-QS-4	Festo Corp US	Hauppauge, NY	2
Pressure regulator	LRMA-QS-4	Festo Corp US	Hauppauge, NY	1
Pressure sensor	TBPDANN150PGUCV	Honeywell	Morristown, NJ	2
Instrumentation amplifier for pressure sensor	AD623 AN	Analog Devices	Norwood, MA	2
Ankle angle sensor	MP1-L-0050-103-5%-RH	Spectrasymbol	Salt Lake City, UT	1
Microcontroller	STM32F407VG	STMicroelectronics	Geneva, Switzerland	1
CO2 bottle with embedded pressure regulator	JacPac J-6901- 91	Pipleline Inc.	Waterloo, ON, Canada	1
Force sensitive resistor	SEN-09376 ROHS	SparkFun Electronics	Niwot, CO	2
Inertial measurement unit	MPU9250	InvenSense	San Jose, CA	2

Appendix D: Electric Pressure Sensor Circuit & Housing

The electric pressure sensor utilized an instrumentation amplifier (AD623 AN) and a Honeywell TBP pressure sensor (TBPDANN150PGUCV). With a 5 V power supply in a pressure range of 0 – 150 psig on the sensor, according to the pressure sensor's datasheet, voltage output was expected to be less than or equal to 47.52 mV. The instrumentation amplifier was used to amplify this signal within the range of detection on the STM32F4 Discovery Development Board in use. This board detects an analog signal from 0.0 V– 3.0 V. Thus, the dynamic range of the amplifier had to be less than 3 V. According to the amplifier's datasheet, the equation for calculating required Gain (G) for the TBP signal was:

$$\mathrm{G} = \frac{3.0\ \mathrm{V}}{0.04752\ \mathrm{V}} = 63.1 \qquad (12)$$

Gain resistance (RG) was then calculated as:

$$\mathrm{R_G} = \frac{100{,}000}{\mathrm{G}-1} = 1609\ \Omega \qquad (13)$$

Through experimentation, $\mathrm{R_G}$ was fine tuned to 1650 Ω to provide a satisfactory range in output voltage (<3.0 V).

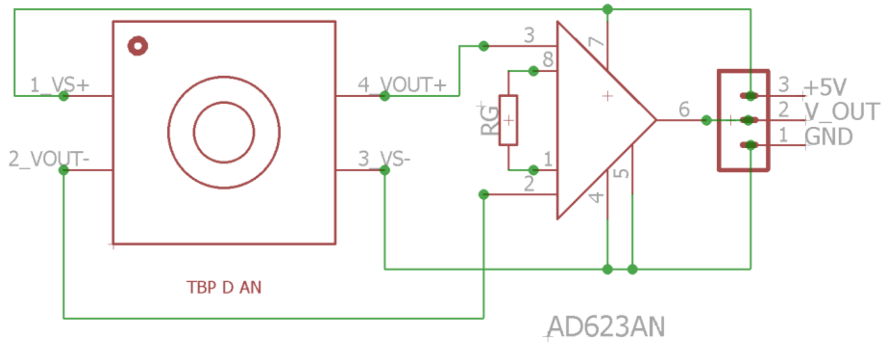

FIGURE 29 CIRCUIT DIAGRAM

Upon completing the circuit (Figure 29 & Figure 30), a case was constructed for the circuit boards for use as an inline sensor. A Legris push to connect (P2C) connector for a 4 mm tube outer diameter (OD) was adapted for use with the board (Figure 30) to simplify the tube connection.

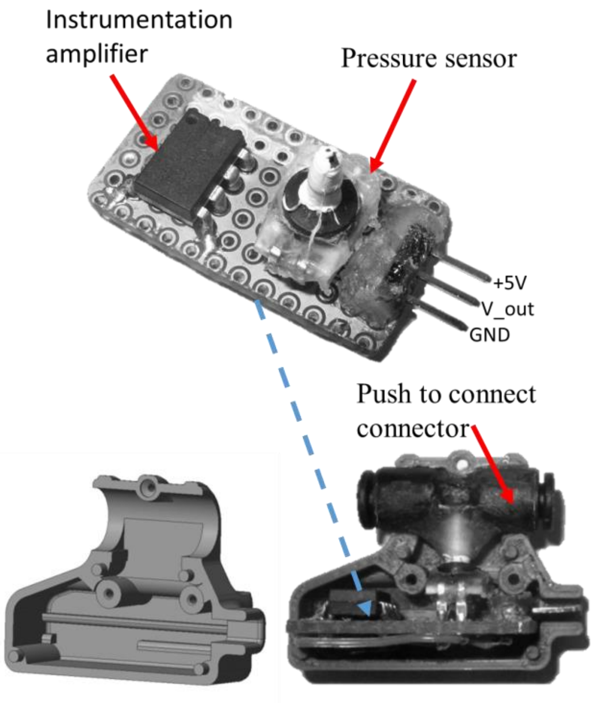

Figure 30 (a) Pressure sensor board, (b) 3d circuit housing model, and (c) housing with circuit board and push to connect connector

Appendix E: Ankle angle sensor (linear magnetic potentiometer) conversion

The linear magnetic potentiometer (MagnetoPot; Spectra Symbol; West Valley City, UT) was attached to the linear pneumatic actuators. Due to the actuators' linear motion being directly translated to ankle joint through the gear train, the potentiometer measurement could be converted to ankle angle measurement. The potentiometer outputs an analog signal (V, in Volt) resulting from the piston position change (L, in m). Therefore, through the calibration, the analog signal could be mapped to the piston linear motion then converted to ankle angle measurement (θ_{ankle} in °). The equation used for converting the analog reading to angle is as follows:

$$L = \frac{V-0.277}{2.94-0.277} \cdot 0.0475 \qquad (14)$$

where 0.277 and 2.94 (in Volt) are the minimum and maximum analog reading from the potentiometer (corresponding to the maximum dorsiflexion angle and maximum plantarflexion angle). 0.0475 (in m) is the full range of motion of the potentiometer. The linear motion was then converted to the ankle angle θ_{ankle} through the known compound gear ratio (GR) and sector gear pitch diameter (PD_{SG}):

$$\theta_{ankle} = \frac{L}{GR \cdot \frac{PD_{SG}}{2}} \cdot \frac{180}{\pi} - 35 \qquad (15)$$

where

$GR = 2$, is the compound gear ratio

$PD_{SG} = 0.0508\, m$ (2 inch), is the pitch diameter of the sector gear

35 (in °) is the maximum plantar flexion angle

The validation of the angle measurement was performed by comparing the calculated joint angles with the joint angles manually measured with a goniometer (Figure 31). The discrepancies were assessed by the Pearson correlation coefficient in MATLAB program using the function "corrcoef" (the Mathworks Inc., Natick, MA, USA). The two sets of measurements had a correlation coefficient of 0.9943.

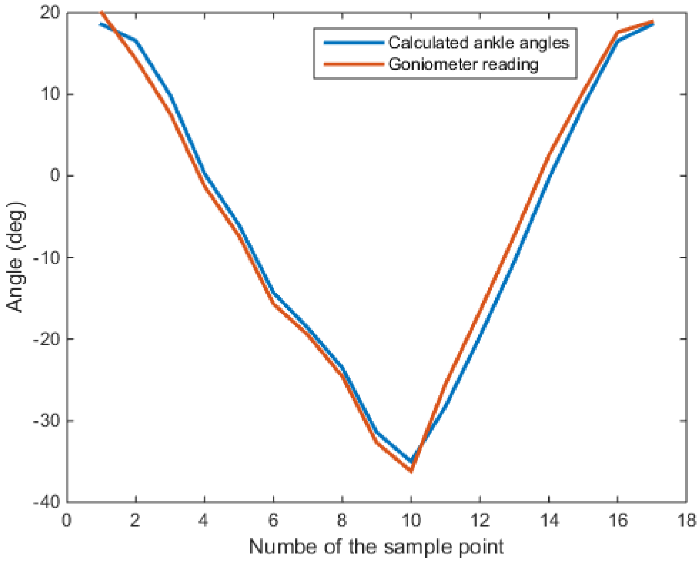

FIGURE 31 COMPARISON OF CALCULATED ANKLE ANGLE AND GONIOMETER ANGLE READING

Appendix F: Supplemental study on IMU placement using Vicon system

A supplemental study was conducted to find the best IMU placement because there were two options of where to place the IMU sensors when measuring segment orientation (either on the carbon fiber shells of the orthosis (shank and foot shell) or strapped directly to the shank and foot segments).

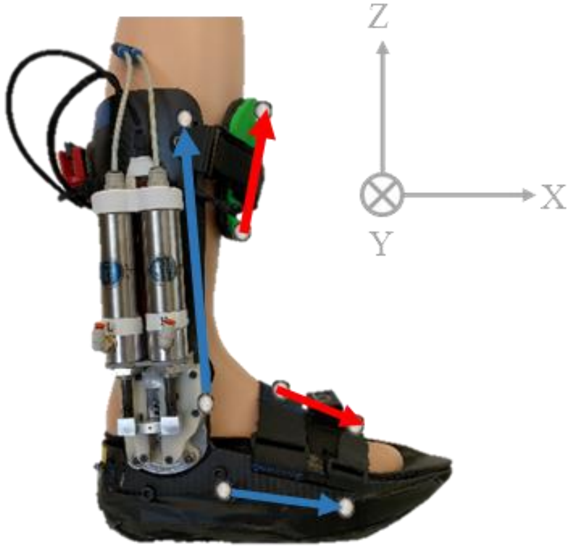

FIGURE 32 VECTOR REPRESENTATION AND VICON GLOBAL COORDINATE SYSTEM

We used a motion capture system (Model 460; Vicon, Oxford, UK) to capture the shell-based ankle angle and body segment-based ankle joint angle. A total of eight markers were placed on the carbon fiber shells and the straps on the body segments with four vectors representing the orientation of the attached surfaces in sagittal plane (x-z plane) (Figure 18.a). The vector angles $\theta_v$were then derived as follows:

$$\theta_v = \tan^{-1}\left(\frac{\vec{v}_z}{\vec{v}_x}\right) \qquad (16)$$

Where $\vec{v}_x$ and $\vec{v}_z$ are the x and z component of each vector.

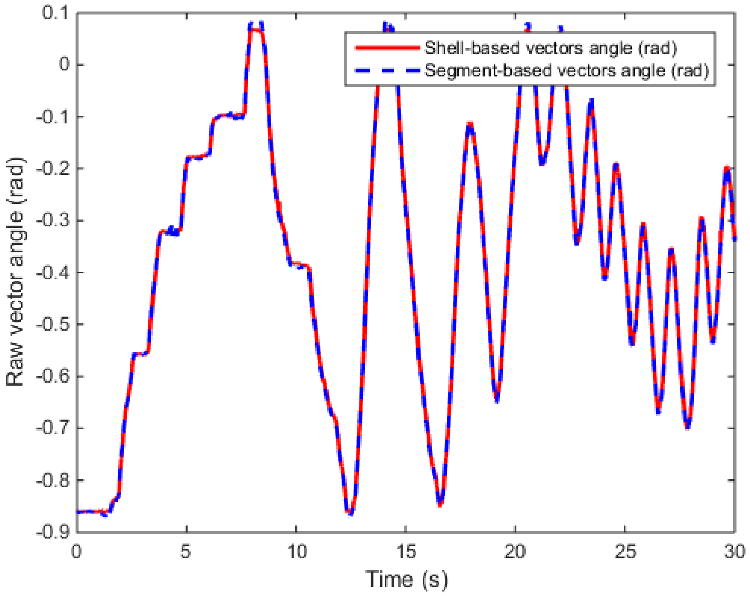

FIGURE 33 RAW VECTOR ANGLE MEASUREMENT FROM SHELL-BASED VECTORS (RED) AND SEGMENT-BASED VECTORS (DASHED BLACK)

Raw (nonfiltered) shell-based vectors angle and body segment-based vectors angle were derived (Figure 33). The discrepancies of the two measurements were accessed by Pearson correlation coefficient in MATLAB program (the Mathworks Inc., Natick, MA, USA). This supplemental study found that the two ankle angles had a correlation coefficient of 0.9998. This result effectively meant that with the PPAFO securely attached to the shank-foot segments, the movement artifact between the body and PPAFO was minimal.

Appendix G: Kalman filter for computing shank angular position

Because the segment orientation could also be used to indicate certain gait events (i.e., shank segment angle was 90˚ to the ground at ***Mid of MSt***), we implemented a Kalman filter to estimate the shank IMU orientation, then converted it to the shank orientation [53, 64, 109]. The IMU orientation was first calculated through the gyroscope (θ_{gyr}) by integrating the gyroscope reading ω_{shank}. The integration error (drift over time) was then corrected through the Kalman filter using the angle calculated from accelerometer readings a_x and a_z using trigonometry ($e.g.,\ \theta_{acc} = \tan^{-1}\left(-\frac{a_x}{a_z}\right)$).

We first denote the state matrix *x* at time k as:

$$x_k = \begin{bmatrix} \theta_{gyr} \\ \omega_b \end{bmatrix}_k \qquad (17)\ [53, 64, 109]$$

with θ_{gyr} being the gyroscope angle calculated by integrating ω_{shank} and $\omega_b$being bias based upon the measurements from the gyroscope. The bias $\omega_b$was the amount that the gyro has drifted and was initially set as 0 then consistently being updated. The calculation of $\omega_b$will be covered in the later steps. The estimated current state $\hat{x}_k$ based on all the previous states $\hat{x}_{k-1}$ and the current gyro measurement ω_{gyr} was derived as follow:

$$\hat{x}_k = F\hat{x}_{k-1} + B\omega_{gyr} \qquad (18)$$

where ω_{gyr} was also called a control input, in this case it was the gyroscope measurement in degrees per second (°/s). F was the state transition model which was applied to the previous state $\hat{x}_{k-1}$ and B was the control input model ($F = \begin{bmatrix} 1 & \Delta t \\ 0 & 1 \end{bmatrix}$ and $B = \begin{bmatrix} \Delta t \\ 0 \end{bmatrix}$ with Δt representing sampling time; i.e., 0.002s) [64].

An updated estimation error covariance matrix P_k was defined based on the previous error covariance matrix P_{k-1}. This matrix was used to estimate how much we should trust the current values of the estimated state. The smaller the value of P_k, then the more that we trust the current estimated state.

$$P_k = FP_{k-1}F^T + Q_k \Delta t \qquad (19)$$

where P was a 2×2 covariance matrix that was constantly being updated. P was initially set as $\begin{bmatrix} 0 & 0 \\ 0 & 0 \end{bmatrix}$. Q_k is the current process noise covariance matrix and in this case the covariance matrix of the state estimate of the angle and bias. It was defined as $\begin{bmatrix} Q_{\theta_{gyr}} & 0 \\ 0 & Q_{\omega_b} \end{bmatrix}$ [53]. $Q_{\theta_{gyr}}$and Q_{ω_b} are the variances of calculated gyroscope angle and gyroscope measurement bias. Common values used for $Q_{\theta_{gyr}}$ and Q_{ω_b} for our IMU (MPU9250; InvenSense; San Jose, CA) were $Q_{\theta_{gyr}} = 0.001$ and $Q_{\omega_b} = 0.003$ [111].

The angle difference between the accelerometer angle measurement θ_{acc} and the estimated state was defined as

$$\tilde{y}_k = \theta_{acc} - H\hat{x}_k \qquad (20)$$

Where H was the observation model ($H = [1 \quad 0]$) used to map the estimated state $\hat{x}_k$ to the observed space (i.e., from a 2 × 1 matrix to a scalar value).

Next, we calculated the innovation covariance which was used to predict how much we should trust the measurement based on the error covariance matrix P_k

$$S_k = HP_kH^T + R \qquad (21)$$

where R is the covariance of the measurement noise. It is noted that a bigger measurement noise will result in a larger S which means the incoming measurement is less reliable which will result in a smaller Kalman gain. In our case, due to the accelerometer's large noise caused by heel strike, the incoming measurement θ_{acc} was less reliable. Therefore, the value for R was manually tuned to 50 [66]. Kalman gain was then derived as:

$$K_k = P_k H^T S_k^{-1} \qquad (22)$$

and the Kalman filtered estimated current state was calculated as:

$$\hat{x}_k = \hat{x}_{k-1} + K_k \tilde{y}_k \qquad (23)$$

Note that since $\hat{x}_k$ was defined as a 2 × 1 matrix which consisted of θ_{gyr} and ω_b. The gyroscope angle and bias were updated here.

Finally, we updated the error covariance matrix.

$$P_k = (I - K_k H) P_k \qquad (24)$$

where I was an identity matrix.

Appendix H: Pilot study on gait mode classification

To better evaluate the performance of the two single IMU configurations (shank IMU, foot IMU), we conducted a pilot study to identify which IMU placement had distinct features for better potential of recognizing and classifying three gait modes (level ground walking, stair ascending and descending). As a pilot study, we had one male subject (age 27 years, height 178 cm, weight 85 kg) wearing the unpowered PPAFO and walking on level ground and indoor stairs – two stair traverse (h = 18m per stair). The subject was asked to walk in one gait mode at a time with his own comfortable speed. Four trials of data per gait mode were collected (total 12 trials). For each trial and gait mode the subject was told to complete 6 full steps (total 6×12 steps). The first trial of each condition was used as training data, and the remaining three trials were used for testing. The sensor sampling rate was set at 500 Hz.

Three of the IMU signals (x & z-direction acceleration (a_x & a_z) and y-direction angular velocity ($\boldsymbol{\omega}_{gyr}$)) were used to identify a feature matrix. Event detection methods described in section 2.2.3 were used to identify the toe off event during the three types of gait. Immediately after identifying the toe off event, 50 data points (equivalent to 0.1 second under the 500 Hz sampling rate) of each signal were recorded. Training matrix $C_{i,n}$was constructed by combining all of the training steps from trial one, with i representing number of training steps and n representing total data points ($3_{sensors} \times 50_{data\ points}$) per trial.

Next, using principle component analysis (PCA) [112], we identified the most distinct feature within the training matrix $C_{i,n}$ by reducing its dimension to one (1D). We first found the covariance matrix $Cov(C)$, then found the linear map or the weight matrix W for reducing the dimension.

$$W = [(\boldsymbol{\Lambda})^{-\frac{1}{2}} \times V^T]_{d \times n} \qquad (25)$$

where, $\boldsymbol{\Lambda}$ was a diagonal matrix of generalized eigenvalues and $V$was a full matrix whose columns were the corresponding eigenvectors computed from $Cov(C)$. W was a $d \times n$ matrix with d representing the reduced number of features ($d = 1$ in this case).

Upon identifying the weight matrix W through the training data (the first trial of each gait mode), the rest of the trials could be classified into three states (level ground walking, stair ascending and descending) by multiplying W with each testing step.

$$Z = W \times C_{i,n} \qquad (26)$$

with i representing number of testing steps and n representing total data points ($3_{sensors} \times 50_{data\,points}$) per trial. Z was the resulting principal component scores which can be used to identify the three states. A gaussian distribution of Z was assumed for the PCA results (Figure 34). The classification results from the shank IMU's data indicated a similarity between stair descending and level ground walking as the Gaussian distributions had a significant amount of overlapping (Figure 34).

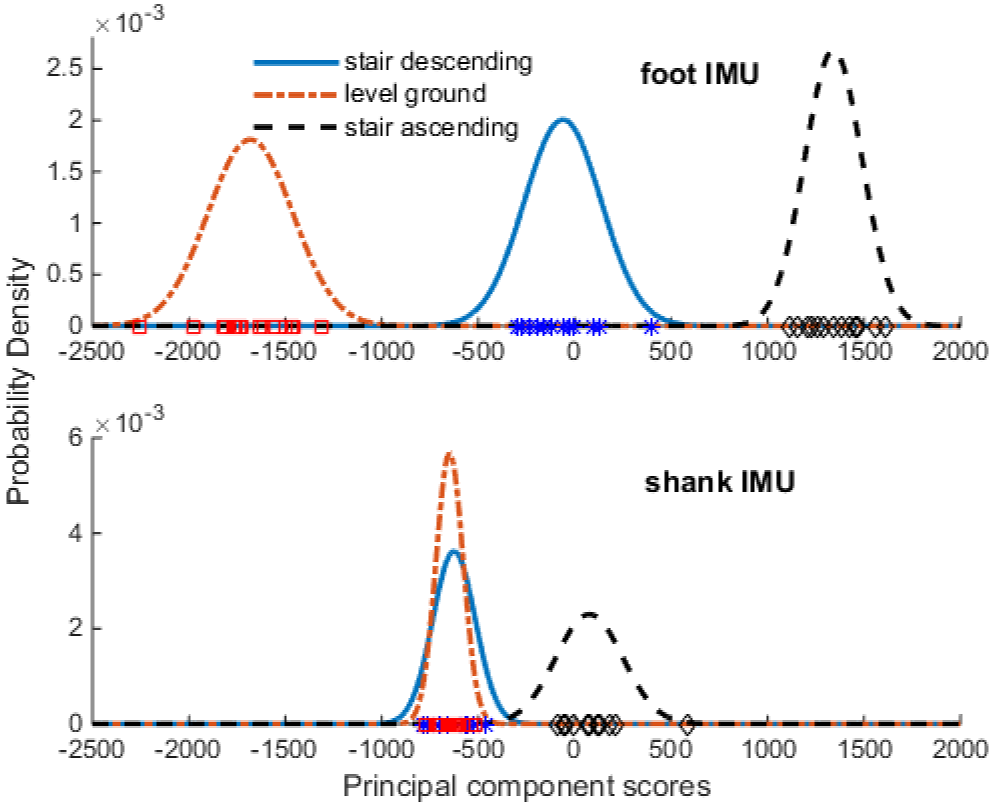

FIGURE 34 GAUSSIAN DISTRIBUTION OF GAIT MODE CLASSIFICATION RESULT USING SINGLE IMU CONFIGURATIONS

For the gait mode detection, the PCA result suggested that the foot IMU configuration had the capability of distinctively classifying each of the three gait modes with a reduced 1D feature. This result suggested that the initial data from the shank segment during level ground walking and stair descending had less distinct features. Further study is recommended for developing a more robust algorithm to identify gait modes.

REFERENCES

[1] E. Ayyappa, "Normal Human Locomotion, Part 1: Basic Concepts and Terminology," *Journal of Prosthetics and Orthotics,* vol. 9, no. 1, pp. 10-17, Jan 1 1997.

[2] J. Perry, J. M. Burnfield, and L. M. Cabico, *Gait analysis: normal and pathological function*, 1 ed.: Slack Thorofare, NJ, 1992.

[3] L. Maryasin. (2013, Mar 29). *Dummy human male*. Available: https://grabcad.com/library/dummy-human-male. Date accessed: 2016, Feb 1

[4] V. T. Inman and H. D. Eberhart, "The major determinants in normal and pathological gait," *Journal of Bone and Joint Surgery,* vol. 35, no. 3, pp. 543-558, Jul 1 1953.

[5] Centers for Disease Control and Prevention (CDC), "Prevalence of Disability and Disability Type Among Adults — United States, 2013," *Morbidity and Mortality Weekly Reports,* vol. 64, no. 29, pp. 777-783, July 31 2015.

[6] K. A. Shorter, G. F. Kogler, E. Loth, W. K. Durfee, and E. T. Hsiao-Wecksler, "A portable powered ankle-foot orthosis for rehabilitation," *Journal of Rehabilitation Research and Development,* vol. 48, no. 4, pp. 459-472, Nov 4 2011.

[7] B. Ovbiagele, L. B. Goldstein, R. T. Higashida, V. J. Howard, S. C. Johnston, O. A. Khavjou*, et al.*, "Forecasting the future of stroke in the United States: a policy statement from the American Heart Association and American Stroke Association," *Stroke,* vol. 44, no. 8, pp. 2361-2375, Aug 1 2013.

[8] P. Mathew J Reeves, M. Cheryl D Bushnell, D. P. George Howard, M. Julia Warner gargano, P. Pamela W Duncan, M. Gwen Lynch*, et al.*, "Sex differences in stroke: epidemiology, clinical presentation, medical care, and outcomes," *The Lancet Neurology,* vol. 7, no. 10, pp. 915-926, Oct 31 2009.

[9] Centers for Disease Control and Prevention (CDC), "Outpatient Rehabilitation Among Stroke Survivors --- 21 States and the District of Columbia, 2005," *Morbidity and Mortality Weekly Reports,* vol. 56, no. 20, pp. 504-507, April 02 2007.

[10] B. Chen, H. Ma, L. Qin, F. Gao, K. Chan, S. Law*, et al.*, "Recent developments and challenges of lower extremity exoskeletons," *Journal of Orthopaedic Translation,* vol. 5, pp. 26-37, Apr 30 2016.

[11] V. L. Nickel, D. L. Savill, A. Karchak, Jr., and J. R. Allen, "Synthetically Powered Orthotic Systems," *Journal of Bone and Joint Surgery,* vol. 47, pp. 458-464, Aug 1 1965.

[12] T. F. Yan, M. Cempini, C. M. Oddo, and N. Vitiello, "Review of assistive strategies in powered lower-limb orthoses and exoskeletons," *Robotics and Autonomous Systems,* vol. 64, pp. 120-136, Feb 28 2015.

[13] A. B. Zoss, H. Kazerooni, and A. Chu, "Biomechanical design of the Berkeley lower extremity exoskeleton (BLEEX)," *IEEE/ASME Transactions on Mechatronics,* vol. 11, no. 2, pp. 128-138, Apr 2006.

[14] D. Sanz-Merodio, M. Cestari, J. C. Arevalo, and E. Garcia, "A lower-limb exoskeleton for gait assistance in quadriplegia," in *2012 IEEE International Conference on Robotics and Biomimetics (ROBIO)*, Guangzhou, China, Dec 11-14, 2012, pp. 122-127.

[15] Y. Sankai, "HAL: Hybrid Assistive Limb Based on Cybernics," in *Robotics Research*. vol. 66, 1 ed: Springer, 2010, pp. 25-34.

[16] L. Ren, D. Howard, L. Q. Ren, C. Nester, and L. M. Tian, "A Phase-Dependent Hypothesis for Locomotor Functions of Human Foot Complex," *Journal of Bionic Engineering,* vol. 5, no. 3, pp. 175-180, Sep 30 2008.

[17] Y. Li, "On Improving Control and Efficiency of a Portable Pneumatically Powered Ankle-Foot Orthosis," PhD Dissertation, Mechanical Science and Engineering University of Illinois at Urbana-Champaign, 2013.

[18] M. K. Boes, M. Islam, Y. David Li, and E. T. Hsiao-Wecksler, "Fuel efficiency of a Portable Powered Ankle-Foot Orthosis," in *2013 IEEE International Conference on Rehabilitation Robotics (ICORR)*, Seattle, WA, Jun 24-26, 2013, pp. 1-6.

[19] D. A. Winter, *Biomechanics and Motor Control of Human Movement*, 4 ed.: John Wiley & Sons, NJ, 2009.

[20] A. Zoss and H. Kazerooni, "Design of an electrically actuated lower extremity exoskeleton," *Advanced Robotics,* vol. 20, no. 9, pp. 967-988, Jan 1 2006.

[21] A. T. Asbeck, K. Schmidt, I. Galiana, D. Wagner, and C. J. Walsh, "Multi-joint Soft Exosuit for Gait Assistance," in *2015 IEEE International Conference on Robotics and Automation (ICRA)*, Seattle, WA, May 26-30, 2015, pp. 6197-6204.

[22] L. M. Mooney, E. J. Rouse, and H. M. Herr, "Autonomous exoskeleton reduces metabolic cost of human walking," *Journal of Neuroengineering and Rehabilitation,* vol. 11, no. 1, p. 1, May 9 2014.

[23] L. M. Mooney and H. M. Herr, "Biomechanical walking mechanisms underlying the metabolic reduction caused by an autonomous exoskeleton," *Journal of Neuroengineering and Rehabilitation,* vol. 13, no. 1, p. 4, Jan 28 2016.

[24] I. W. Hunter, J. M. Hollerbach, and J. Ballantyne, "A comparative analysis of actuator technologies for robotics," in *Robotics Review 2*. vol. 2, 1 ed: MIT Press, 1992, pp. 299-342.

[25] A. Young and D. Ferris, "State-of-the-art and Future Directions for Robotic Lower Limb Exoskeletons," *IEEE Transactions on Neural Systems and Rehabilitation Engineering,* vol. PP, no. 99, p. 1, Jan 27 2016.

[26] J. C. Xia and W. K. Durfee, "Analysis of Small-Scale Hydraulic Actuation Systems," *Journal of Mechanical Design,* vol. 135, no. 9, p. 91001, Sep 1 2013.

[27] B. C. Neubauer, J. Nath, and W. K. Durfee, "Design of a portable hydraulic ankle-foot orthosis," in *2014 Annual International Conference of the IEEE Engineering in Medicine and Biology Society (EMBC)*, Chicago, IL, Aug 26-30, 2014, pp. 1182-1185.

[28] A. Zoss and H. Kazerooni, "Architecture and hydraulics of a lower extremity exoskeleton," in *2005 ASME International Mechanical Engineering Congress and Exposition (IMECE)*, Orlando, FL, Nov 5-11, 2005, pp. 1447-1455.

[29] D. P. Ferris and C. L. Lewis, "Robotic lower limb exoskeletons using proportional myoelectric control," in *2009 Annual International Conference of the IEEE Engineering in Medicine and Biology Society (EMBC)*, Minneapolis, MN, Sep 3-6, 2009, pp. 2119-2124.

[30] G. S. Sawicki and D. P. Ferris, "Mechanics and energetics of level walking with powered ankle exoskeletons," *Journal of Experimental Biology,* vol. 211, no. 9, pp. 1402-1413, May 1 2008.

[31] D. P. Ferris, K. E. Gordon, G. S. Sawicki, and A. Peethambaran, "An improved powered ankle-foot orthosis using proportional myoelectric control," *Gait and Posture,* vol. 23, no. 4, pp. 425-428, Jun 30 2006.

[32] M. Wehner, B. Quinlivan, P. M. Aubin, E. Martinez-Villalpando, M. Baumann, L. Stirling*, et al.*, "A Lightweight Soft Exosuit for Gait Assistance," in *2013 IEEE International Conference on Robotics and Automation (ICRA)*, Karlsruhe, Germany, May 6-10, 2013, pp. 3362-3369.

[33] R. Chin, E. T. Hsiao-Wecksler, E. Loth, G. Kogler, S. D. Manwaring, S. N. Tyson*, et al.*, "A pneumatic power harvesting ankle-foot orthosis to prevent foot-drop," *Journal of Neuroengineering and Rehabilitation,* vol. 6, no. 1, p. 19, Jun 19 2009.

[34] S. H. Collins, M. B. Wiggin, and G. S. Sawicki, "Reducing the energy cost of human walking using an unpowered exoskeleton," *Nature,* vol. 522, no. 7555, pp. 212-215, Jun 11 2015.

[35] V. Agostini, G. Balestra, and M. Knaflitz, "Segmentation and classification of gait cycles," *IEEE Transactions on Neural Systems and Rehabilitation Engineering,* vol. 22, no. 5, pp. 946-952, Sep 2014.

[36] M. M. Skelly and H. J. Chizeck, "Real-time gait event detection for paraplegic FES walking," *IEEE Transactions on Neural Systems and Rehabilitation Engineering,* vol. 9, no. 1, pp. 59-68, Mar 2001.

[37] J. Bae and M. Tomizuka, "Gait phase analysis based on a Hidden Markov Model," *Mechatronics,* vol. 21, no. 6, pp. 961-970, Sep 30 2011.

[38] S. K. Ng and H. J. Chizeck, "Fuzzy model identification for classification of gait events in paraplegics," *IEEE Transactions on Fuzzy Systems,* vol. 5, no. 4, pp. 536-544, Nov 1997.

[39] G. Dominguez, E. Cardiel, S. Arias, and P. Rogeli, "A Digital Goniometer based on encoders for measuring knee-joint position in an orthosis," in *2013 World Congress on Nature and Biologically Inspired Computing (NaBIC)*, Fargo, ND, Aug 12-14, 2013, pp. 1-4.

[40] K. A. Witte, J. J. Zhang, R. W. Jackson, and S. H. Collins, "Design of Two Lightweight, High-Bandwidth Torque-Controlled Ankle Exoskeletons," in *2015 IEEE International Conference on Robotics and Automation (ICRA)*, Seattle, WA, May 26-30, 2015, pp. 1223-1228.

[41] M. Islam and E. T. Hsiao-Wecksler, "Gait State Estimation for Powered Ankle Orthosis using Modified Fractional Timing and Artificial Neural Network," *Journal of Medical Devices,* vol. 10, no. 2, p. 200920, May 12 2016.

[42] A. Muro-de-la-Herran, B. Garcia-Zapirain, and A. Mendez-Zorrilla, "Gait analysis methods: an overview of wearable and non-wearable systems, highlighting clinical applications," *Sensors,* vol. 14, no. 2, pp. 3362-3394, Feb 19 2014.

[43] M. O. Derawi, C. Nickel, P. Bours, and C. Busch, "Unobtrusive User-Authentication on Mobile Phones Using Biometric Gait Recognition," in *2010 International Conference on Intelligent*

Information Hiding and Multimedia Signal Processing (IIH-MSP), Darmstadt, Germany, Oct 15-17, 2010, pp. 306-311.

[44] R. W. Selles, M. A. Formanoy, J. B. Bussmann, P. J. Janssens, and H. J. Stam, "Automated estimation of initial and terminal contact timing using accelerometers; development and validation in transtibial amputees and controls," *IEEE Transactions on Neural Systems and Rehabilitation Engineering,* vol. 13, no. 1, pp. 81-88, Mar 2005.

[45] T. Kikuchi, S. Tanida, K. Otsuki, T. Yasuda, and J. Furusho, "Development of third-generation intelligently controllable ankle-foot orthosis with compact MR fluid brake," in *2010 IEEE International Conference on Robotics and Automation (ICRA)*, Anchorage, AK, May 3-7, 2010, pp. 2209-2214.

[46] H. Sun and T. Yuao, "Curve aligning approach for gait authentication based on a wearable accelerometer," *Physiological Measurement,* vol. 33, no. 6, pp. 1111-1120, May 24 2012.

[47] J. Taborri, E. Palermo, S. Rossi, and P. Cappa, "Gait Partitioning Methods: A Systematic Review," *Sensors,* vol. 16, no. 1, p. 66, Jan 6 2016.

[48] R. E. Mayagoitia, A. V. Nene, and P. H. Veltink, "Accelerometer and rate gyroscope measurement of kinematics: an inexpensive alternative to optical motion analysis systems," *Journal of Biomechanics,* vol. 35, no. 4, pp. 537-542, Apr 30 2002.

[49] D. Gouwanda and A. A. Gopalai, "A robust real-time gait event detection using wireless gyroscope and its application on normal and altered gaits," *Medical Engineering and Physics,* vol. 37, no. 2, pp. 219-225, Feb 28 2015.

[50] K. Aminian, B. Najafi, C. Bula, P. F. Leyvraz, and P. Robert, "Spatio-temporal parameters of gait measured by an ambulatory system using miniature gyroscopes," *Journal of Biomechanics,* vol. 35, no. 5, pp. 689-699, May 31 2002.

[51] Y. L. Park, B. R. Chen, N. O. Perez-Arancibia, D. Young, L. Stirling, R. J. Wood*, et al.*, "Design and control of a bio-inspired soft wearable robotic device for ankle-foot rehabilitation," *Bioinspiration and Biomimetics,* vol. 9, no. 1, p. 016007, Jan 16 2014.

[52] D. K. Shaeffer, "MEMS Inertial Sensors: A Tutorial Overview," *IEEE Communications Magazine,* vol. 51, no. 4, pp. 100-109, Apr 2013.

[53] I. Cikajlo, Z. Matjacic, and T. Bajd, "Efficient FES triggering applying Kalman filter during sensory supported treadmill walking," *Journal of Medical Engineering and Technology,* vol. 32, no. 2, pp. 133-144, Jan 1 2008.

[54] A. M. Sabatini, C. Martelloni, S. Scapellato, and F. Cavallo, "Assessment of walking features from foot inertial sensing," *IEEE Transactions on Biomedical Engineering,* vol. 52, no. 3, pp. 486-494, Mar 2005.

[55] S. O. Madgwick, A. J. Harrison, and A. Vaidyanathan, "Estimation of IMU and MARG orientation using a gradient descent algorithm," in *2011 IEEE International Conference on Rehabilitation Robotics (ICORR)*, Zürich, Switzerland, Jun 29-Jul 01, 2011, pp. 1-7.

[56] A. Peruzzi, U. Della Croce, and A. Cereatti, "Estimation of stride length in level walking using an inertial measurement unit attached to the foot: a validation of the zero velocity assumption during stance," *Journal of Biomechanics,* vol. 44, no. 10, pp. 1991-1994, Jul 7 2011.

[57] C. Caltran and A. A. G. Siqueira, "Sensor fusion applied to position estimation and gait identification of an ankle-foot orthosis," in *2011 ISSNIP Biosignals and Biorobotics Conference (BRC)*, Vitoria, Brazil, Jan 6-8, 2011, pp. 1-6.

[58] S. L. Nogueira, A. A. Siqueira, R. S. Inoue, and M. H. Terra, "Markov jump linear systems-based position estimation for lower limb exoskeletons," *Sensors,* vol. 14, no. 1, pp. 1835-1849, Jan 22 2014.

[59] Y. D. Li and E. T. Hsiao-Wecksler, "Gait mode recognition and control for a portable-powered ankle-foot orthosis," in *2013 IEEE International Conference on Rehabilitation robotics (ICORR)*, Seattle, WA, Jun 24-26, 2013, pp. 1-8.

[60] J. J. Kavanagh and H. B. Menz, "Accelerometry: a technique for quantifying movement patterns during walking," *Gait and Posture,* vol. 28, no. 1, pp. 1-15, Jul 31 2008.

[61] V. Ahanathapillai, J. D. Amor, Z. Goodwin, and C. J. James, "Preliminary study on activity monitoring using an android smart-watch," *Healthcare Technology Letters,* vol. 2, no. 1, pp. 34-39, Feb 25 2015.

[62] S. Mazilu, U. Blanke, and G. Troster, "Gait, wrist, and sensors: Detecting freezing of gait in Parkinson's disease from wrist movement," in *2015 IEEE International Conference on Pervasive Computing and Communication Workshops (PerCom Workshops)*, St. Louis, MO, Mar 23-27, 2015, pp. 579-584.

[63] H. Dejnabadi, B. M. Jolles, and K. Aminian, "A new approach to accurate measurement of uniaxial joint angles based on a combination of accelerometers and gyroscopes," *IEEE Transactions on Biomedical Engineering,* vol. 52, no. 8, pp. 1478-1484, Aug 2005.

[64] Y. Teruyama and T. Watanabe, "A basic study on variable-gain Kalman filter based on angle error calculated from acceleration signals for lower limb angle measurement with inertial sensors," in *2013 Annual International Conference of the IEEE Engineering in Medicine and Biology Society (EMBC)*, Osaka, Japan, Jul 3-7, 2013, pp. 3423-3426.

[65] F. Alonge, E. Cucco, F. D'Ippolito, and A. Pulizzotto, "The use of accelerometers and gyroscopes to estimate hip and knee angles on gait analysis," *Sensors,* vol. 14, no. 5, pp. 8430-8446, May 13 2014.

[66] A. M. Sabatini, "Estimating three-dimensional orientation of human body parts by inertial/magnetic sensing," *Sensors,* vol. 11, no. 2, pp. 1489-1525, Jan 26 2011.

[67] J. Rueterbories, E. G. Spaich, B. Larsen, and O. K. Andersen, "Methods for gait event detection and analysis in ambulatory systems," *Medical Engineering and Physics,* vol. 32, no. 6, pp. 545-552, Jul 31 2010.

[68] M. D. Djuric-Jovicic, N. S. Jovicic, and D. B. Popovic, "Kinematics of gait: new method for angle estimation based on accelerometers," *Sensors,* vol. 11, no. 11, pp. 10571-10585, Nov 7 2011.

[69] W. Tao, T. Liu, R. Zheng, and H. Feng, "Gait analysis using wearable sensors," *Sensors,* vol. 12, no. 2, pp. 2255-2283, Feb 16 2012.

[70] C. R. Kinnaird and D. P. Ferris, "Medial gastrocnemius myoelectric control of a robotic ankle exoskeleton," *IEEE Transactions on Neural Systems and Rehabilitation Engineering,* vol. 17, no. 1, pp. 31-37, Feb 2009.

[71] D. Y. Li, A. Becker, K. A. Shorter, T. Bretl, and E. T. Hsiao-Wecksler, "Estimating System State During Human Walking With a Powered Ankle-Foot Orthosis," *IEEE/ASME Transactions on Mechatronics,* vol. 16, no. 5, pp. 835-844, Oct 2011.

[72] H. A. Varol, F. Sup, and M. Goldfarb, "Real-time Gait Mode Intent Recognition of a Powered Knee and Ankle Prosthesis for Standing and Walking," in *2008 IEEE RAS & EMBS International Conference on Biomedical Robotics and Biomechatronics (BioRob)*, Scottsdale, AZ, Oct 19-22, 2008, pp. 66-72.

[73] J. U. Chu, K. I. Song, S. Han, S. H. Lee, J. Y. Kang, D. Hwang*, et al.*, "Gait phase detection from sciatic nerve recordings in functional electrical stimulation systems for foot drop correction," *Physiological Measurement,* vol. 34, no. 5, pp. 541-565, Apr 22 2013.

[74] D. Ewins, "Gait event detection during stair walking using a rate gyroscope," *Sensors,* vol. 14, no. 3, pp. 5470-5485, Mar 19 2014.

[75] K. A. Shorter, J. C. Xia, E. T. Hsiao-Wecksler, W. K. Durfee, and G. F. Kogler, "Technologies for Powered Ankle-Foot Orthotic Systems: Possibilities and Challenges," *IEEE/ASME Transactions on Mechatronics,* vol. 18, no. 1, pp. 337-347, Feb 2013.

[76] W. Svensson and U. Holmberg, "Ankle-Foot-Orthosis Control in Inclinations and Stairs," in *2008 IEEE Conference on Robotics, Automation and Mechatronics (CIS-RAM)*, Chengdu, China, Sep 21-24, 2008, pp. 301-306.

[77] K. A. Shorter, "The Design and Control of Active Ankle-Foot Orthoses," PhD Dissertation, Mechanical Science and Engineering, University of Illinois at Urbana-Champaign 2011.

[78] M. K. Boes, "Evaluation of a pneumatic ankle-foot orthosis: portability and functionality," PhD Dissertation, Mechanical Science and Engineering, University of Illinois at Urbana-Champaign 2016.

[79] M. K. Boes, R. E. Klaren, R. M. Kesler, M. Islam, Y. Learmonth, M. N. Petrucci*, et al.*, "Spatiotemporal and Metabolic Impacts on Gait of a Powered Ankle Exoskeleton in Persons with Multiple Sclerosis," in *39th Annual Meeting of the American Society of Biomechanics*, Columbus, OH, Aug 5-8, 2015.

[80] M. N. Petrucci, C. D. MacKinnon, and E. T. Hsiao-Wecksler, "Modulation of anticipatory postural adjustments of gait using a portable powered ankle-foot orthosis," in *2013 IEEE International Conference on Rehabilitation Robotics (ICORR)*, Seattle, WA, June 24-26, 2013, pp. 1-6.

[81] E. T. Hsiao-Wecksler, K. A. Shorter, Y. D. Li, G. F. Kogler, and W. K. Durfee, "Portable Pneumatically-Powered Ankle-Foot Orthosis," *Journal of Medical Devices,* vol. 6, no. 1, p. 017593, Mar 1 2012.

[82] K. A. Shorter, Y. Li, E. A. Morris, G. F. Kogler, and E. T. Hsiao-Wecksler, "Experimental evaluation of a portable powered ankle-foot orthosis," in *2011 Annual International Conference of the IEEE*

Engineering in Medicine and Biology Society (EMBC), Boston, MA, Aug 30- Sep 03, 2011, pp. 624-627.

[83] M. Gerrity, C. Vogel, V. Caliendo, and J. Lewis, "Design of Compact and Efficient Pneumatic Actuator for Ankle-Foot Orthosis," Final Report,May 9 2012.

[84] J. P. Dougherty, R. J. Dreste, A. M. Grabo, and N. Rupprecht, "Design of a Compact and Efficient Pneumatic Actuator for an Ankle Orthotic," Final Report,May 2013.

[85] A. Barry, A. Davis, R. Epping, and S. Kelly, "Design of a Compact, Efficient, and Robust Ankle Orthotic," Final Report,May 9 2014.

[86] R. C. Juvinall and K. M. Marshek, *Fundamentals of machine component design*, 5 ed.: John Wiley & Sons, NJ, 2006.

[87] R. F. Handschuh and A. J. Zakrajsek, "High-pressure angle gears: Comparison to typical gear designs," *Journal of Mechanical Design,* vol. 133, no. 11, p. 114501, Nov 1 2011.

[88] S. P. Radzevich, *Dudley's handbook of practical gear design and manufacture*, 2 ed.: CRC Press, Taylor & Franciis Group, NW, 2012.

[89] R. Hessmer. (2014). *Involute Spur Gear Builder (C) 2014 Dr. Rainer Hessmer*. Available: http://hessmer.org/gears/InvoluteSpurGearBuilder.html. Date accessed: 2016, Feb 1

[90] B. Izquierdo, S. Plaza, J. A. Sánchez, I. Pombo, and N. Ortega, "Numerical prediction of heat affected layer in the EDM of aeronautical alloys," *Applied Surface Science,* vol. 259, pp. 780-790, Oct 15 2012.

[91] DSM Somos. *Somos® ProtoGen™ O-XT 18420* Available: https://www-s.mechse.uiuc.edu/rplab/media/sla_materials_dsm_somos_protogen_o-xt_18420.pdf. Date accessed: 2016, Feb 1

[92] Bimba Manufacturing Company. (2016). *Original Line® Air Cylinder*. Available: http://www.bimba.com/Products-and-Cad/Actuators/Inch/Round-Line/Non-Repairable/Original-Line-Cylinder/. Date accessed: 2015, Mar 1

[93] Parker Hannifin. (2016). *Miniature HI-ROTOR/Standard type PRNseries*. Available: http://www.wainbee.com/suppliers/Parker/rotaryActuators/0900PRN.pdf. Date accessed: 2016, Jun 4

[94] M. Islam and E. T. Hsiao-Wecksler, "Developing a Classification Algorithm for Plantarflexor Actuation Timing of a Powered Ankle-Foot Orthosis," in *Design of Medical Devices Conference (DMD)*, Minneapolis, MN, April 11-14, 2016.

[95] E. H. Yang, C. Lee, and J. M. Khodadadi, "Development of MEMS-based piezoelectric microvalve technologies," *Sensors and Materials,* vol. 19, no. 1, pp. 1-18, Jan 1 2007.

[96] H. Wirtl and U. Sixt. (2014). *White paper Piezo technology in pneumatic valves*. Available: https://www.festo.com/net/SupportPortal/Files/346243/White_Paper_Piezo_EN.pdf. Date accessed: 2016, Feb 1

[97] K. E. Gordon and D. P. Ferris, "Learning to walk with a robotic ankle exoskeleton," *Journal of Biomechanics,* vol. 40, no. 12, pp. 2636-2644, Dec 31 2007.

[98] B. R. Greene, D. McGrath, R. O'Neill, K. J. O'Donovan, A. Burns, and B. Caulfield, "An adaptive gyroscope-based algorithm for temporal gait analysis," *Medical and Biological Engineering and Computing,* vol. 48, no. 12, pp. 1251-1260, Dec 1 2010.

[99] A. Salarian, H. Russmann, F. J. G. Vingerhoets, C. Dehollain, Y. Blanc, P. R. Burkhard*, et al.*, "Gait assessment in Parkinson's disease: toward an ambulatory system for long-term monitoring," *IEEE Transactions on Biomedical Engineering,* vol. 51, no. 8, pp. 1434-1443, Aug 2004.

[100] S. K. Au, P. Bonato, and H. Herr, "An EMG-position controlled system for an active ankle-foot prosthesis: an initial experimental study," in *2005 IEEE International Conference on Rehabilitation Robotics (ICORR)*, Chicago, IL, Jun 28-Jul 1, 2005, pp. 375-379.

[101] C. Fleischer, C. Reinicke, and G. Hommel, "Predicting the intended motion with EMG signals for an exoskeleton orthosis controller," in *2005 IEEE/RSJ International Conference on Intelligent Robots and Systems (IROS)*, Edmonron, AB, Canada, Aug 2-6 2005, pp. 2029-2034.

[102] S. Yang and Q. Li, "Inertial sensor-based methods in walking speed estimation: A systematic review," *Sensors,* vol. 12, no. 5, pp. 6102-6116, May 10 2012.

[103] Z. Wang and E. T. Hsiao-Wecksler, "Design of a Compact High Torque Actuation System for Portable Powered Ankle-Foot Orthosis," in *Design of Medical Devices Conference (DMD)*, Minneapolis, MN, April 11-14, 2016.

[104] J. Carberry, G. Hinchly, J. Buckerfield, E. Tayler, T. Burton, S. Madgwick*, et al.*, "Parametric design of an active ankle foot orthosis with passive compliance," in *2011 IEEE International Symposium on Computer-Based Medical Systems (CBMS),* , Bristol, UK, Jun 27-30, 2011, pp. 1-6.

[105] M. Hanlon and R. Anderson, "Real-time gait event detection using wearable sensors," *Gait and Posture,* vol. 30, no. 4, pp. 523-527, Nov 30 2009.

[106] Q. Li, M. Young, V. Naing, and J. M. Donelan, "Walking speed and slope estimation using shank-mounted inertial measurement units," in *2009 IEEE International Conference on Rehabilitation Robotics (ICORR)*, Kyoto, Japan, Jun 23-26, 2009, pp. 839-844.

[107] P. Catalfamo, S. Ghoussayni, and D. Ewins, "Gait Event Detection on Level Ground and Incline Walking Using a Rate Gyroscope," *Sensors,* vol. 10, no. 6, p. 5683, Jun 4 2010.

[108] V. Chawda, O. Celik, and M. K. O. Malley, "Application of Levant's differentiator for velocity estimation and increased Z-width in haptic interfaces," in *2011 IEEE World Haptics Conference (WHC)*, Istanbul, Turkey, Jun 21-24, 2011, pp. 403-408.

[109] T. Watanabe, H. Saito, E. Koike, and K. Nitta, "A preliminary test of measurement of joint angles and stride length with wireless inertial sensors for wearable gait evaluation system," *Computational Intelligence and Neuroscience,* vol. 2011, p. 6, Jan 1 2011.

[110] M. R. Patterson, E. Delahunt, K. T. Sweeney, and B. Caulfield, "An ambulatory method of identifying anterior cruciate ligament reconstructed gait patterns," *Sensors,* vol. 14, no. 1, pp. 887-899, Jan 7 2014.

[111] K. S. Lauszus. (2012). *A practical approach to Kalman filter and how to implement it*. Available: http://blog.tkjelectronics.dk/2012/09/a-practical-approach-to-kalman-filter-and-how-to-implement-it/. Date accessed: 2015, Feb 1

[112] M. Islam, "Studies on Gait Control Using a Portable Pneumatically Powered Ankle-Foot Orthosis (PPAFO) During Human Walking," PhD Dissertation, Mechanical Science and Engineering, University of Illinois at Urbana-Champaign 2016.